Black hole dynamics in Effective Field Theory extensions to General Relativity

by

Ramiro Cayuso

A thesis
presented to the University of Waterloo
in fulfillment of the
thesis requirement for the degree of
Doctor of Philosophy
in
Physics

Waterloo, Ontario, Canada, 2023

Examining Committee Membership

The following served on the Examining Committee for this thesis. The decision of the Examining Committee is by majority vote.

External Examiner:	Helvi Witek Assistant Professor, Department of Physics, University of Illinois Urbana-Champaign (UIUC)
Supervisor(s):	Luis Lehner Adjunct Faculty, Dept. of Physics and Astronomy, University of Waterloo Perimeter Institute for Theoretical Physics
Internal Member:	William E. East Adjunct Faculty, Dept. of Physics and Astronomy, University of Waterloo Perimeter Institute for Theoretical Physics
Internal Member:	Matthew Johnson Adjunct Faculty, Dept. of Physics and Astronomy, University of Waterloo Perimeter Institute for Theoretical Physics
Internal-External Member:	Eduardo Martin-Martinez Associate Professor, Dept. of Applied Mathematics, University of Waterloo Perimeter Institute for Theoretical Physics
Other Member(s):	Niayesh Afshordi Professor, Dept. of Physics and Astronomy, University of Waterloo Perimeter Institute for Theoretical Physics

Author's Declaration

This thesis consists of material all of which I authored or co-authored: see Statement of Contributions included in the thesis. This is a true copy of the thesis, including any required final revisions, as accepted by my examiners.

I understand that my thesis may be made electronically available to the public.

Statement of Contributions

The research presented in this thesis is based on coauthored publications to which I made significant contributions and a single-authored publication.

Chapter 4 covers research from [59] conducted in collaboration with Luis Lehner. Chapter 5 covers research from [58] conducted in collaboration with Pau Figueras, Tiago França, and Luis Lehner. Chapter 6 covers research from a single-author publication [57].

Abstract

This thesis aims to develop and implement mathematical and numerical techniques to enable the study of deviations from General Relativity (GR) in the nonlinear regime. The focus is on studying the nonlinear dynamics of higher derivative Effective Field Theory (EFT) extensions to GR and employing innovative methods to address the associated mathematical and practical challenges. To this end, we utilize two crucial techniques: the *Fixing the Equations* method, which controls spurious high frequencies, and the *Order reduction* approach to address challenges related to higher than second order time derivatives and ghosts.

The research starts with a detailed study of black hole dynamics in a higher derivative extension of General Relativity described by a dimension-eight operator EFT. A fully nonlinear/non-perturbative treatment is presented for constructing initial data and studying its dynamical behavior in spherical symmetry when coupled to a massless scalar field.

Subsequently, we extend the previous work to explore the evolution of black holes merging in quasi-circular orbits within the same higher-derivative EFT extension. This scenario poses more demanding challenges; a toy model and the single-boosted black hole scenario are considered to build up to the binary merger case. The effects of modifications on the dynamics and gravitational wave emission in the binary merger scenario are studied.

The research work culminates with a study of gravitational collapse in Quadratic Gravity, the leading order correction to GR from an EFT perspective in the presence of matter fields. An *Order Reduction* approach is used to eliminate additional degrees of freedom associated with higher order time derivatives. We study the collapse of a massless scalar field into a black hole in spherical symmetry. We explore the stability of our simulations, whether the solutions remain within the bounds of EFT, and their deviations from General Relativity during the collapse.

Acknowledgements

I would like to thank all the people who made this thesis possible.

I would first like to thank my advisor, Luis Lehner. I would like to thank you for all these years of guidance, in addition to physics, I've learned a lot from you. Thanks for always challenging me to look further than what is immediately in front of me. I learned that this is how special things are found. Thank you for telling me all of those things that start with, " I shouldn't be saying this ". And mostly, thanks for being such a nice person and the best supervisor I could have hoped to have.

I would like to thank the Strong Gravity group. I am so thank full to have been part of it all of these years, it has always been such a pleasure to meet with all of you. Our meetings always had an incredibly friendly environment, very stimulating discussions, and hilarious moments.

I want to thank the several collaborators I had the pleasure of working with, Pau Figueras, Tiago França, Miguel Bezares, and Guillermo Lara. Doing research with you has been a wonderful experience and always a lot of fun.

I thank my committee members, William East, Matthew Johnson, and Niayesh Afshordi, for their guidance during my PhD. I would also like to thank them, as well as the examiners of this thesis, Helvi Witek and Eduardo Martin-Martinez, for reading this thesis and your work to examine it.

I would also like to thank all of the staff at PI, the bistro staff, IT, and the admin staff. Without you, PI would turn into ashes very quickly, you make PI a wonderful place to work at.

I also thank Maite Dupuis for doing an amazing job as Academic and Research Programs Director and for caring so much for the well-being of students at PI. I would also like to thank the PSI fellows, my journey at PI started in the PSI program, and they really make it a unique experience.

I would like to thank all of the people responsible for maintaining Symmetry (special mention to Erik Schnetter) and the Digital Research Alliance of Canada. The numerical simulations in this thesis were performed on Symmetry at PI , and on the Niagara cluster at the University of Toronto.

I would like to thank all the friends I made in Perimeter and in Waterloo. Life would have been very different without your company and friendship all these years. Aiden, Max, Nils, Taillte, Guillaume, Soham, Jake, Finn, Mike, Celine, Luciano, Ana, Anna, Amalia, Francisco, Bruno, and Hanna. Every one of you, in your own way, made my life better, and you all have a place in my heart. I hope that our paths cross again very soon.

I would like to thank my whole family for their love and support over these very long years away from you. To Mama and Papa, everything I am and will be is thanks to you, you are the most loving parents a son could have. To my siblings, Lauri, Reni, and Juani, thank you for putting up with your baby brother, for being amazing, and for teaching him so much about life. To my grandmothers Martha who would always light up a room with her characteristic laughter, and Marta, who would always light up a candle when I had an exam, Abu, wherever you are, do you think you can pull one of those again for my defense? I can not begin to explain how grateful I am for having you all.

Finally, I would like to thank Sara for all of the fun, companionship, and support you gave me through all of these years. This PhD has been a hard endeavor, and having you in my life helped me get and grow through it. I am so happy to have met you here in Waterloo and that our lives together will continue somewhere new.

Table of Contents

List of Figures

List of Tables

Chapter 1

Introduction

The theory of General Relativity (GR), formulated over a hundred years ago, stands as one of the most remarkable achievements in the history of physics. It certainly revolutionized our understanding of gravity and its profound influence on the dynamics of our Universe. To date, backed by an extensive body of experimental evidence [182], GR has consistently showcased its unparalleled precision in describing the intricate dynamics of gravitational phenomena. Its predictive power has shown remarkably accurate descriptions at vastly different scales, from solar system dynamics, the dynamics of compact objects such as Black Holes and neutron stars inspiraling and merging, to the large cosmic structures of galaxies in the expanding Universe. One of the most renowned pieces of evidence (and most relevant for the subject of this thesis) is the detection of gravitational waves (GW) predicted by the theory. Binary pulsar timing experiments [181], were first able to indirectly confirm that GWs were being emitted, and more recently GWs, thanks to colossal efforts from experimentalists and theorists, direct detection of the GWs emitted from compact binary mergers is now possible using ground-based gravitational wave interferometers from the LIGO/Virgo/KAGRA (LVK) collaboration [5, 2]. Recently, NANOGrav [10], by analyzing 15-year millisecond pulsar-timing data, provided evidence for the existence of a GW background in the nanohertz regime. The window that GWs opened enables the observation of the Universe through a different lens, giving us the chance to peer into the nature of gravity in the highly dynamical and strong regime.

Despite its impressive empirical success, GR confronts profound theoretical obstacles that indicate it may not serve as the ultimate theory of gravity. GR's non-renormalizability [175, 101] raises compatibility issues with Quantum Mechanics and Quantum Field Theory, compelling the quest for a quantum theory of gravity that has remained a formidable challenge in theoretical physics for decades. Moreover, the existence of singularities within black holes, as predicted by GR, implies its inadequacy to provide accurate predictions at the largest curvature scales, thereby foreshadowing its own limitations. On a different front, one regarding large scales, experiments indicate that with our current understanding of gravity, dark matter and dark energy need to be introduced in our models to account for all the matter-energy content and the rate of expansion of our Universe. The standard model of cosmology, backed by its observational success [11], is the ΛCDM model. However, the fundamental origins of some of its constituent pieces are still unknown. The value of the cosmological constant, which accounts for the rate of expansion of our Universe, presents a perplexing problem in cosmology (known as the cosmological constant problem), as it is extremely small compared to theoretical predictions [180, 140]. Unraveling the origin of dark matter presents a significant challenge, the exceedingly weak interactions of dark matter particles with ordinary matter make their detection and identification extremely hard [137]. These reasons have fueled the exploration and proposal of numerous alternative theories of gravity.

Scenarios falling within the strong-field and highly dynamical regime may have the potential to exhibit slight departures from GR. In this regime, gravitational fields are comparable to the system's mass-energy content, rapid evolution occurs relative to the system's characteristic size, and the objects' velocities approach the speed of light. In this regime, the detection of GWs originating from the mergers of compact binary systems represents the most compelling probe to explore the extreme manifestations of gravity and possible deviations from GR. During its first three observing runs (currently on its fourth), the LVK collaboration has successfully detected a significant number of events. These events have been attributed to the merger of various astrophysical systems, including pairs of black holes, pairs of neutron stars, and the merger between a black hole and a neutron star. To date, analysis [6] of these events have not revealed any significant deviations from GR. This outcome suggests that if there are any deviations present in this regime, they must be small in nature. The quality and quantity of collected data are bound to improve with the future advancement in sensitivity of our current detectors and the deployment of new detectors such as the Laser Interferometer Space Antenna (LISA) [21, 167] and of 3rd generation ground base interferometers like Einstein's Telescope [139].

However, the level of scrutiny to which we will be able to test GR is not solely determined by the precision and reach of our detectors. It also hinges on the quality of our predictions, both within the framework of GR and potential extensions. The detection and characterization of GW events rely heavily on the accuracy of waveform templates that are matched against the observed data. So far, most GW tests of GR have been conducted as self-consistency tests. This approach involves analyzing the data assuming that GR describes GW events utilizing waveform templates derived from GR to search for inconsistencies that may indicate deviations from the theory, see, for example, [99]. However, this task presents considerable challenges. As the precision of GW detectors increases, they become sensitive to a greater number of effects predicted by GR. Consequently, distinguishing potential deviations from GR amidst the increasing complexity of GR itself becomes an increasingly demanding task. In most cases, when deviations from GR are considered in the models, this is done through parameterized deviations, for example, by considering deviations [9] to the Post-Newtonian (PN) [35] parameters. The drawback to this approach is that the way these parameters are modified lacks a direct link to physically motivated extensions to GR. This can make the constraints from such an approach weaker and harder to translate into alternative theories, even rendering them physically non-informative.

An alternative to this approach is directly matching against waveforms generated from specific modified theories. This task comes with both practical (and technical) challenges. Most proposed beyond GR theories have, at a formal level, mathematical pathologies, making their understanding in general scenarios difficult. Such pathologies may include loss of uniqueness, a dynamical change of character in the equations of motion (e.g., from hyperbolic to elliptic), or, even worse, having equations of motion (EOMs) of unknown mathematical type [153, 161, 74, 86]. Combined with the need to use computational simulations to study the (nonlinear/dynamical) regime of interest, this becomes a challenging scenario. There are now several instances [58, 66, 19, 32, 24, 83, 87, 116] where full nonlinear numerical simulations of compact binary coalescence have been achieved in modified gravity candidate theories. Obtaining waveforms by solving the complete nonlinear problem is not only crucial for accurately predicting the physics in the highly nonlinear regime, but also highly valuable for assessing the strengths, weaknesses, and accuracy of the analytical techniques used to model the inspiral and ringdown phases of the waveforms. Since such techniques are rooted in perturbation theory, results from the nonlinear theory can help us identify when a given approximation is insufficient and higher-order terms in the expansions may be required.

Aside from these technical difficulties, there is the issue of which particular theory direct our efforts to. A whole myriad of theories have been proposed with widely different motivations and implications. For example[1], some theories modify GR by introducing new scalar degrees of freedom, such as Horndeski gravity [118] and dynamical Cherns-Simons gravity (dCS) [13]. Others introduce new vector degrees of freedom like Einstein-Aether gravity [82], new tensor degrees of freedom like massive gravity [68], and some introduce, scalar, vector, and tensor degrees of freedom like MOG [144]. In contrast, some theories

---

[1] This is by no means an extensive list; see [85] for a (more) extensive list.

include no new degrees of freedom, but generalize Einstein-Hilbert action to have higher-order curvature invariants like $f(R)$ gravity. The choice of theory to be explored can be guided by requiring it to have the desirable mathematical properties, such as being able to define a well-posed initial value problem, having second order in derivatives evolution equations, and being free of pathologies. However, this can be significantly restraining; the number of theories in which such properties are satisfied is quite limited. Horndeski theories are a stellar example in that regard; they constitute the sole class of theory which, by introducing a non-minimally coupled scalar field, retains second-order equations of motion. These theories, however, can suffer from pathologies that can render the problem ill-posed [161, 29, 86]. In those cases, after significant theoretical effort, appropriate new gauges were formulated [129, 128] that, in the small coupling limit, ameliorate these issues to the point where nonlinear studies of compact binary mergers are possible [81, 66, 19, 79]. An alternative perspective on this matter arises when considering that theories of interest (and GR itself) may serve as effective descriptions [44, 77] of gravitational phenomena only up to a certain energy or curvature scale. Pathologies and the challenges in defining a well-posed initial value problem could be attributed to the inherent incompleteness of the theory. However, a method capable of alleviating these pathologies and enabling accurate predictions within the desired regime and scales would expand the realm of testable theories. Exploring and pursuing such a method serve as a central objective of this thesis, and we will delve deeper into this aspect in subsequent sections. In this context and aligning with the aforementioned mindset, the Effective Field Theory (EFT) framework emerges as an ideal formalism for constructing extensions to GR [84, 71, 162]. The construction of such theories involves the addition of terms to the Einstein-Hilbert action, which are formed from powers of curvature invariants and conform to all the symmetries and assumptions of the desired theory. These additional terms are then appropriately suppressed by powers of a chosen cutoff scale Λ, resulting in a perturbative expansion that avoids introducing new light degrees of freedom and that can capture the underlying theory's physics below the cutoff. This methodology provides a comprehensive approach to testing modifications to GR in a general manner. If gravity is modified at the scale Λ, such that departures from GR can be detected through gravitational wave experiments, and the EFT remains valid in this regime, this methodology can be employed to model and detect these deviations. Furthermore, the knowledge gained from such detections can guide theoretical efforts in the search for a fundamental theory of gravity. One of the drawbacks of working with such theories is that the field equations obtained from them generally possess fourth-order spacetime derivatives of the metric and, therefore, can give rise to the previously discussed ill-posedness problems.

The primary objective of this thesis is to develop and implement mathematical and numerical techniques to study deviations from GR in the nonlinear regime. To test these methodologies, we will implement them to investigate the nonlinear dynamics of higher derivative EFT extensions to GR. We will employ innovative techniques to address the mathematical and practical challenges associated with these extensions. Specifically, we will utilize the *Fixing the Equations* method (refer to section 3.1) to effectively manage spurious higher frequencies and use an approach known as *Order reduction* (refer to section 3.2) to handle higher time derivatives in the equations. These novel techniques will enable us to tackle challenging scenarios involving the dynamics of BH spacetimes. Initially, we will work in simplified scenarios such as spherical symmetry, and subsequently, we will extend our work to confront the binary BH merger case.

The following notation is adopted throughout the thesis: The beginning of the Latin alphabet $(a, b, c, d, ...)$ will be used to denote full spacetime indices, while the Latin letters $(i, j, k, l...)$ will be used to indicate spatial ones. The metric $(-, +, +, +)$ signature is used, and geometric units are adopted, where the speed of light is set to $c = 1$ and the gravitational constant is set to $G = 1$.

1.1 Outline

Chapter 2 will provide a comprehensive review of essential background material and fundamental concepts that play a crucial role throughout this thesis. We will start with a concise overview of Einstein's theory of GR, including a discussion of Einstein's field equations. Subsequently, we will introduce the concept of a well-posed initial value problem and establish its significance in the numerical evolution of GR. This will be followed by an introduction to EFT as a powerful tool for constructing theories beyond GR. The chapter will finish by discussing results concerning black hole (BH) solutions and constraints on couplings within such theories.

Chapter 3 will introduce some of the mathematical and numerical techniques we implement to enable nonlinear studies in modified gravity theories. First, an introduction and motivation to the *Fixing the equations* methodology will be presented. The chapter will culminate with the introduction of a technique called *Order reduction* to address challenges related to higher derivatives and ghosts.

Chapter 4 covers a study of black hole dynamics in a higher derivative extension to General Relativity and presents a fully nonlinear/non- perturbative treatment to construct initial data and study its dynamical behavior in spherical symmetry when coupled to a massless scalar field. For initial data, we compare the obtained solutions with those from alternative treatments that rely on a perturbative (or iterative) approach. For the future evolution of such data, we implement an approach that addresses mathematical pathologies brought in by the higher derivatives. Our solutions demonstrate the presence of unexpected phenomena—when seen from the lens of General Relativity, as well as departures from General Relativity in the quasi-normal mode behavior of the scalar field scattering off the black hole.

Chapter 5 covers a follow-up work to Chapter 4. In this instance, we treat the evolution of black holes merging in quasi-circular orbits for the same higher-derivative EFT extension to GR treated in Chapter 4. This more general and demanding scenario requires further considerations not arising in the simplified regimes explored in Chapter 4. To build up to the binary scenario, we first study a simplified prototypical example as well as the single-boosted BH scenario. With these new considerations, we are able to carry out simulations in the binary merger scenario and study the effects of modifications on the dynamics and the GW emission.

Chapter 6 covers a study of gravitational collapse in Quadratic gravity, which in the presence of matter fields, is the leading order correction to GR from an EFT point of view. The matter content of the spacetime is that of a massless scalar field, which is set to collapse into a BH in spherical symmetry. The additional degrees of freedom associated with the higher derivatives in this theory are removed by an Order Reduction approach, where the truncated expansion nature of the theory is exploited. Through simulations, we study whether solutions remain within the bounds of the EFT and look for significant deviations from General Relativity during the collapse. Limitations of the approach taken, the EFT approximation, and the appearance of instabilities are also discussed.

The thesis finishes in Chapter 7 with an outlook and future directions.

Chapter 2

Background Material

2.1 General Relativity

Newtown's theory of gravitation was inconsistent with Einstein's new theory of Special Relativity since it contains instantaneous influence between bodies. This incompatibility and some key ideas and observations led Einstein to develop GR. The first of these ideas was the equivalence principle, which states that all bodies are influenced by gravity and that all bodies fall precisely the same way in a gravitational field. In Newtown's gravity, this idea manifests in the fact that the gravitational force on a body is proportional to its inertial mass. Freely falling bodies define a set of preferred curves in spacetime, just as geodesics of the flat metric did in Special Relativity. This resonates with the idea that freely falling bodies describe the geodesics of spacetime which deviate from the flat ones in the presence of matter. The presence of matter ties in perfectly with the second idea that motivated GR; this is Mach's principle which proposes that the distribution of all matter in the universe influences the inertial properties of matter. In other words, Mach's principle stated that the concept of a non-accelerating or non-rotating has no meaning in a universe without matter. Guided by these ideas, Einstein postulated that spacetime is a four-dimensional manifold with a metric of Lorentzian signature g_{ab} and that the curvature of g_{ab} is related to the matter distribution in spacetime through Einstein's field equations, which read,

$$G_{ab} \equiv R_{ab} - \frac{1}{2} R g_{ab} = 8\pi T_{ab}, \tag{2.1}$$

where G_{ab} is the Einstein tensor, R_{ab} and R are the Ricci tensor and scalar, which are derived from the Riemann curvature tensor defined as,

$$R_{abc}{}^{d} = \frac{\partial}{\partial x^b}\Gamma^{d}{}_{ac} - \frac{\partial}{\partial x^a}\Gamma^{d}{}_{bc} + \Gamma^{e}{}_{ac}\Gamma^{d}{}_{eb} - \Gamma^{e}{}_{bc}\Gamma^{d}{}_{ea}, \tag{2.2}$$

$$R_{ab} = R^{c}{}_{acb}, \tag{2.3}$$

$$R = R^{a}{}_{a}, \tag{2.4}$$

where $\Gamma^{c}{}_{ab}$ are the Christoffel symbols defined as,

$$\Gamma^{c}{}_{ab} = \frac{1}{2} g^{cd}\left(\partial_a g_{bd} + \partial_b g_{ad} - \partial_d g_{ab}\right), \tag{2.5}$$

which is in turn associated with the covariant derivative operator ∇_a and the coordinate system used to define the partial derivative ∂_a. For example, the covariant derivative acting on a vector can be written as,

$$\nabla_a v^b = \partial_a v^b + \Gamma^{b}{}_{ac} v^c. \tag{2.6}$$

Geodesics in a curved spacetime are the equivalent of straight lines of flat spacetime, and free particles follow them in accordance with the geodesics equation. For a particle with a spacetime velocity $u^a = \partial x^a/\partial t$ at spacetime coordinates $x^a(t)$ the geodesic equation reads,

$$\frac{d^2 x^a}{dt^2} + \Gamma^{a}{}_{bc}\frac{dx^b}{dt}\frac{dx^c}{dt} = 0. \tag{2.7}$$

Einstein's Field equations relate the curvature of spacetime to the energy-momentum tensor T_{ab} of the matter fields. The structure and dynamics of spacetime are directly intertwined with the presence and dynamics of matter in the universe, which is reminiscent of Mach's idea of the relevance of matter in the very notion of states of motion.

Through the contracted Bianchi identity, namely, $\nabla^a G_{ab} = 0$, we obtain that $\nabla^a T_{ab} = 0$. This last equation dictates the dynamics of matter fields in spacetime, which reduces to the geodesics equation when this matter is described by sufficiently small bodies whose self-gravity is weak enough.

It is pertinent (especially for what comes in section 2.2) to highlight the mathematical essence of Einstein's equations (2.1). Choosing coordinates and expressing everything in terms of the metric g_{ab}, Einstein's equations are equivalent to a nonlinear second-order partial differential system of equations for the metric components of g_{ab}. Solutions to the linearized Einstein's equations, which describe wave-like solutions of perturbations on flat spacetime, are known as gravitational waves.

2.1.1 Gravitational waves

Gravitational waves are solutions to the linearized Einstein's equations around a flat background spacetime. In this section, we will shortly review a derivation of such solutions. Perturbations to the flat metric can be incorporated at linear order by considering the perturbed metric (and its inverse),

$$g_{ab} = \eta_{ab} + h_{ab}, \quad g^{ab} = \eta^{ab} - h^{ab}, \tag{2.8}$$

where η_{ab} is the flat metric, and h_{ab} the perturbation. To linear order in h_{ab}, the Einstein tensor G_{ab} can be written as,

$$G^{(1)}_{ab} = \partial^c \partial_{(a} h_{a)c} - \frac{1}{2}\partial_c \partial^c h_{ab} - \frac{1}{2}\partial_a \partial_b h - \frac{1}{2}\eta_{ab}\left(\partial^c \partial^d h_{cd} - \partial^c{}_c h\right), \tag{2.9}$$

where $h = h_a{}^a$. Defining $\bar{h}_{ab} \equiv h_{ab} - 1/2\eta_{ab}h$ and replacing it on (2.9) simplifies the linearization of Einstein's equations to,

$$G^{(1)}_{ab} = \frac{1}{2}\partial^c \partial_c \bar{h}_{ab} + \partial^c \partial_{(b} \bar{h}_{a)c} - \frac{1}{2}\eta_{ab}\partial^c \partial^d \bar{h}_{cd} = 8\pi T_{ab}. \tag{2.10}$$

Thanks to the diffeomorphism invariance of GR, two metric perturbations $\widetilde{h}_{ab}$ and h_{ab} represent the same physical perturbation as long as they are related by,

$$\widetilde{h}_{ab} = h_{ab} - \partial_a \zeta_b + \partial_b \zeta_a, \tag{2.11}$$

where ζ^a is the vector field generating the infinitesimal diffeomorphism (e.i, change or coordinates) $\widetilde{x}^a = x^a + \zeta^a$. This sets the gauge freedom of the linearized perturbation. This gauge freedom can be used to impose the Lorentz gauge condition

$$\partial_a \bar{h}^{ab} = 0. \tag{2.12}$$

This choice further simplifies (2.10) to

$$\partial^a \partial_c \bar{h}_{ab} = -16\pi T_{ab}. \tag{2.13}$$

There is, however, residual gauge freedom, transformations satisfying $\partial_b \partial^b \zeta^a = 0$ will still satisfy the Lorentz gauge. Solutions of the source-free ($T_{ab} = 0$) linearized Einstein's equations $\partial^a \partial_c \bar{h}_{ab} = 0$ can be found without loss of generality, as plane waves,

$$\bar{h}_{ab} = A_{ab} e^{ik_c x^c} + c.c., \tag{2.14}$$

where A_{ab} is a constant polarization tensor, the wavevector k^a satisfies $k^a k_a = 0$ (e.i. a null-vector), and c.c. is the complex conjugate of the first term. Considering for concreteness that $k_a = (1, 0, 0, 1)$, using the gauge freedoms previously discussed and some algebra, it can be shown that the polarization tensor A_{ab} (in the traceless-transverse gauge) takes the form,

$$A_{ab} = \begin{bmatrix} 0 & 0 & 0 & 0 \\ 0 & h_+ & h_x & 0 \\ 0 & h_x & -h_+ & 0 \\ 0 & 0 & 0 & 0 \end{bmatrix}, \tag{2.15}$$

where h_+ and h_x are the two independent transverse polarizations. With this, we can conclude that gravitational waves propagating in flat spacetime have only two propagating degrees of freedom.

The generation, rather than propagation, of gravitational waves from matter sources can be described by the famous quadrupole formula, which in the traceless transverse gauge is

$$h_{ij}^{TT} = \frac{2G}{c^4 r} \mathcal{P}_{ij}{}^{kl} \ddot{Q}_{kl}, \tag{2.16}$$

where Q_{ij} is the quadrupole tensor defined as,

$$Q_{ij} = I_{ij} - \frac{1}{3} I^k{}_k \delta_{ij}, \quad I_{ij} = \int d^3x' T^{tt} x'^i x'^i, \tag{2.17}$$

and $P_{ij}{}^{kl} \equiv P_i{}^k P_k{}^l - \frac{1}{2} P_{ij} P^{kl}$. This result shows that the dominant contribution to gravitational radiation comes from the rate of change of the quadrupole moment of the source. Sources like compact binary mergers generate GWs, and interferometers from the LVK collaboration were designed to be able to detect them in the 10Hz to 10kHz frequency regime. These signals are buried in noise; a way to detect them is by matching the data to GW templates of binary merger events. To obtain such templates, perturbation theory can be used to describe the inspiral regime, where velocities are small, and the objects are far apart, as well as the ringdown part, which comes after the merger where the solution can be described by oscillations of a perturbed BH. However, in the merger, when perturbation theory is not valid, and the full nonlinear problem needs to be solved, we resort to numerical simulations. In the following sections, we will discuss important aspects of solving Einstein's equations numerically.

2.2 Well-posedness and formulations of GR

In classical theories of physics, the behavior of the relevant fields is governed by systems of differential equations. If a theory can be formulated in a way in which appropriate initial data (which could be subject to the satisfaction of constraint equations) can be prescribed, and appropriate boundary data if needed, then the theory can be said to possess an initial boundary value formulation. A fundamental property that any desirable physical theory should have is to be able to be formulated as a well-posed initial value problem. The concept of well-posedness is crucial in various fields, including mathematics, physics, and numerical analysis, as it provides a solid mathematical foundation for studying and simulating dynamical systems. It ensures the stability and predictability of solutions, allowing for accurate and meaningful results in the analysis of physical phenomena. A well-posed problem is characterized by three key aspects: existence, uniqueness, and continuous dependence on the initial conditions. This last condition implies that small changes in the initial data result in correspondingly small changes in the solution. If these conditions were not met, given that our ability to specify initial conditions in an experiment and even numerically is limited, then it would be virtually impossible to make any meaningful physical prediction.

The condition of continuity on the initial data can be presented in a more mathematical and concrete way as Hadamard first presented in [109], where the continuity of a solution $u(t,x)$ on its initial data: $u_0(t,x) \equiv u(t_0,x)$, where t_0 is the initial time, can be expressed as:

$$||u|| \leq \alpha \exp(\beta t) ||u_0||, \tag{2.18}$$

where $||u||$ is a Sobolev-type norm, and α and β are constants that are independent of u_0.

2.2.1 Hyperbolicity and classification

In classical physics, the behavior and dynamics of the relevant fields of a system are formulated in terms of systems of partial differential equations (PDEs). Many of the most relevant systems in physics can be formulated (sometimes through introducing new variables) as a first-order linear system of PDEs. Given this, the classification of hyperbolic systems in this section will be written for this type of system[1]. First-order systems can be written in the following form,

$$\frac{\partial \boldsymbol{u}}{\partial t} = \boldsymbol{A}^j \frac{\partial \boldsymbol{u}}{\partial x^j} + \boldsymbol{B}\boldsymbol{u} \tag{2.19}$$

where, $\boldsymbol{u}$ is an m-dimensional vector of variables, x^j are real coordinates from $j = 1..N$, $\boldsymbol{A}^j$ from $j = 1..N$ and $\boldsymbol{B}$ are $m \times m$ matrices, and do not depend on derivatives of $\boldsymbol{u}$.

In Fourier space equation 2.19 can be written as,

$$\frac{\partial \widetilde{\boldsymbol{u}}}{\partial t} = \boldsymbol{P}(ik)\boldsymbol{u} \equiv \boldsymbol{P}_0(ik) + \boldsymbol{B}, \tag{2.20}$$

where $\boldsymbol{P}_0 = ik_j\boldsymbol{A}^j$ is called the *principal symbol.* The principal symbol will dominate in the high-frequency regime, where $|k|$ is large, and one can discard $\boldsymbol{B}$ in the well-posedness studies. The system can be then classified by studying the decomposition of the characteristic matrix defined as $\boldsymbol{\mathcal{P}} = \boldsymbol{A^j} n_j$ (here n_j is an arbitrary unit vector) into eigenvalues and eigenvectors. The first-order system is called :

- Weakly hyperbolic if, for all arbitrary n_j, $\boldsymbol{\mathcal{P}}$ has all real eigenvalues but lacks a complete set of eigenvectors.
- Strongly hyperbolic if, for all arbitrary n_j, $\boldsymbol{\mathcal{P}}$ is diagonalizable with real eigenvalues and the maxtix $\boldsymbol{T}_n$ that diagonalizes it and its inverse $\boldsymbol{T}_n^{-1}$ depend smoothly on n_j.
- Symmetric Hyperbolic if there exists a Hermitian, positive definite matrix $\boldsymbol{H}$ such that $\boldsymbol{H}\boldsymbol{\mathcal{P}}$ is Hermitian for any arbitrary n_j and that $\boldsymbol{H}$ is independent of n_j.

This classification is enough to give necessary and sufficient conditions for well-posedness. Strong and symmetric hyperbolicity systems give rise to a well-posed initial value problem. The initial value problem from weakly hyperbolic systems is typically ill-posed in the presence of the lower order terms $\boldsymbol{B}$.

---

[1] Hyperbolicity classifications of second-order PDEs are also possible; for details, see [107].

2.2.2 Formulations of GR

The importance of defining a well-posed initial value problem was alluded to in the previous section. A huge roadblock that the numerical relativity community suffered in performing complex numerical simulations of highly dynamical systems in full generality, such as evolving BH binary for many orbits until the merger, was that the formulations used were not well-posed ones. The Arnotwitt-Deser-Misner (ADM) formulation [20] is one of them. The ADM formulation relies on a $3+1$ decomposition of Einstein's equations [2]. The 3+1 decomposition consists of splitting the four-dimensional spacetime into space and time by choosing a particular coordinate time t with which we label the different space-like hypersurfaces that will foliate the four-dimensional spacetime. As displayed in Figure 2.1 the normal vector to each one of these surfaces is n_a defined as:

$$n_a = (-\alpha, 0, 0, 0), \tag{2.21}$$

where α is denoted the lapse function, it can be a function of both the label t and the spatial coordinates $\{x^i\}$ in the hypersurfaces and guarantees that $n_a n^a = -1$. The proper time between two hypersurfaces of labels t and $t+dt$ measured by an observer that moves along this normal direction (also known as Eulerian observers) is $d\tau = \alpha dt$. The coordinates $\{x^i\}$ are not necessarily carried from hypersurface to hypersurface by the normal vector n. The relative velocity between the Eulerian observer and the lines that correspond to constant spatial coordinates is denoted β^i and called the shift vector.

The three-dimensional metric induced in the spatial hypersurfaces is denoted by γ_{ij}, and the line element for the four-dimensional spacetime metric in adapted coordinates can be written as:

$$ds^2 = (-\alpha^2 + \beta^i \beta_i)dt^2 + 2\beta_i dt dx^i + \gamma_{ij} dx^i dx^j. \tag{2.22}$$

Another key ingredient in the 3+1 decomposition is the *extrinsic* curvature K_{ij}. In contrast to the intrinsic curvature given by the three-dimensional Riemann tensor defined in terms of the three-metric γ_{ij}, the extrinsic curvature encodes the information on how the vector n^a is parallel transported along a space-like hypersurface from one point to another. In other words, the extrinsic curvature K_{ij} gives a notion of how each one of these space-like hypersurfaces is "bent" inside the 4-dimensional spacetime by giving us a measure of the change of the normal vector under the parallel transport. The extrinsic curvature can be defined as:

---

[2] See [102] for an extended review on the subject.

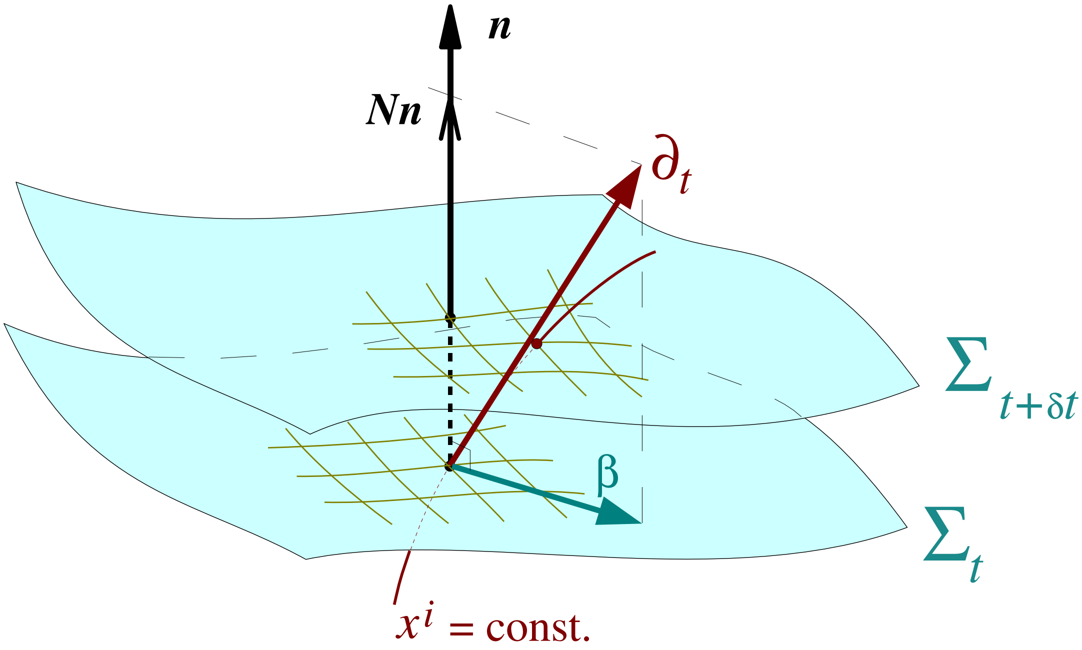

Figure 2.1: Spacetime is foliated by space-like hypersurfaces labeled with coordinate time t and with their corresponding set of spatial coordinates x^i. Image taken from [102]

.

$$K_{ij} := -P^a{}_i P^b{}_j \nabla_a n_b = -(\nabla_i n_j + n_i n^c \nabla_c n_j), \tag{2.23}$$

where $P^a{}_i$ is a projector operator onto the spatial hypersurfaces defined as,

$$P^a{}_i := \delta^a{}_i + n^a n_i. \tag{2.24}$$

The extrinsic curvature K_{ij} can be related to evolution equations of the spatial metric γ_{ij} as:

$$\partial_t \gamma_{ij} = -2\alpha K_{ij} + D_i \beta_j + D_j \beta_i, \tag{2.25}$$

where D_i is the covariant derivative associated to the spatial metric γ_{ij}.

This set of equations will be part of the evolution equations that determine the evolution of the system. It's important to notice that these equations have no information whatsoever about the field equations. To get a set of evolution and constraint equations, we must perform projections on Einstein's equations 2.1 onto the spatial hypersurfaces and the direction orthogonal to them. Let us now perform these projections to Einstein's equation when matter described by the tensor T_{ab} is present :

- The normal projection gives us the Hamiltonian constraint:

$$n^a n^b (G_{ab} - 8\pi T_{ab}) = 0. \tag{2.26}$$

- The mixed projection gives us the Momentum constraints:

$$P^b{}_a n^c (G_{cb} - 8\pi T_{cb}) = 0. \tag{2.27}$$

- The projection onto the hypersurface gives us the evolution equations :

$$P^c{}_a P^d{}_b (G_{cd} - 8\pi T_{cd}) = 0. \tag{2.28}$$

Equations (2.26 - 2.27) are together the 4 constraints equations of the theory; it becomes clear that no time derivatives are involved in these equations after writing them in terms of the 3+1 variables (e.i α, β,γ_{ij} and K_{ij}) and using the Gauss-Codazzi relations to write projections of the Riemann tensor. On the other hand, equations (2.28) correspond to six evolution equations, namely the evolution equations of the six independent components of the extrinsic curvature tensor K_{ij}. Equations (2.28) and (2.25) constitute together a set of twelve evolution equations known as the ADM equations; in the Smarr and York form [187, 172] they can be written as

$$\partial_\perp \gamma_{ij} = -2\alpha K_{ij} \tag{2.29a}$$

$$\partial_\perp K_{ij} = \alpha \left[R^{(3)}_{ij} - 2K_{ik}K^k_j + KK_{ij} \right] - D_i D_j \alpha - 8\pi G\alpha \left[S_{ij} - \gamma_{ij}(S-\rho)/2 \right] \tag{2.29b}$$

were the derivative operator $\partial_\perp$ is defined as $\partial_\perp = \partial_t - \mathcal{L}_\beta$, where $\mathcal{L}_\beta$ is the Lie derivative along the shift vector β^i. K is the trace of the extrinsic curvature defined as $K = \gamma^{ij} K_{ij}$, while S_{ij}, S and ρ are the matter variables constructed from the energy-momentum tensor T_{ab} as, $S_{ij} = P^a{}_i P^b{}_j T_{ab}$, it's trace $S = \gamma^{ij} S_{ij}$ and $\rho = n_a n_b T^{ab}$.

It turns out that, as shown in [145], the set of equations (2.29a-2.29b) together with the corresponding constraint equations is not well-posed since they are only weakly hyperbolic.

Formulations were developed to overcome such limitations. Among the most successful ones, there are those that have strong hyperbolicity properties, such as the Baumgarte-Shapiro-Shibata-Nakamura-Oohara-Kojima (BSSNOK) formulation [168, 25, 146] and the CCZ4 formulation [14, 15, 36, 37], and those which are symmetric hyperbolic such as the Generalized Harmonic (GH) formulation [91, 157, 135].

In this thesis, we use two of these formulations. In chapters 4 and 6, we implement a GH formulation, and in Chapter 5, we use a CCZ4 formulation. In what follows, we will review these formulations and their corresponding properties.

Generalized harmonic formulation

The GH formulation is a formulation that extends the original Harmonic formulation, which casts Einstein's equations into a system of wave equations when the gauge is fixed such that it satisfies the condition,

$$\nabla_a \nabla^a x^b = -g^{ac}\Gamma^b_{ac} = 0. \tag{2.30}$$

The generalization in the GH formulation is introduced by generalizing the wave equation that the coordinates have to satisfy into an inhomogeneous wave equation,

$$\nabla_a \nabla^a x^b = -g^{ac}\Gamma^b_{ac} = H^b(x,g), \tag{2.31}$$

where $H^a(x,g)$ is the gauge source vector, whose components are arbitrary functions of the coordinates x^a and the spacetime metric g_{ab}. Its value can be prescribed to impose gauge conditions suitable for the evolution of, for example, dynamical BH spacetimes. Then satisfying the GH gauge is equivalent to satisfying,

$$\mathcal{C}^a \equiv H^a(x,g) + \Gamma^a = 0, \tag{2.32}$$

We define also $\Gamma^a := g^{bc}\Gamma^a{}_{bc}$ is the trace of the Christoffel symbols Γ^a_{bc}. The generalized harmonic equations take the form,

$$R_{ab} - \nabla_{(a}\mathcal{C}_{b)} = -\kappa\left[n_{(a}\mathcal{C}_{b)} - g_{ab}n^c\mathcal{C}_c/2\right] + 8\pi G\left[T_{ab} - g_{ab}T^c{}_c/2\right]. \tag{2.33}$$

These equations are equivalent to Einstein's equations when the constraint defined by equation (2.32) $\mathcal{C}^a = 0$ is satisfied. Ensuring that this constraint is under control is essential. From the contracted Bianchi identities, it can be shown that $\mathcal{C}$ satisfies the following wave-like equation,

$$\nabla^a \nabla_a \mathcal{C}^b = -R^b{}_a \mathcal{C}^a - 16\pi G \nabla_a T^{ab}. \tag{2.34}$$

Since the energy-momentum tensor is covariantly conserved (e.i. $\nabla_a T^{ab} = 0$), this implies that if initial data is prescribed such that $\mathcal{C}^a = \partial_t \mathcal{C}^a = 0$ initially, then $\mathcal{C}^a = 0$ for all t. These conditions are equivalent to giving initial data such that $\mathcal{C}^a = 0$, and the Hamiltonian (2.26) and Momentum (2.27) constraints are satisfied initially. Due to numerical limitations, it is impossible to prescribe initial data in which such conditions are met exactly. Furthermore, numerical truncation can trigger growth in constraint violations during the evolution. The first term on the right-hand side has been introduced to deal with those issues; it is a constraint-damping term [40, 108, 156] whose job is to damp violations of the constraint $\mathcal{C}^a = 0$. When these equations are written in terms of the metric components, the principal part of the equation (second derivatives in this case) is a set of wave-like equations, and then, given reasonable gauge conditions, the system is symmetric hyperbolic.

CCZ4 formulation

The CCZ4 (Conformal covariant of the Z4) formulation is a formulation that combines the advantages of conformal decompositions such as BSSNOK and the advantages of formulations where constraints are damped. Starting from the damped version of the Z4 formulation [108], Einstein's equations can be written as,

$$R_{ab} + \nabla_a Z_b + \nabla_b Z_a + \kappa_1 \left[n_a Z_b + n_b Z_a - (1+\kappa_2) g_{ab} n_c Z^c) \right] = 8\pi \left(T_{ab} - \frac{1}{2} T g_{ab} \right). \tag{2.35}$$

Here, the usual constraints of GR are transformed into algebraic conditions for the new four-vector Z^a. Satisfaction of the constraints $Z^a = 0$ amounts to the usual Hamiltonian and Momentum constraints being satisfied, as well as equations (2.35) being equivalent to Einsteins' equations. The κ_i parameters determine the characteristic time of the exponential damping of constraint violations. In the 3+1 decomposition of (2.35) the CCZ4 formulation also performs conformal decompositions of the relevant fields as done in the BSSNOK formulation. The spatial metric γ_{ij} is decomposed into conformal metric $\widetilde{\gamma}_{ij}$, with unit determinant, and its conformal factor χ,

$$\widetilde{\gamma}_{ij} = \chi \gamma_{ij}. \tag{2.36}$$

The extrinsic curvature first is decomposed into its traceless part A_{ij} and its trace K, and these are subsequently conformally decomposed as,

$$K_{ij} = \chi^{-1}\left(\widetilde{A}_{ij} + \frac{1}{3}\widetilde{\gamma}_{ij}K\right), \tag{2.37}$$

where $\widetilde{A}_{ij} = \chi A_{ij}$. Furthermore, the Z^a are decomposed into its normal and spatial components to define to following variables,

$$\Theta \equiv -n_a Z^a, \tag{2.38}$$

$$\hat{\Gamma}^i \equiv \widetilde{\Gamma}^i + 2\widetilde{\gamma}^{ij}Z_j, \tag{2.39}$$

where, $\widetilde{\Gamma}^i \equiv \widetilde{\gamma}^{jk}\widetilde{\Gamma}^i{}_{jk} = \widetilde{\gamma}^{ij}\widetilde{\gamma}^{kl}\partial_l\widetilde{\gamma}_{jk}$. The resulting system is a strongly hyperbolic one. With these definitions, the evolution equations written in first-order form are,

$$
\begin{aligned}
\partial_t\widetilde{\gamma}_{ij} &= -2\alpha\widetilde{A}_{ij} + 2\widetilde{\gamma}_{k(i}\partial_{j)}\,\beta^k - \frac{2}{3}\widetilde{\gamma}_{ij}\partial_k\,\beta^k + \beta^k\partial_k\widetilde{\gamma}_{ij}\,, && (2.40)\\
\partial_t\widetilde{A}_{ij} &= \chi\left[-\nabla_i\nabla_j\alpha + \alpha\left(R_{ij} + \nabla_i Z_j + \nabla_j Z_i - 8\pi S_{ij}\right)\right]^{\mathrm{TF}} + \alpha\tilde{A}_{ij}\left(K - 2\Theta\right)\\
&\quad -2\alpha\widetilde{A}_{il}\widetilde{A}^l{}_j + 2\widetilde{A}_{k(i}\partial_{j)}\,\beta^k - \frac{2}{3}\widetilde{A}_{ij}\partial_k\,\beta^k + \beta^k\partial_k\widetilde{A}_{ij}\,, && (2.41)\\
\partial_t\chi &= \frac{2}{3}\chi\left(\alpha K - \partial_i\beta^i\right) + \beta^k\partial_k\chi, && (2.42)\\
\partial_t K &= -\nabla^i\nabla_i\alpha + \alpha\left(R + 2\nabla_i Z^i + K^2 - 2\Theta K\right) + \beta^j\partial_j K - 3\alpha\kappa_1\left(1+\kappa_2\right)\Theta\\
&\quad +4\pi\alpha\left(S - 3\rho\right)\,, && (2.43)\\
\partial_t\Theta &= \frac{1}{2}\alpha\left(R + 2\nabla_i Z^i - \widetilde{A}_{ij}\widetilde{A}^{ij} + \frac{2}{3}K^2 - 2\Theta K\right) - Z^i\partial_i\alpha + \beta^k\partial_k\Theta\\
&\quad -\alpha\kappa_1\left(2+\kappa_2\right)\Theta - 8\pi\alpha\,\rho\,, && (2.44)\\
\partial_t\hat{\Gamma}^i &= 2\alpha\left(\widetilde{\Gamma}^i{}_{jk}\widetilde{A}^{jk} - \frac{3}{2}\tilde{A}^{ij}\frac{\partial_j\chi}{\chi} - \frac{2}{3}\widetilde{\gamma}^{ij}\partial_j K\right) + 2\widetilde{\gamma}^{ki}\left(\alpha\partial_k\Theta - \Theta\partial_k\alpha - \frac{2}{3}\alpha K Z_k\right) - 2\widetilde{A}^{ij}\partial_j\alpha\\
&\quad +\widetilde{\gamma}^{kl}\partial_k\partial_l\beta^i + \frac{1}{3}\widetilde{\gamma}^{ik}\partial_k\partial_l\beta^l + \frac{2}{3}\widetilde{\Gamma}^i\partial_k\beta^k - \widetilde{\Gamma}^k\partial_k\beta^i + 2\kappa_3\left(\frac{2}{3}\widetilde{\gamma}^{ij}Z_j\partial_k\beta^k - \widetilde{\gamma}^{jk}Z_j\partial_k\beta^i\right)\\
&\quad +\beta^k\partial_k\hat{\Gamma}^i - 2\alpha\kappa_1\widetilde{\gamma}^{ij}Z_j - 16\pi\alpha\widetilde{\gamma}^{ij}S_j, && (2.45)
\end{aligned}
$$

where the term proportional to κ_3 is an additional damping term. The constraints are,

$$
\begin{aligned}
Z_a &= 0, && (2.46)\\
det(\widetilde{\gamma}_{ij}) &= 1, && (2.47)\\
tr(\widetilde{A}_{ij}) &= 0. && (2.48)
\end{aligned}
$$

The gauge conditions for α and β^i are still unspecified. The prescription of adequate gauge conditions is essential for achieving controlled long evolutions in dynamical spacetimes, particularly in the presence of BHs. Conditions on the lapse function α are called slicing conditions; among the most popular ones, there is the called 1 +log slicing, along with others in the Bona-Masso family on conditions [38]. This type of slicing condition achieves a collapse of the lapse function, which forces the lapse function to approach zero close to singularities; this slows the "clocks" of observers approaching the singularity, hence avoiding the fall of such observers into them, since if this were to happen it would be catastrophic for the simulations. Conditions on the shift β^i are called shift conditions; one of the most popular choices for such conditions is the Gamma-driver shift condition [12], which solves the problem of "slice stretching" due to the difference in the value of the lapse function in regions close to BHs and the far regions.

2.3 Effective Field Theory in gravitational physics

As mentioned in the introduction, EFT can be used as a guiding principle for constructing extensions to GR. In general terms, EFT is a framework used to systematically describe physical phenomena by incorporating the effects of higher-energy scales via introducing a tower of local operators built from the lower-energy theory operators. This technique comes in two flavors. The first one is commonly denoted "Top-down "approach, in which the high-energy theory is known, and the "heavy" fields are integrated out in favor of operators built from the "light" fields to have a simpler description of the physics at low energies [3]. The second one is called the "Bottom-up" approach, in which the high-energy theory is unknown, and the low-energy degrees of freedom of the theory are used to construct an effective action that contains the effects of the heavy fields as a collection of operators of increasing dimensionality which are adequately suppressed by a cut-off scale. The "bottom-up" approach is particularly useful because it allows exploring new physics without requiring a complete and detailed understanding of the underlying fundamental

---

[3] This approach has gained traction in the computation of gravitational radiation in the spiral of compact objects within GR, these are commonly denoted Worldline Effective Theories [154, 100].

theory. In the context of extensions to GR relativity, the "bottom-up" approach can allow us to construct the most general extensions to GR under a desired set of assumptions. In gravity, the operators added to the Einstein-Hilbert action are terms formed from curvature invariants. Depending on the number of derivatives of the metric they contain (usually denoted dimensionality), they will be suppressed by the corresponding power of the lengthscale cut-off Λ^{-1}. As EFT describes a perturbative approach, there is a hierarchy of these terms, where the lower dimensionality terms dominate over terms with larger dimensionality. The leading order corrections to GR should then be encoded on Riemann squared terms, called the dimension-four operators, in the following way,

$$S_{\text{eff}} = \frac{1}{16\pi G}\int d^4x\sqrt{-g}\left(R + \frac{a_1}{\Lambda^2}R_{ab}R^{ab} + \frac{a_2}{\Lambda^2}R^2 + \frac{a_3}{\Lambda^2}R_{abcd}R^{abcd} + \cdots\right). \tag{2.49}$$

These are the same operators that are used to construct the well-known Gauss-Bonnet invariant, $\mathcal{G} = R^2 - 4R_{ab}R^{ab} + R_{abcd}R^{abcd}$. If the spacetime dimension is $D = 4$, $\mathcal{G}$ is a total derivative and hence topological and does not contribute to the field equations. This fact can be used to essentially remove one of the dimension-four terms from the definition of the effective action (2.49). For reasons that will become evident in just a moment, the term proportional to a_3 will be eliminated, giving then,

$$S_{\text{eff}} = \frac{1}{16\pi G}\int d^4x\sqrt{-g}\left(R + \frac{\widetilde{a}_1}{\Lambda^2}R_{ab}R^{ab} + \frac{\widetilde{a}_2}{\Lambda^2}R^2 + \cdots\right). \tag{2.50}$$

If the spacetime of interest is absent of matter fields, then one can show that these terms will not contribute to the field equations. This can be shown using a field redefinition given by:

$$g_{ab} \to g_{ab} + \frac{\widetilde{a}_1}{\Lambda^2}\left(R_{ab} - \frac{1}{2}Rg_{ab}\right) - \frac{\widetilde{a}_2}{\Lambda^2}Rg_{ab} \tag{2.51}$$

which changes (2.50) to,

$$\begin{aligned} S_{\text{eff}} &= \frac{1}{16\pi G}\int d^4x\sqrt{-g}\left(R + \frac{\widetilde{a}_1}{\Lambda^2}R_{ab}R^{ab} + \frac{\widetilde{a}_2}{\Lambda^2}R^2 - R^{ab}\left(\frac{\widetilde{a}_1}{\Lambda^2}R_{ab} + \frac{\widetilde{a}_2}{\Lambda^2}Rg_{ab}\right) + \cdots\right) \\ &= \frac{1}{16\pi G}\int d^4x\sqrt{-g}\left(R + \cdots\right), \end{aligned} \tag{2.52}$$

hence no modification to GR enters through dimension-four operators in vacuum scenarios. This can also be seen explicitly by varying the action (2.50) and computing the field equations. All terms modifying Einstein's equations are proportional to R_{ab} and R. Schematically,

$$R_{ab} - \frac{1}{2} g_{ab} R = \frac{1}{\Lambda^2} M(R_{ab}, R), \tag{2.53}$$

where $M(R_{ab}, R)$ are the terms modifying Einstein's equations and are proportional to at least R_{ab} or R. From this we can clearly read that $R_{ab} = R = 0 + \mathcal{O}(\Lambda^{-2})$. Then one uses this to replace the Ricci terms on the RHS of (2.53) to give,

$$R_{ab} - \frac{1}{2} g_{ab} R = \frac{1}{\Lambda^4} \widetilde{M}(R_{ab}, R) + \mathcal{O}(\Lambda^{-6}). \tag{2.54}$$

This process can then be iterated to show that contributions to the field equations from 4-dimensional operators can always be pushed to a higher order in the perturbative expansion.

The story changes when matter is present; the field redefinition (2.51) can not eliminate modifications to GR. Instead, field redefinitions would introduce terms mixing the energy-momentum tensor of the matter field T_{ab} and the Ricci tensor/scalar. This would then modify GR by including non-minimally coupled matter fields. In chapter 6, when we work with spacetimes where matter is present, these terms represent the leading order corrections. Constraints of $\Lambda^{-1} \lesssim 1$ km [18, 73] for these theories can be obtained through neutron stars observations and study of the mass-radius relations within the modified theory.

In chapters 4 and 5, we will work in vacuum spacetimes. In such cases, using the fact that all Ricci terms can be eliminated through field redefinitions, the most general effective action can be written as,

$$\begin{split} S_{\text{eff}} = \frac{1}{16\pi G} \int d^4x \sqrt{-g} \bigg(R + \frac{b_1}{\Lambda^4} R_{ab}{}^{ef} R^{abcd} R_{cdef} + \frac{b_2}{\Lambda^4} R_{ab}{}^{ef} R^{abcd} \widetilde{R}_{cdef} + \\ + c_1 \frac{1}{\Lambda^6} \mathcal{C}^2 + c_2 \frac{1}{\Lambda^6} \widetilde{\mathcal{C}}^2 + c_3 \frac{1}{\Lambda^6} \mathcal{C}\widetilde{\mathcal{C}} + \cdots \bigg), \end{split} \tag{2.55}$$

where $\mathcal{C} \equiv R_{abcd} R^{abcd}$ and $\widetilde{\mathcal{C}} \equiv R_{abcd} \widetilde{R}^{abcd}$, with $\widetilde{R}_{abcd} = \epsilon_{ab}{}^{ef} R_{efcd}$. Here the terms proportional to Λ^{-4} are dimension six-operators, which are the leading corrections in the effective action in the vacuum case. The next to leading order terms are given by the dimension-eight operators[4], which are proportional to Λ^{-6}. The terms proportional to b_2 and c_3 are parity violating terms.

In this thesis, we will focus mainly on the dimension-eight operators. The reason for not pursuing studies for the leading order dimension-six operators is historical and practical. Starting with the historical side of things, when we first started working with these theories, there were some suggestions that dimension-six operators were disfavored from causality arguments. The consensus at the moment is that 6-dimensional operators are not disfavored, and they should be considered in the effective action. On the practical side, the field equations from the dimensional-eight operator theory are simpler than those from the dimension-six one. The former introduces higher-order metric derivatives only through a second covariant derivative of scalar quantity, namely $\mathcal{C}$. In contrast, the latter introduces them through covariant derivatives of the Riemann tensor. This fact is helpful in treating the dimension-eight theory in chapter 5. However, we acknowledge that in this EFT prescription, dimension-six operators are the leading contributions and naturally should be the first deviations to look for. We will apply what we learned from the dimension-eight operator theory to future studies we will conduct on the dimension-six operator theory.

2.3.1 Black hole solutions and corrections

It is possible to find BH solutions for this EFT extension of GR. In [54] approximate (valid to first order in Λ^{-6}) solutions are found for the dimension-eight theory. BH solutions to the dimension-six theory can also be found in [69]. In this section, we will focus on the spherically symmetric solutions. Slowly rotating solutions have also been derived in [54, 53]. Following [54], we will review the process of finding such solutions and their physical implications. In spherical symmetry and for static solutions, the only non-vanishing contributions come from the c_1 proportional term in (2.55). Consequently, in what follows, we will only consider the theory coming from dimension-eight operators and $c_1 = -1$ and $c_2 = c_3 = 0$. In that setting, the field equations obtained from variation of the action are given by.

$$G_{ab} = \frac{1}{\Lambda^6}\Big(4\,\mathcal{C}\,R_a{}^{cde}R_{bcde} - \frac{1}{2}g_{ab}\mathcal{C}^2 + 8R_a{}^c{}_b{}^d\nabla_d\nabla_c\mathcal{C}\Big), \tag{2.56}$$

---

[4] These types of operators are known to emerge in low-energy EFT expansions of string theories, see [143] for dimension-six operators, and [124, 123, 104, 103, 26] for dimension-eight operators.

Taking the following metric ansatz for the line element,

$$ds^2 = -\left(1 - \frac{2M}{r} + \frac{f_t(r)}{\Lambda^6 M^6}\right) dt^2 + \left(1 - \frac{2M}{r} + \frac{f_r(r)}{\Lambda^6 M^6}\right)^{-1} dr^2 + r^2 \left(d\theta^2 + sin^2\theta d\phi^2\right) \tag{2.57}$$

and plugin it in (2.56) and truncating after first order in $(\Lambda M)^{-6}$ leads to a system of ordinary differential equations for $f_t(r)$ and $f_r(r)$. The solution of such a system is given by,

$$f_t(r) = -128\left(8\frac{M^9}{r^9} - 11\frac{M^{10}}{r^{10}}\right), \tag{2.58}$$

$$f_r(r) = -128\left(36\frac{M^9}{r^9} - 67\frac{M^{10}}{r^{10}}\right). \tag{2.59}$$

These solutions describe a BH spacetime. The event horizon of this BH is located at the radius,

$$r_H = 2M\left(1 + \frac{5}{8}(\Lambda M)^{-6}\right), \tag{2.60}$$

and M is the gravitational mass of the spacetime.

As shown in (2.58) and (2.59), corrections to the metric enter with large inverse powers of r, making modifications to weaken strongly as the distance to the BH increases. For example, the radius of the innermost stable circular orbit (ISCO) is also modified to,

$$r_{ISCO} = 6M\left(1 + \frac{1871}{157464}(\Lambda M)^{-6}\right), \tag{2.61}$$

which is ≈ 60 times weaker than the effect on the horizon. The new ISCO will also have a different frequency Ω_{ISCO} associated with it, and its given by,

$$M\Omega_{ISCO} = \frac{1}{6\sqrt{6}}\left(1 - \frac{5291}{314928}(\Lambda M)^{-6}\right). \tag{2.62}$$

which is smaller than the GR value since r_{ISCO} is larger for this choice of sign on c_1, naturally the opposite happens for the opposite sign of c_1.

Quantities such as Ω_{ISCO} can provide valuable insights in the context of binary mergers. This quantity, in the small mass-ratio limit, (e.i., $m_2/m_1 \to 0$), determines the frequency at which the binary system can no longer sustain orbits and undergoes a final plunge. If the plunge occurs at a lower(higher) frequency, it indicates that a smaller(larger) amount of the orbital angular momentum has been emitted through GWs, resulting in a final black hole with a higher(lower) angular momentum[5].

Another important characteristic of BHs is their quasinormal modes (QNMs) [126, 31]. QNMs are the solutions to the equations [176] that describe perturbations in the spacetime geometry of a BH. When a BH is perturbed, it emits gravitational waves to overtime settle into a stationary solution. A combination of damped oscillations can describe the emission of these GWs; the decay rate of such oscillations is determined by the imaginary part of the QNM frequency, while the real part determines the oscillatory part. In particular, QNMs can be used to describe the GW emission in the ringdown part of a BH binary coalescence waveform, where the BH remnant settles to a stationary configuration. The BH predicted by this EFT extension to GR has QNMs that differ from the ones predicted by GR. These modifications to the QNMs have been computed for spherically symmetric BHs and for slowly rotating ones in [54, 52]. For example, the QNM frequencies of the fundamental mode for an even $l = 2$ perturbation differ from GR as follows,

$$\omega_R = \omega_R^{GR}\left(1 + 0.45(\Lambda M)^{-6}\right), \tag{2.63}$$

$$\omega_I = \omega_I^{GR}\left(1 - 2.75(\Lambda M)^{-6}\right), \tag{2.64}$$

$$\tag{2.65}$$

where ω_R and ω_I are the real and imaginary parts of the frequency of the fundamental mode, respectively, and ω_R^{GR} and ω_I^{GR} are such frequencies for the GR BH. Naturally, the signs of these modifications are opposite with the opposite sign of c_1.

Another exciting feature of BHs in this EFT is regarding their Tidal Love Numbers (TLNs)[34, 67]. Tidal love numbers quantify how an object is deformed when placed in an external gravitational field, and an exciting result for GR BH is that their TLNs vanish. However, BHs in this theory possess non-vanishing love numbers [54], given by

---

[5] Following strategies such as [43] can help estimate the final dimensionless spin in BH coalescence in GR

$$\kappa_E = \frac{1008}{25} (\Lambda M)^{-6} , \tag{2.66}$$

$$\kappa_B = \frac{3072}{175} (\Lambda M)^{-6} , \tag{2.67}$$

where κ_E and κ_B are the electric and magnetic quadrupolar TLNs respectively.

The presence of non-vanishing TLNs impacts the GW radiation during the inspiral phase of compact binary mergers. In particular, the internal structure of neutron stars influences the phase of GWs during that regime, and such dependence is encoded in their TLNs. Detection of such signatures in the inspiral of NS waveforms can help constrain the nuclear equation of state. Furthermore, if signatures of non-vanishing TLNs are detected on objects believed to be BHs can help constrain the relevant parameters (like Λ) that modify GR. The dephasing in the waveforms of a compact binary merger with constituents that possess non-zero TLNs with respect to one in which the TLNs are vanishing is given by [89],

$$\delta\Psi(f) = -\frac{9}{16}\frac{v^5}{\mu M_T^4}\left[\left(11\frac{m_1}{m_2} + \frac{M_T}{m_1}\right)\lambda_1 + 1 \leftrightarrow 2\right], \tag{2.68}$$

where $\Psi(f)$ is the phase of the Fourier transform of the GW signal at a common frequency f, $v = (\pi M_T f)^{1/3}$ is the orbital velocity, M_T is the total mass of the binary, $\mu = \frac{m_1 m_2}{m1+m2}$ is the reduced mass, with m_1 and m_2 being the component masses. Here λ_1 is related to the TLN of the object with mass m_1. This relationship is given by, $\lambda = \frac{2}{3} R^5 G^{-1} \kappa_E$, where R is the radius of the object. This is a 5PN correction to the phase of the waveform, although, in the case of NS, it tends to be numerically larger (by $\approx (R/M)^5 \approx 10^5$) than the point-particle 5PN corrections. In the case of BHs with non-vanishing TLDs, we can not expect the same to play out since $R \approx 2M + \mathcal{O}(\Lambda M)^{-6}$.

Other PN corrections to the GW phase have been computed for the dimension-eight EFT of gravity [6]. Using the results from [84], a subsequent work [165] is able to compute the leading order (excluding finite-size effects) of the phase corrections to the waveform. This correction is given by,

$$\delta\Psi(f) = \frac{3}{128\nu v^5}\left(\frac{234240}{11} - \frac{522240}{11}\nu\right)(\Lambda M_T)^{-6} v^{16}, \tag{2.69}$$

---

[6] For results in the dimension-six operator EFT see [8].

where $\nu = m_1 m_2 / M_T^2$ is the symmetric mass ratio. The authors emphasize that this 8PN correction is numerically a 2PN correction when $v^2 \approx M_T \Lambda$ which happens when $r_{orbit}\Lambda^{-1} \approx 1$. This last argument is motivated by the author's choice of assuming a soft UV completion of the theory takes place in the case where $\Lambda^{-1} > r_s$, where r_s is the Schwarzschild radius of the smallest BH. When $\Lambda^{-1} > r_s$ the EFT makes no sense at the scales pertinent to the BH, a soft UV completion here implies the theory reduces back to GR (or sufficiently close to it) at those scales. When that assumption is in place, the relevant scale of the system to compare Λ^{-1} to is the radius of the orbit r_{orbit}. Such EFT will only be valid until $\Lambda^{-1} > r_{orbit}$, and corrections in the spiral can become strong (numerically as 2PN) in the regimes where $r_{orbit}\Lambda^{-1}$ is below but close to 1. If the soft UV completion does not take place, then the EFT is only valid for $\Lambda^{-1} < r_s$ and in such case, the dominant PN corrections come from the 5PN contributions from tidal effects as in (2.68).

Notice how all the discussed effects from modifying the theory are strongly enhanced as the mass of the BHs M decreases. This is expected since modifications in this theory come in as curvature operators, and the curvature at the horizon for BHs decreases with their mass. This generally tells us that for a given fundamental scale Λ, the strongest effects would be observed (provided that our experiments are sensitive to such regimes/frequencies) for the smallest BHs. In what follows, we will present the current constraints on the EFTs described by (2.55) in addition to some other theories where the corrections enter at a scale Λ and where corrections are suppressed by Λ^{-p} with $p = 4, 6$.

2.3.2 Current constraints

Let's start with the constraints on Λ for the dimension-eight operator EFT through the analysis of GW waves in the inspiral regime of the waveform. This analysis was performed in [165] by constructing waveforms considering the deviations to GR coming from (2.69) and performing Bayesian model selection using the data for two binary black hole events, GW151226 and GW170608 (which at the time were the lowest mass binaries reported LIGO-Virgo collaboration). The results from this work show that lengthscales Λ^{-1} between 70 and 200 km are strongly disfavored by the data. The predicted mass of the smallest component BH of these events was reported to be $m = 7.5 M_\odot \pm 2.3 M_\odot$; hence its radius would be $r_s \lessapprox 30$ km. Knowing this, disfavoring Λ^{-1} between 70 and 200 km is not a striking result. The authors emphasize that they focus on the $\Lambda^{-1} > r_s$ regime (under the assumption of a soft UV completion), where the dominant effects come from the dephasing corresponding to 2.69. Without a soft UV completion, the sort of couplings excluded by their analysis would strongly modify the BHs, and the EFT would no longer be valid. For such cases, we could expect waveforms to be wildly different from GR ones, which is not what we are observing.

We will continue by reporting constraints obtained using the ringdown part of GW data. The study conducted in [170] includes in the waveform model the quasinormal frequencies on a theory-by-theory basis. The theories considered include the six and dimension-eight EFTs of gravity and dynamical Chern-Simons (dCS) theory. The aforementioned waveform model is used to measure the ringdown properties of, at the time, the loudest signal-to-noise ratio events; GW150914 and GW200129. Their findings show for the dimension-eight EFT, the constraint is $\Lambda^{-1} \leq 51.3$ km and for the dimension-six theory $\Lambda^{-1} \leq 38.2$ km. For the relevant scale entering in dCS, they constraint $\Lambda_{dCS}^{-1} \leq 38.7$ km. Since beyond GR, effects are included in the ringdown of the waveforms, the relevant scale to compare Λ^{-1} to is the radius of the remnant BH. For both events, the final mass is $M \approx 60M_{\odot}$, giving a radius of $r_s \approx 180$ km. In contrast to the study conducted for the inspiral, in this case, the EFTs are still applicable (even for the component masses) for the constrained values of Λ^{-1}, which improve the ones obtained in [165]. A previous work [55] performed a similar analysis without a theory-by-theory incorporation of modifications to the ringdown portion of the waveform. In contrast, this work only assumes that the changes to the QNM's are proportional to $(\Lambda M)^{-p}$, where M is the mass of the remnant BH. By performing their analysis with a total of 17 GW events, the following constraints were drawn, for $p = 6$ (corresponding to the dimension-eight operator EFT) $\Lambda^{-1} \lesssim 42$ km, and for p=4 (corresponding to the dimension-six operator EFT and dCS) they constrain $\Lambda^{-1} \lesssim 35$ km.

These upper bounds on $\Lambda^{-1} \lesssim 40$ km are still quite large, considering that the smallest BH candidates observed by GW have components masses consistent with $m \approx 5M_{\odot}$, which would have a radius of $r_s \approx 15$ km. These observed events do not seem to show considerable deviations from GR, which would be expected if the fundamental scale at which corrections to GR arise was ≈ 40 km. Placing constraints using the ringdown part of the signal for events with lower masses is not doable given the current detectors' sensitivity on that higher frequency regime and inferred binary BH distribution.

Causality constraints

There are theoretical arguments regarding causality that can be used to put constraints on the value of Λ. Most of these come as positivity bounds, which are constraints on the signs of the couplings in the effective action (2.55). Such constraints can be derived from different theoretical considerations. Under requirements of UV completions of the EFT to respect unitarity, causality, Lorentz invariance, and causality, through analyticity arguments on the scattering amplitudes of gravitons [27, 28] constrain c_1 and c_2 in (2.55)

Operator	**Inspiral**	**Ringdown**	**Causality**
Dimension-6	-	$\Lambda^{-1} \lesssim 38.2$ km [170], $\Lambda^{-1} \lesssim 35$ km [55]	$b_1 > 0$
Dimension-8	$\Lambda^{-1} \lesssim 150$ km	$\Lambda^{-1} \lesssim 51.3$ km [170], $\Lambda^{-1} \lesssim 42$ km [55]	$c_1, c_2 > 0$, $\Lambda^{-1} \lesssim 4$ km

Table 2.1: Summary on constraints of Λ^{-1} and its sign, derived from GW data from the inspiral and the ringdown portions of the signal, as well constraints drawn from causality arguments.

to be positive. Demanding that the group velocity of GW's to not be superluminal, these coefficients were also constrained [105] to be positive. More recently, these constraints were refined in [72] to $c_1 > 0$ and $(\Lambda M)^{-6} \lesssim 0.04$ by studying the scattering of GWs in a spherically symmetric BH (of mass M) background (2.57). The causality requirements on this work demand that the contribution of the EFT modifications to the time delay to be positive, schematically for

$$T(\omega) = T^{GR}(\omega) + \delta T(\omega), \tag{2.70}$$

where T is the total time delay, $T^{GR}(\omega)$ is the time delay for the GR case, $\delta T(\omega)$ is the contribution from the EFT modification to the time delay, and ω is the frequency of the scattered wave. In addition to demanding $\delta T(\omega) > 0$, notions of *infrared causality* [70, 60] were also used in the requirements for preserving causality. In short, the EFT's contribution to the time advance should be resolvable within the valid EFT regime. This is, $-\delta T(\omega) \gtrsim 1/\omega$ to be considered acausal, where a bound on ω is also set by requiring that the scattering process should remain in the EFT's regime of validity.

Considering that the theory should remain causal in the description of physical phenomena, and considering that we have observed BHs of conservatively $M \approx 5M_\odot$ [7]. The bound $(\Lambda M)^{-6} < 0.04$ would then imply that $\Lambda^{-1} \lesssim 4.3$ km.

Table 2.3.2 summarizes the constraints discussed in this section on the lengthscale Λ^{-1} at which modifications to GR are incorporated through dimension-six and dimension-eight operators.

As we have just reviewed, the current constraints are in the order of $\Lambda \approx \text{km}^{-1}$. However, one might wonder how modifications at these length scales have not been ruled out by experiments that probed GR in way shorter length scales. Effects from these types of

---

[7] There is some evidence [178, 4, 125] for candidate BHs in the $M \approx 3M_\odot$ range, putting the constraint at $\Lambda^{-1} \lesssim 2.6$ km

operators should be measurable at energies of $E \approx 10^{-2} eV(\Lambda/km^{-1})^{4/5}$ in the lab. The key difference between the experiments that can probe gravity at such length scales/energies and those of GWs is that in the latter the curvature is large. The assumption is then that the UV completion of these theories is such that if the curvature is sufficiently small then the modifications to GR are also small at length scales shorter than Λ^{-1}.

To end this section, it is important to remark that none of these studies has been able to draw constraints using the full inspiral, merger, and ringdown waveform. This is mainly because such waveforms are not available for this type of higher derivative EFT theory. The goal of the works in this thesis is to push forward in enabling the nonlinear studies necessary to generate these waveforms. The availability of full waveforms could not only help to improve constraints on relevant parameters like Λ^{-1} through direct use of these waveforms in data analysis studies. These waveforms could also be used to understand where and in what fashion possible deviations arise in GW waveforms from higher derivative theories. This would help in the construction of phenomenological models used in tests of violations of GR. Furthermore, such waveforms can be used to identify the limitations of solutions obtained in the linear regime, for example, to attest whether a given order in a PN expansion captures all the relevant effects. Additionally, the QNMs extracted from the ringdown portion of such waveforms can fill holes in the parameter space due to the lack of rapidly rotating BH[8] solutions in these theories.

---

[8] Rapidly rotating solutions can be obtained as the end state of BH binary merger simulations.

Chapter 3

Dealing with Pathologies: Fixing the Equations and Order Reduction

3.1 Fixing the equations

In the previous chapter, we have alluded to the importance of defining a well-posed initial value problem if we intend to obtain reliable predictions from a theory. For the theories discussed in section 2.3, achieving a formulation with such properties becomes exceptionally challenging. In general, gravitational theories formulated from effective Lagrangians, including high-order terms in curvature operators, tend to possess field equations involving higher derivatives of the metric (for example, equation (2.56)), which are in general of unknown mathematical type. Nonlinearities in derivatives are also of common appearance in such theories, and in addition to higher-order derivatives, can result in a handful of pathologies that can make their initial value problem ill-posed; among them, the appearance of ghost degrees of freedom due to higher-order time derivatives, loss of uniqueness, and dynamical change of character of the equations, for example, from hyperbolic to elliptic, (see [74, 153, 161, 29, 151, 86, 95]). Furthermore, some of those pathologies materialize as an uncontrolled growth of high-frequency modes, rendering any perturbative expansion in derivatives outside its applicability regime. It is important to note that the standard mathematical approach to analyze PDEs [1] –where the high-frequency limit is examined– creates tension with EFT. Such a regime is incompatible with the very assumptions of the EFT to build extensions to GR. Different techniques can be applied to deal with these issues at the linear regime, and as we have seen in section 2.3.1, predictions are readily available. However, these issues pose significant roadblocks in obtaining predictions in the nonlinear regime, where numerical simulations are necessary and techniques used at the linearized level are not applicable. In such circumstances, the need for a practical approach to deal with these shortcomings becomes of maximum importance. In this section, we will introduce the alternatives proposed to deal with these issues: The *Perturbative Order Reduction* and the *Fixing the Equations* techniques.

The *Perturbative Order Reduction* technique deals with higher derivatives and problematic terms by effectively transforming them into sources. These sources are computed by evaluating such terms on the solutions of the "unmodified" equations. Schematically the procedure can be summarized as follows, starting from the full equations,

$$G(g) = \epsilon M(g), \tag{3.1}$$

where $G(g)$ are the unmodified part of the equations (for example, the Einstein tensor), and $\epsilon M(g)$ contains the modifications to the theory, which might include higher-derivatives and problematic nonlinearities on the lower-order derivatives. By solving the unmodified equations $G(g_0) = 0$ (for example, solving for the metric in the evolution of binary BHs merging), the solution g_0 is obtained. Then this solution can be used to evaluate the modifying terms to define a source $S(g_0) = \epsilon M(g_0)$, and then solve,

$$G(g_1) = S(g_0), \tag{3.2}$$

where now solving for g_1 is equivalent to solving the original problem with the presence of a source $S(g_0)$. In principle, such a procedure can be iterated until the solution reaches some convergence threshold. In practice, such iterations could become increasingly costly; furthermore, if the assumption is that the theory and equations are valid to order ϵ, then the g_1 solution should also be valid to that order, and further iterations would be unnecessary. This has been the approach several works took in performing the evolution of BH binary mergers for higher derivative theories like dCS [149, 151, 150], massive dCS [160], and Hordenski-type theories like EsGB [184, 171] and EdGB [148]. It is relevant to mention that in the cases where corrections to the GW emission were computed, this was done by solving linearized perturbations of the metric in the background described by the uncorrected solution g_0 [1]. Schematically, this would be equivalent to solving,

$$G^0(h_1) = \epsilon S(g_0), \tag{3.3}$$

where h_1 is the perturbation, and G^0 is the linearized operator around the g_0 background. Since the equations being solved are linear, solving for one value of ϵ is enough to know

---

[1] In these works, corrections to the metric enter at order ϵ^2. These corrections are proportional to $\epsilon\phi$, where ϕ is the extra scalar field present in these theories, and ϕ is of order ϵ.

the result for any value of ϵ. This approach does not come without shortcomings. The existence of secular growth in the amplitude of the GW corrections is quite apparent in their results. Such growth gets aggravated the earlier in the inspiral the corrections are turned on. There is also the problem of the lack of back-reaction in the orbit of the BHs; due to corrections, the system is expected to radiate at a different rate than the unmodified theory, hence tightening the orbit at a faster/slower rate. This approach can not capture this. These issues are consequences of the linear nature of this approach, which is ultimately not self-consistent. Given this, the corrections to the GW should not be trusted unless a method is devised which can account for and correct the secular growth, see [94] for such a proposal using a renormalization-group-based approach.

The *Fixing the Equations* approach was proposed in [56] as an alternative to the methods presented above. This approach introduces a suitable modification to an original truncated theory in favor of a fixed theory, where the mathematical pathologies have been dealt with, and nonlinear studies are possible. A guiding principle of this methodology is that physical phenomena should be unmodified at the scales the truncated theory is deemed valid. This is achieved by effectively controlling and dampening the spurious high frequencies that would otherwise be sourced and grow uncontrollably. The failure to control a strong energy flow into smaller scales would take the relevant system away from the validity regime of any truncated expansion in derivatives. The inspiration of [56] to treat ill-posedness in modified gravity theories comes from Israel-Stewart's formulation of relativistic viscous hydrodynamics [122, 120, 121]. The usual formulation for studying relativistic fluids relies on a gradient expansion on the fluid variables up to second order, i.e., a truncated theory. This approach has pathologies when dissipation is included in the model; well-posedness is lost, acausal propagation takes place, the system undergoes a runaway energy transfer to shorter wavelengths, and the theory leaves the regime of applicability since higher-order gradients are relevant. In essence, Israel-Stewart's solution to this issue consists of restoring hyperbolicity by promoting all the contributions (let's call them M) to the equations that do not correspond to the perfect fluid and contain the problematic nonlinearities, to new dynamical variables. These new variables are evolved with ad-hoc evolution equations that guarantee their values asymptote the value of M. The timescale at which the new variables are dampened to M is controlled by a parameter that sets a scale, let's call it τ. This parameter also determines the wavelengths at which the new formulation strongly dissipates energy. This dissipation prevents the system from having significant energy runaways to high-frequency modes, forcing the nonlinear terms to remain subleading. The system is kept in the long-wavelength regime, where the gradient expansion is valid; this is both an assumption and a consequence. It is important to remark that this procedure is consistent with the desired physics only if the system of consideration possesses the feature that energy does not preferably flow to higher frequencies. This happens to be the case for viscous relativistic hydrodynamics in 2+1 dimensions. In such case, a semi-conserved quantity called *enstrophy* [130] guarantees a preferential flow of energy to lower frequency modes. Then for the 2+1 case, the Israel-Stewart formulation is valid to provide solutions that truly represent the physical scenario of interest and that capture features of the underlying non-truncated theory.

Schematically, [56] proposes the following methodology. Starting from (3.1), $M(g)$ are promoted to new dynamical variables Π and are given evolution equations as follows,

$$\begin{aligned} G(g) &= \epsilon\Pi, & (3.4)\\ \sigma\mathcal{S}(\Pi) + \tau\partial_t\Pi &= -(\Pi - M(g)), & (3.5)\end{aligned}$$

where σ and τ are the fixing parameters and are related to the damping scales of the system. Here $\mathcal{S}(\Pi)$ represents some operators, which could be, for example, differential operators, which could or not be necessary to guarantee a controlled evolution of the system. In the absence of $\mathcal{S}(\Pi)$, it is clear that deviations of Π away from $M(g)$ are dampened at a timescale set by τ. As remarked earlier, the success of an approach like this depends on the assurance that the long wavelength properties of the system remain unaltered. Studying the dependence of the solution to variations in the values of τ and σ, and the choice of $\mathcal{S}(\Pi)$, can serve to attest whether physics is being spoiled in the process. There should be a range in the parameter space of fixing parameters, likely where the timescales set by such parameters are smaller or comparable to the lengthscales modifying the theory, where the solutions should be independent or very weakly dependent on the value of such parameters. The failure to achieve such independence would indicate that the system is naturally sourcing higher frequencies and that the approach is dissipating them at different rates, altering relevant physical phenomena in the process. This would be the case in some gravitational scenarios; in critical gravitational collapse, shorter and shorter wavelengths arise as the collapsing fields get arbitrarily focused, and gradients become extremely large. In such conditions, an approach like *Fixing the Equations* would not be able to describe the relevant physics accurately; in such scenarios, any effective description relying on a truncated expansion in derivatives would be inapplicable. However, it is not far-fetched to believe that scenarios like BH binary mergers could be scenarios where these techniques would be applicable. Simulations on GR do not show a significant transfer of energy to higher frequencies, not even in the highly nonlinear regime of the merger itself. Furthermore, GW events do not show signs of strong energy cascades into the UV, which suggests that the underlying gravity theory governing such events disfavors such processes.

Some implementations of the *Fixing the Equations* method were studied in [56]. In particular, they studied such implementation at the linearized level on equations with common pathologies to the ones encountered in modified gravity theories. We review a slightly modified version of one of these examples in Appendix A. In particular, [56] shows how this technique successfully removes blowing-up modes in the original equations while preserving the physics at the long wavelength regime. A follow-up work [16] further studied the numerical implementation of this technique in the context of a particular EFT [46] that stood as a truncation of a know UV complete theory. In particular, [16] studied the effectiveness of mimicking the solutions of the UV theory by the implementation of the *Perturbative Order Reduction* and *Fixing* on the pathological truncated theory, task for which the latter method showed more concrete results.

Chapter 4 of this thesis is based on our work applying the *Fixing the Equations* for the first time in a theory of modified gravity and performing simulations of highly dynamical scenarios in spherical symmetry. Chapter 5 is based on the work extending the work discussed in Chapter 4 to simulations of the dimension-eight EFT of gravity for BH binary mergers.

3.2 Order reduction

When the equations of motion of a theory are higher than second-order time derivatives, it is almost universal that its Hamiltonian is unbounded from below. This leads to an instability and, nonphysical solutions, known as the *Ostrogradski instability*[152]. In the context of particle physics, this is not an unusual scenario when considering EFTs, where higher-order derivatives are common. A completely healthy UV complete theory does not imply that its corresponding EFT will be free of these instabilities [46]. Furthermore, the extra degrees of freedom that come from the higher derivatives and cause the instabilities (ghosts) are usually unphysical from the EFT perspective. This is the case if the mass of such fields is above or around the energy cut-off of the EFT. These are good arguments against discarding EFTs with such pathologies and, instead, attempting to find a way to extract physical and well-behaved solutions from them. In [173], similar arguments are presented to defend the idea that it is not necessary to restrict to second order in time theories of the Lovelock[138] and Horndeski[118] type as proposals for modified gravity. In particular, [173] demonstrates how higher-derivative operators can be cast into a lower-derivative form by applying EFT techniques. A simple and illustrative example of how to use one of these techniques is presented in [173]. This example is instructive enough to be repeated in the thesis in appendix B. In particular, example B shows how sometimes the space of solutions of a higher order theory is larger than expected, requiring then extra initial conditions which can be associated with solutions that do not represent solutions of the UV complete theory. The example also presents the implementation of a technique called *Order reduction* (not to confuse with the *Perturbative Order Reduction* discussed in the previous section) that helps to recast the problem into second order in derivatives. In this thesis, we will use an order reduction technique to deal with higher-than-second derivatives in the equations. This technique is applied in conjunction with the *Fixing the Equations* approach in Chapters 4 and 5, and on its own as done in Chapter 6.

Chapter 4

Single black hole nonlinear dynamics in Effective Field Theory extension to GR

4.1 Introduction

In the introduction, we discussed how extracting predictions in the nonlinear regime faces multiple formal and practical challenges for most candidate alternatives to GR. On the formal side, there is uncertainty on whether different theories can define a well-defined initial value problem in the regimes of interest (nonlinear, strongly gravitating, and possibly highly dynamical). At the practical level, the desire to discern possible signatures with complex theories requires involved (and typically costly) numerical simulations, a problem that is exacerbated—and in many cases rendered formally impossible— due to the mathematical challenge alluded to above. In section 3.1, the *Fixing the Equations* was introduced as a possible methodology to deal with the aforementioned difficulties. The benefits of this approach have been demonstrated in a few simplified model problems [56, 16] and we now explore its application within the context of a challenging extension to GR inspired by EFT considerations [84], which also explicitly unearths several delicate issues. In this chapter, adopting spherical symmetry for simplicity, we illustrate the application of the method and address a number of required steps. In particular, we discuss the construction of initial data consistent with the theory (and in passing also contrast with the *Perturbative Order Reduction* approach), the evolution of the system, and the impact of modifications to GR.

This chapter is organized as follows. In section 4.2, following [84], we briefly discuss the theory adopted considering, in our case, also a minimally coupled self-gravitating scalar field in the theory. We also present the steps involved in considering equations of motions governed by *second order* in time derivatives (but general spatial derivatives). Section4.4 describes the construction of initial data, deferring to section 4.6 the results obtained and potential implications in section 4.7. We include in the appendices C convergence results. Lastly, we employ geometrized units ($G = c = 1$), use early Latin letters in the alphabet to denote spacetime indices and use the latter part of the Latin alphabet for spatial indices.

4.2 Model

4.2.1 EFT and field equations

To fix ideas and adopt a sufficiently challenging model, we here take an extension to GR constructed from an EFT point of view. In such an approach, one introduces no new degrees of freedom in the theory—as they are integrated out—and parameterizes new physics through a suitable low-energy/long-distance expansion. New physics enters through local interactions organized in terms of powers that depend on some given scale [47]. Here, we consider the extension presented in [84], which we defined in section 2.3 as the dimension-eight operator theory. In this work, we include a minimally coupled scalar field to endow the target system (as we consider spherical symmetry) with non-trivial dynamics [1]. We note that [84] builds the action for the EFT, requiring that the theory respects unitarity, causality, and locality and includes no new light degrees of freedom. These requirements are consistent with writing the most general Lagrangian by adding to the Einstein Hilbert action's terms constructed out of the Riemann tensor and suppressing them by a curvature scale comparable to the scale probed by gravitational wave observations. The action for this EFT reads,

$$S_{eff} = \frac{1}{16\pi G} \int d^4x \sqrt{-g} \left(R - \frac{\mathcal{C}^2}{\Lambda^6} - \frac{\widetilde{\mathcal{C}}^2}{\widetilde{\Lambda}^6} - \frac{\mathcal{C}\widetilde{\mathcal{C}}}{\Lambda_-^6} + \dots \right), \tag{4.1}$$

where $\mathcal{C} \equiv R_{abcd}R^{abcd}$ and $\widetilde{\mathcal{C}} \equiv R_{abcd}\widetilde{R}^{abcd}$, with $\widetilde{R}^{abef} = \epsilon^{ab}{}_{cd}R^{cdef}$, and the $+\dots$ correspond to sub-leading contributions.

Notice, however, that the EFT built this way starts with correction at Λ^{-6} as it is restricted to the vacuum. More generally, in principle, other orders could be present

---

[1] As argued in 2.3 in the non-vacuum case, interactions would give rise to corrections at Λ^{-2}.

depending on assumptions made. For concreteness, however, we here stick to the model in [84] so as to work in a highly demanding (i.e., with respect to the order of derivatives to deal with) setting to stress our approach. To simplify somewhat the computational cost, we will also restrict to the case $\widetilde{\Lambda}^{-6} = \Lambda_{-}^{-6} = 0$.

We thus consider the action above and include a minimally coupled scalar field to obtain non-trivial dynamics. The equations of motion are,

$$\begin{aligned} G_{ab} = 8\pi T_{ab} + \frac{1}{\Lambda^6}\Big(&- 8\mathcal{C} R_a{}^c R_{bc} + 8\,\mathcal{C}\, R^{cd} R_{acbd} + 4\,\mathcal{C}\, R_a{}^{cde} R_{bcde} - \frac{1}{2} g_{ab}\mathcal{C}^2 - 4\mathcal{C}\nabla_a\nabla_b R \\ &- 32 R^{defg}\nabla_{(a} R_{b)}{}^c \nabla_c R_{defg} + 8\mathcal{C}\nabla_c\nabla^c R_{ab} + 32 R^{defg}\nabla_c R_{defg}\nabla^c R_{ab} + 8 R_a{}^c{}_b{}^d \nabla_d\nabla_c\mathcal{C}\Big), \end{aligned} \tag{4.2}$$

$$\nabla^a T_{ab} = 0. \tag{4.3}$$

with G_{ab} the Einstein tensor and T_{ab} the standard scalar field stress-energy tensor with no potential. Besides the presence of T_{ab}, the main difference between the field equations (4.2) with those in [84] is the appearance of terms with involving R_{ab} and R, which vanish in their case. Modifications to GR in this theory are governed by involved higher-derivative/nonlinear terms on the right-hand side of Einstein's field equations. Demonstrating that our proposed method is capable of handling these equations is a central goal of this work.

4.2.2 3+1 splitting

We now discuss how we express our equations in a way amenable to numerical integration. To this end, we must face three particular issues: (i) define a 3+1 initial value problem by a suitable spacetime decomposition, (ii) address the problem of higher than second-time derivatives in the resulting equations, (iii) address the related problem of higher-order spatial derivatives and the issue of well-posedness.

To start, we adopt the standard spacetime decomposition of spacetime in 3+1 form by introducing a spacelike foliation, with intrinsic metric γ_{ij}, extrinsic curvature K_{ij}, and auxiliary lapse/shift variables $\{\alpha, \beta^i\}$. Further, we adopt the (symmetric hyperbolic formulation, in the absence of corrections) "*Generalized Harmonic*" (GH) formulation of GR[91, 157, 135]. The full set of equations can be expressed as:

$$G_{ab} = 8\pi T_{ab} + \epsilon M_{ab}, \tag{4.4}$$

where we have also replaced Λ^{-6} for ϵ.

Then the full system can be written as,

$$\partial_\perp \gamma_{ij} = -\, 2\alpha K_{ij}, \tag{4.5a}$$

$$\begin{aligned}\partial_\perp K_{ij} =& \alpha \left[R^{(3)}_{ij} - 2K_{ik}K^k_j - \widetilde{\pi} K_{ij} \right] - D_i D_j \alpha - \alpha D_{(i}\mathcal{C}_{j)} - \kappa\alpha\gamma_{ij}\mathcal{C}_T/2 \\ & - 8\pi G\alpha \left[S_{ij} - \gamma_{ij}(S-\rho)/2 \right] - \epsilon\alpha \left[S^M_{ij} - \gamma_{ij}(S^M - \rho^M)/2 \right],\end{aligned} \tag{4.5b}$$

$$\partial_\perp \alpha = \alpha^2 \widetilde{\pi} - \alpha^2 H_T, \tag{4.5c}$$

$$\partial_t \beta^i = \beta^j \bar{D}_j \beta^i + \alpha^2 \rho^i - \alpha D^i \alpha + \alpha^2 H^i, \tag{4.5d}$$

$$\partial_\perp \widetilde{\pi} = -\, \alpha K_{ij}K^{ij} + D_i D^i \alpha + \mathcal{C}^i D_i \alpha - \kappa\alpha\mathcal{C}_T/2 - 4\pi G\alpha(\rho + S) - \frac{\epsilon}{2}\alpha(\rho^M + S^M), \tag{4.5e}$$

$$\begin{aligned}\partial_\perp \rho^i =& \gamma^{k\ell}\bar{D}_k \bar{D}_\ell \beta^i + \alpha D^i \widetilde{\pi} - \widetilde{\pi} D^i \alpha - 2K^{ij} D_j \alpha + 2\alpha K^{jk}\Delta\Gamma^i_{jk} + \kappa\alpha\mathcal{C}^i \\ & - 16\pi G\alpha j^i - 2\epsilon\alpha j^i_M,\end{aligned} \tag{4.5f}$$

$$\nabla^a T_{ba} = 0, \tag{4.5g}$$

with the constraints,

$$\mathcal{C}_T \equiv \widetilde{\pi} + K, \tag{4.6a}$$

$$\mathcal{C}^i \equiv -\rho^i + \Delta\Gamma^i_{jk}\gamma^{jk}, \tag{4.6b}$$

$$\mathcal{H} \equiv K^2 - K_{ij}K^{ij} + R - 16\pi G\rho - 2\epsilon\rho^M, \tag{4.6c}$$

$$\mathcal{M}_i \equiv D_j K_i^{\ j} - D_i K - 8\pi G j_i - \epsilon j^M_i, \tag{4.6d}$$

where $K \equiv \gamma^{ij}K_{ij}$, D_i and $\bar{D}_i$ are the covariant derivatives for the three-metric γ_{ij} and the background 3-metric $\bar{\gamma}_{ij}$ respectively. The derivative operator $\partial_\perp$ is defined as $\partial_\perp = \partial_t - \mathcal{L}_\beta$, where $\mathcal{L}_\beta$ is the Lie derivative along the shift vector β^i. We define $\Delta\Gamma^i_{jk} :=^{(3)} \Gamma^i_{jk} -^{(3)} \bar{\Gamma}^i{}_{jk}$, where these are the Christoffel symbols for the induced metric and background metric (flat in spherical coordinates) respectively. We also define $H_T := H^a n_a$, where n_a is the normal vector to the spatial hypersurfaces defined by the spacetime foliation (note, for completeness sake we include the gauge source vector H_a for reference but in our studies it was sufficient to adopt $H_a = 0$). We also introduce new dynamical variables $\widetilde{\pi}$ and ρ^i through equations (4.5c-4.5d) to make the system (ignoring the extensions to gravity) first order in time derivatives. S_{ij}, S, ρ and j^i are the matter variables constructed from the Energy-Momentum tensor T_{ab} as, $S_{ij} = P^a_i P^b_j T_{ab}$, its trace $S = \gamma^{ij}S_{ij}$, $\rho = n_a n_b T^{ab}$, and $j^i = -P^{ia} n^b T_{ab}$. Here the definitions for S^M_{ij} ,S^M, ρ^M and j^i_M are analogous to the ones for the matter sources, but instead of using T_{ab}, we use M_{ab}. In addition, we now have also included now equation (4.5g) that determines the evolution for the matter degrees of freedom.

Let us now analyze the nature of the additional terms M_{ab} we have incorporated into Einstein's equations. All these terms contain nonlinear combinations of derivatives of metric components with a combined scaling of λ^{-8} (with λ the local wavelength). In particular, terms contain derivatives of order as high as fourth. Thus, such terms are present for the effective sources S^M_{ij}, S^M, ρ^M and j^M_i(4.5). Well-posedness has now clearly gone out the window. Both the presence of high-order time derivatives—which bring forth so-called Ostrogradsky's instability[152]— as well as higher order spatial derivatives (of both even and odd orders) doom prospects of defining well-posed problems for general cases. However, restriction of the initial data considered and control of potential pathologies introduced might enable obtaining well-posedness. In what follows, we describe how these issues are addressed.

4.2.3 Time derivative order reduction of the modified equations

We now turn our attention now to dealing with higher-than-second-order time derivatives. To do so, we follow an order reduction approach (e.g. [173]) whereby higher time derivatives are expressed in terms of spatial derivatives by repeated use of the field equations.

For presentation clarity, we illustrate this approach schematically and ignore contributions from the matter terms. First we rewrite system (4.5) in terms of variables $g^a = \{\gamma_{ij}, \alpha, \beta\}$ by means of equations (4.5a),(4.5c), and (4.5d). Then equations (4.5b), (4.5e) and (4.5f) can be cast as,

$$\frac{\partial^2 g^a}{\partial t^2} = \Delta^a(g, \partial_b g, \partial_i^2 g) + \epsilon M^a(g, \partial_b g, \partial_b^2 g, \partial_b^3 g, \partial_b^4 g) + \mathcal{O}(\epsilon^2), \tag{4.7}$$

where Δ^a represents the contributions of GR that, as $(g, \partial_b g, \partial_i^2 g)$ indicates, depend only on the variables g^a, their first spacetime derivatives, and their second spatial derivatives. The symbol M^a encodes the contributions of extensions to GR's equations which depend on the variables g^a, their first, second, third and fourth spacetime derivatives. Now, take equations (4.7) to $\mathcal{O}(\epsilon)$,

$$\frac{\partial^2 g^a}{\partial t^2} = \Delta^a(g, \partial_b g, \partial_i^2 g) + \mathcal{O}(\epsilon), \tag{4.8}$$

and define higher time derivatives of the g^a variables by suitable derivatives of (4.8). For instance, the third time derivative would be given to this order by,

$$\frac{\partial^3 g^a}{\partial t^3} = \frac{\partial_t \Delta^a}{\partial t}(g, \partial_b g, \partial_b^2 g, \partial_b \partial_i^2 g) + \mathcal{O}(\epsilon). \tag{4.9}$$

Notice the right-hand side of (4.9) depends on second-time derivatives of the g^a variables, which can be re-expressed through (4.8). This procedure can be repeated to express all higher than second-order time derivatives appearing on the right-hand-side in terms of spatial derivatives (of high order) while keeping time derivatives to at most first order.

Armed with these definitions, and replacing in $M_{ab} \to \widetilde{M}_{ab}$, one has

$$\widetilde{M}_{ab} = M_{ab} + \mathcal{O}(\epsilon), \tag{4.10}$$

and can re-express the M^a terms in equations (4.7) to yield the "time reduced" evolution equations which are unchanged to $\mathcal{O}(\epsilon)$,

$$\frac{\partial^2 g^a}{\partial t^2} = \Delta^a(g, \partial_b g, \partial_i^2 g) + \epsilon \widetilde{M}^a(g, \partial_b g, \partial_b \partial_i g, \partial_b \partial_i^2 g, \partial_b \partial_i^3 g) + \mathcal{O}(\epsilon^2), \tag{4.11}$$

Finally, we reintroduce variables $u^a = \{K_{ij}, \widetilde{\pi}, \rho^i\}$ (through (4.5a),(4.5c), and (4.5d)) to present the system in first order in time form for the whole set of variables $v^a = \{g^a, u^a\}$,

$$\frac{\partial u^a}{\partial t} = \Delta^a(v, \partial_i v, \partial_i^2 g) + \epsilon \widetilde{M}^a(v, \partial_i v, \partial_i^2 v, \partial_i^3 v, \partial_i^4 g) + \mathcal{O}(\epsilon^2). \tag{4.12}$$

Equations (4.5) and (4.6) are modified solely by replacing S_{ij}^M, S^M, ρ^M and j_M^i by $S_{ij}^{\widetilde{M}}$, $S^{\widetilde{M}}$, $\rho^{\widetilde{M}}$ and $j_{\widetilde{M}}^i$, constructed using the tensor $\widetilde{M}_{\mu\nu}$ instead of the tensor $M_{\mu\nu}$. The only time derivatives are on the left-hand side of the equations, while the right-hand side has up to third-order spatial derivatives for the $\{u^a\}$ variables, and up to fourth order spatial derivatives for the $\{g^a\}$ variables. Later on, we will use a similar strategy to deal with the constraint equations when constructing consistent initial data.

Before moving on, we note that in the case of spherical symmetry, there is yet another step we can take. One can make use of the constraint equations (and their spatial derivatives) (4.6c) and (4.6d) to replace high-order spatial derivatives of metric variables in $M_{\mu\nu}$ in terms of (higher) derivatives of the scalar field. For convenience, we do so here, and, as a result, our equations of motion will not display derivatives of higher than second order in the metric. Instead, there will be non-linear combinations of derivatives up to order two in the metric and higher derivatives of the scalar field.

4.2.4 Fixing the equation

Having removed all higher order time derivatives, we are not done, as even without potential Ostrogradsky instabilities, there is a long road ahead to ensure the well-posedness of an initial value problem. The existence of higher order derivatives (in this case of the scalar field), and nonlinear terms describing products of up to second-order spatial derivatives (of the metric variables) are responsible for a variety of problems preventing the definition of a well-posed problem (at the analytical and, therefore, numerical levels). For instance, in [56], several examples of simple toy models illustrate the problematic behavior that higher derivatives can bring. Clearly, a suitable approach must be devised even to aspire to explore the theory of interest. As mentioned, at present two options are being explored to address this issue: (i) "*Reduction of order*" procedure[2] and (ii) "*Fixing the Equations*". In this work, we choose the latter approach. We will devote this section to giving details on the implementation of this technique. Further details and motivations for this approach can be found in [56, 16]. At its core, such an approach introduces an evolution prescription to the higher-order terms to ensure high-frequency modes are controlled.

To this end, we introduce a new dynamical tensor Π_{ab} with an evolution prescription to dynamically constrain it to $\widetilde{M}_{ab}$ (and with initial data $\Pi_{ab} = \widetilde{M}_{ab}$). We write system (4.12) (omitting the $\mathcal{O}(\epsilon^2)$ symbol) as,

$$\frac{\partial u^a}{\partial t} = \widetilde{\Delta}^a(v, \partial_i v, \partial_i^2 g) + \epsilon \Pi^a, \tag{4.13}$$

$$\tau \frac{\partial \Pi_{ab}}{\partial t} = -(\Pi_{ab} - \widetilde{M}_{ab}(v, \partial_i v, \partial_i^2 v, \partial_i^3 v, \partial_i^4 g)), \tag{4.14}$$

where now Π^a is computed using the tensor Π_{ab} instead of the tensor $\widetilde{M}_{ab}$. Equations (4.14) are ad-hoc equations introduced to control Π_{ab} to approach $\widetilde{M}_{ab}$ in a timescale given by the free parameter τ. (Note, τ has dimensions of time; throughout this work, specific values will be given to it with respect to the total mass M of scenarios considered.) The particular form of equation (4.14) is not unique though it should not be crucial as long as the solution remains well-behaved and within the domain of applicability of the EFT. In such a scenario, the physics obtained would be independent of the choice of equation and the value of the damping timescale τ. This approach controls the behavior of short wavelength modes in the original equations while preserving the physics at the long wavelength regime.

We thus arrive at the final form of the equations that are now ready for numerical implementation. Notice that in equations (4.5) and (4.6) one replaces S^M_{ij},S^M, ρ^M and j^i_M by S^{Π}_{ij},S^{Π}, ρ^{Π} and j^i_{Π}, which are constructed with $\Pi_{\mu\nu}$ instead M_{ab}. Additionally, one incorporates equations (4.14) for the evolution of the new dynamical variables $\Pi_{\mu\nu}$.

---

[2] While related, this is not to be mistaken with the time reduction of order used in the previous section.

4.3 Target problem

We study a simple case that is dynamic and in which non-linearities become relevant. To this end, we consider the dynamics of a spherically symmetric spacetime minimally coupled to a scalar field that induces non-trivial dynamics in the problem. The line element for our problem is,

$$ds^2 = (-\alpha^2 + g_{rr}\beta^2)dt^2 + 2\beta g_{rr} dr dt + g_{rr} dr^2 + r^2 g_T (d\theta^2 + \sin^2\theta d\varphi^2). \tag{4.15}$$

In these coordinates the general form of the tensor $\widetilde{M}_{\mu\nu}$ encoding the extension to GR takes the form,

$$\widetilde{M}_{ab} = \begin{pmatrix} \widetilde{M}_{tt} & \widetilde{M}_{tr} & 0 & 0 \\ \widetilde{M}_{tr} & \widetilde{M}_{rr} & 0 & 0 \\ 0 & 0 & \widetilde{M}_T & 0 \\ 0 & 0 & 0 & \widetilde{M}_T \sin^2\theta \end{pmatrix}, \tag{4.16}$$

with four independent components. The structure $\Pi_{\mu\nu}$ is also of the form of (4.16).

The equation of motion for the massless scalar field (4.3) is,

$$\nabla^a \nabla_a \phi = 0, \tag{4.17}$$

and we introduce the new variable Σ defined by,

$$\Sigma := \frac{1}{\alpha}(\beta\partial_r\phi - \partial_t\phi), \tag{4.18}$$

to also express the scalar field evolution equations in terms of first order in time derivatives.

4.4 Initial Data & implementation

We next discuss how to construct initial data that is consistent with the modified theory we are working with. The procedure is similar to the one usually followed in GR, but there are certain unique aspects to be treated carefully.

We start with the usual conformal decomposition of the spatial metric,

$$\gamma_{ij} = \psi^4 \overline{\gamma}_{ij}, \tag{4.19}$$

where ψ is the conformal factor and $\overline{\gamma}_{ij}$ is a given background metric which we take to be the flat metric in spherical coordinates. With this choice, the extension to the *Hamiltonian Constraint* takes the form,

$$8\nabla^2_{\mathit{flat}}\psi + \psi^5(A_{ij}A^{ij} - \frac{2}{3}K^2) + 16\pi\psi^5\rho + 2\epsilon\psi^5\rho^{\widetilde{M}} = 0, \tag{4.20}$$

where A_{ij} is the traceless part of the extrinsic curvature tensor K_{ij} and now the additional term $2\psi^5\rho^{\widetilde{M}}$ contains the modifications to GR. Notice that the effective energy density defined by extension to GR is now directly constructed using the time reduced tensor $\widetilde{M}_{\mu\nu}$.

The extension to the *Momentum Constraint* takes the form,

$$\nabla_j A^{ij} - \frac{2}{3}\nabla^i K - 8\pi j^i - \epsilon j^i_{\widetilde{M}} = 0, \tag{4.21}$$

which includes the additional current-like term $-\epsilon j^i_{\widetilde{M}}$. We aim to define initial data with traceless extrinsic curvature K_{ij} (i.e. $K = 0$), so we adopt the following ansatz for A_{ij},

$$A_{ij} = \begin{pmatrix} K_{rr} & 0 & 0 \\ 0 & -r^2\frac{K_{rr}}{2} & 0 \\ 0 & 0 & -r^2\frac{K_{rr}\sin^2\theta}{2} \end{pmatrix}. \tag{4.22}$$

The resulting (extended) *Hamiltonian* and *Momentum* constraints are,

$$\frac{\partial^2\psi}{\partial r^2} = -\frac{2}{r}\frac{\partial\psi}{\partial r} - \frac{3}{16}\frac{K_{rr}^2}{\psi^3} - \pi\psi\left(\frac{\partial\phi}{\partial r}\right)^2 - \pi\psi^5\Sigma^2 + \epsilon\frac{\psi^5}{\alpha^2}\left(-\frac{\beta^2}{4}\widetilde{M}_{rr} + \frac{\beta}{2}\widetilde{M}_{tr} - \frac{1}{4}\widetilde{M}_{tt}\right), \tag{4.23}$$

$$\frac{\partial K_{rr}}{\partial r} = -2\psi^{-1}K_{rr}\frac{\partial\psi}{\partial r} - \frac{3}{r}K_{rr} + 8\pi\psi^4\Sigma\frac{\partial\phi}{\partial r} + \epsilon\frac{\psi^4}{\alpha}\left(\beta\widetilde{M}_{rr} - \widetilde{M}_{tr}\right), \tag{4.24}$$

respectively.

For $\epsilon = 0$, these are familiar forms in GR, and given appropriate boundary values, and initial data for the scalar field, a unique solution can be found. Notice, these equations do not depend on the gauge variables $\{\alpha, \beta^i\}$. However, when $\epsilon \neq 0$ the modifications to gravity add terms with high order spatial derivatives, highly nonlinear terms, and even a dependency on the gauge variables. To date, a thorough mathematical analysis for these types of equations in general cases is still lacking. Notice, in particular, the presence of higher derivatives require additional boundary conditions—either explicitly or implicitly given. We have explored two ways of constructing initial data consistent with this system. The first one involves a procedure similar to the one we used for the time order reduction in section 4.2.3—so as to express higher derivatives in terms of lower ones—and a second one which is essentially the iterative approach (i) mentioned in the introduction. For clarity, we will refer to them as *order reduced* and *iterative* methods.

4.4.1 Order-reduced direct integration (ORDI)

In this approach, one replaces high-order spatial derivatives on the tensor $\widetilde{M}_{\mu\nu}$ by means of equations (4.23) and (4.24) to the order desired. Schematically, to first order in ϵ, we can write equations (4.23) and (4.24) as,

$$\frac{\partial^2 \psi}{\partial r^2} = \Psi(\chi, \partial_r \psi) + \epsilon \widetilde{M}_\psi(\chi, \partial_r \chi, \partial_r^2 \chi, \partial_r^3 \chi, \partial_r^4 \psi), \tag{4.25}$$

$$\frac{\partial K_{rr}}{\partial r} = \mathcal{K}(\chi, \partial_r \psi) + \epsilon \widetilde{M}_K(\chi, \partial_r \chi, \partial_r^2 \chi, \partial_r^3 \chi, \partial_r^4 \psi), \tag{4.26}$$

were $\chi = \{\psi, K_{rr}\}$ and we omit (in the presentation) the matter variables since their initial values are chosen freely. By neglecting $\mathcal{O}(\epsilon)$ terms in equations (4.25) and (4.26) then the expressions,

$$\begin{aligned} \frac{\partial^2 \psi}{\partial r^2} &= \Psi(\psi, \partial_r \psi, K_{rr}) + \mathcal{O}(\epsilon), \\ \frac{\partial K_{rr}}{\partial r} &= \mathcal{K}(\psi, \partial_r \psi, K_{rr}) + \mathcal{O}(\epsilon), \end{aligned} \tag{4.27}$$

$$\begin{aligned} \frac{\partial^3 \psi}{\partial r^3} &= \frac{\partial \Psi}{\partial r}(\chi, \partial_r \chi, \partial_r^2 \psi) + \mathcal{O}(\epsilon), \\ \frac{\partial^2 K_{rr}}{\partial r^2} &= \frac{\partial \mathcal{K}}{\partial r}(\chi, \partial_r \chi, \partial_r^2 \psi) + \mathcal{O}(\epsilon), \end{aligned} \tag{4.28}$$

$$\begin{aligned} \frac{\partial^4 \psi}{\partial r^4} &= \frac{\partial^2 \Psi}{\partial r^2}(\chi, \partial_r \chi, \partial_r^2 \chi, \partial_r^3 \psi) + \mathcal{O}(\epsilon), \\ \frac{\partial^3 K_{rr}}{\partial r^3} &= \frac{\partial^2 \mathcal{K}}{\partial r^2}(\chi, \partial_r \chi, \partial_r^2 \chi, \partial_r^3 \psi) + \mathcal{O}(\epsilon), \end{aligned} \tag{4.29}$$

can be used to redefine $\widetilde{M}_\psi$ and $\widetilde{M}_\psi$ in terms of only $\{\psi, \partial_r \psi, K_{rr}\}$, so that,

$$\begin{aligned} \overline{M}_\psi(\psi, \partial_r \psi, K_{rr}) &= \widetilde{M}_\psi(\chi, \partial_r \chi, \partial_r^2 \chi, \partial_r^3 \chi, \partial_r^4 \psi) + \mathcal{O}(\epsilon), \\ \overline{M}_K(\psi, \partial_r \psi, K_{rr}) &= \widetilde{M}_K(\chi, \partial_r \chi, \partial_r^2 \chi, \partial_r^3 \chi, \partial_r^4 \psi) + \mathcal{O}(\epsilon). \end{aligned} \tag{4.30}$$

Finally the system of equations (4.25) and (4.26) can be redefined as,

$$\frac{\partial^2 \psi}{\partial r^2} = \Psi(\psi, \partial_r \psi, K_{rr}) + \epsilon \overline{M}_\psi(\psi, \partial_r \psi, K_{rr}), \tag{4.31}$$

$$\frac{\partial K_{rr}}{\partial r} = \mathcal{K}(\psi, \partial_r\psi, K_{rr}) + \epsilon \overline{M}_K(\psi, \partial_r\psi, K_{rr}), \tag{4.32}$$

which now contains no higher-order derivatives on the right-hand side. Higher order derivatives are replaced by an expansion in ϵ of lower order derivatives, and the equations are now, in principle, solvable. For concreteness, we have restricted to first order in ϵ. For the numerical implementation, we employ finite difference approximations, and we numerically integrate through a Runge-Kutta 4th order. To obtain solutions, we perform a shooting procedure in which the value of the fields on the inner boundary is found by the implementation of a Newton-Rapson method to ensure that the solutions satisfy the outer boundary conditions (4.39) and (4.40).

4.4.2 Iterative method, full system (FSII) or order-reduced (ORII)

The procedure for constructing an iterative solution relies on constructing a solution in terms of an expansion in ϵ where corrections are evaluated with respect to previous iterations. One can choose to solve for the system of equations (4.23) and (4.24)—which involve higher derivatives. We refer to this as the full system and study its iterative (or perturbative) integration (FSII). Alternatively, one can adopt the order-reduced form of the equations (4.31), (4.32) and solve it iteratively (ORII). We describe the order-reduced case (and an analogous method is employed for the FSII case).

First find solutions $\psi_{(0)}$ and $K_{rr(0)}$ for the GR equivalent (4.27). Then with this zeroth order solution all the components of $\widetilde{M}_{\mu\nu}$ can be evaluated to an approximation $\widetilde{M}_{\mu\nu(0)}$. Next one can find solutions $\psi_{(1)}$ and $K_{rr(1)}$ for,

$$\begin{aligned}\frac{\partial^2\psi_{(1)}}{\partial r^2} = & -\frac{2}{r}\frac{\partial\psi_{(1)}}{\partial r} - \frac{3}{16}\frac{K^2_{rr(1)}}{\psi^3_{(1)}} - \pi\psi_{(1)}\left(\frac{\partial\phi}{\partial r}\right)^2 - \pi\psi^5_{(1)}\Sigma^2 \\ & + \epsilon\frac{\psi^5_{(0)}}{\alpha^2}\left(-\frac{\beta^2}{4}\widetilde{M}_{rr(0)} + \frac{\beta}{2}\widetilde{M}_{tr(0)} - \frac{1}{4}\widetilde{M}_{tt(0)}\right),\end{aligned} \tag{4.33}$$

$$\begin{aligned}\frac{\partial K_{rr(1)}}{\partial r} = & -2\psi^{-1}_{(1)}K_{rr(1)}\frac{\partial\psi_{(1)}}{\partial r} - \frac{3}{r}K_{rr(1)} + 8\pi\psi^4_{(1)}\Sigma\frac{\partial\phi}{\partial r} \\ & + \epsilon\frac{\psi^4_{(0)}}{\alpha}\left(\beta\widetilde{M}_{rr(0)} - \widetilde{M}_{tr(0)}\right).\end{aligned} \tag{4.34}$$

This way the terms proportional to ϵ on (4.33) and (4.34) act simply as source terms in the equations. This procedure can of course be iterated to obtain $\psi_{(j)}$ and $K_{rr(j)}$.

4.4.3 Matter source

We adopt a largely in-falling scalar field pulse towards a black hole,

$$\phi(t,r) = \frac{\Phi(u \equiv r+t)}{r}, \tag{4.35}$$

with,

$$\Phi(u) = Au^2 \exp\left(-\frac{(u-r_c)^2}{\sigma^2}\right), \tag{4.36}$$

where A, r_c and σ are the pulse amplitude, center, and width, respectively. Thus, the matter source variables take the following initial values,

$$\phi_0 = Ar \exp\left(-\frac{(r-r_c)^2}{\sigma^2}\right), \tag{4.37}$$

$$\Sigma_0 = \frac{\phi_0}{\alpha}\left(\beta\left(\frac{1}{r} - \frac{2(r-r_c)}{\sigma^2}\right) - \left(\frac{2}{r} - \frac{2(r-r_c)}{\sigma^2}\right)\right). \tag{4.38}$$

and as many spatial derivatives of ϕ_0 as required.

4.4.4 Boundary conditions

To solve the initial data equations boundary conditions must be specified. In principle, given the high (fourth) order in derivatives of the original equations (4.23) and (4.24), then up to second derivatives or third derivatives should also be prescribed at the boundaries. However, we have modified these equations via either the iterative or the order-reduced approaches to eliminate these high-order derivatives. As a result, one is implicitly specifying these derivatives. In particular, in the order-reduced options high order derivatives are expressed in terms of lower order ones as in equations (4.27), (4.28) and (4.29). In the full system iterative integration approach these boundary conditions are redefined at each iteration by means of the previous iteration solution's derivatives.

We explicitly prescribe,

$$\psi|_{r_{out}} = 1 + \frac{M}{2r_{out}}, \tag{4.39}$$

$$\left.\frac{\partial\psi}{\partial r}\right|_{r_{out}} = -\frac{M}{2r_{out}^2}, \tag{4.40}$$

$$K_{rr}|_{r_{in}} = 0 \tag{4.41}$$

Also, for simplicity, we choose the initial values of the gauge variables to be $\alpha(t=0)=1$ and $\beta(t=0)=0$. This choice simplifies (4.23), since $\beta=0$ removes, except the term proportional to $\widetilde{M}_{tt}$, all other modifications to GR. Furthermore, the only non-zero modification term in equation (4.24) is the one proportional to $\widetilde{M}_{tr}$, which vanishes for $K_{rr}=0$. Consequently, since $K_{rr}=0$ on the inner boundary, $K_{rr}(r<R)\simeq 0$ with $r=R$ the radius at which the scalar field source is not trivially small.

4.5 Evolution equations & implementation

Having presented the evolution equations (4.13), (4.14) and (4.17) (reduced to first-order form via (4.18) for convenience) we implement them numerically in the following way. We adopt a method of lines to integrate in time through a Runge-Kutta 4th order which CFL coefficient set as $dt=0.2\,dx$, where dt denotes the time step and dx the spatial (uniform) grid spacing. Our uniform grid extends from $r_i=0.2M$ to $r_i=240M$, and our typical resolution for production runs is $dx=0.019M$. Spatial derivatives are discretized via Finite Differences operators satisfying summation by parts (SBP) (see e.g. [48, 49, 142, 141]), of 6th order for inner points and 3rd order at the boundaries, and we excise the black hole interior. We implement Kreiss-Oliger dissipation with operators that are 5th order at the boundary and 6th order at the interior points [76].

4.6 Results

4.6.1 Initial data

We now obtain solutions with the three methods described for different values and discuss their salient features.

Order-reduced & full system solutions

To quantify the performance of the different methods ORDI, ORII, and FSII we monitor the residual of the original equations (4.23) and (4.24) (which requires evaluating up to fourth-order derivatives of the metric) or their order reduced version (containing up to second-order derivatives of the metric). We focus first on results obtained with ORDI and ORII. For this set of simulations, we take the initial scalar field to have amplitude $A=1\times 10^{-3}$, to be centered at $r_c=20M$ and of width $\sigma=1$.

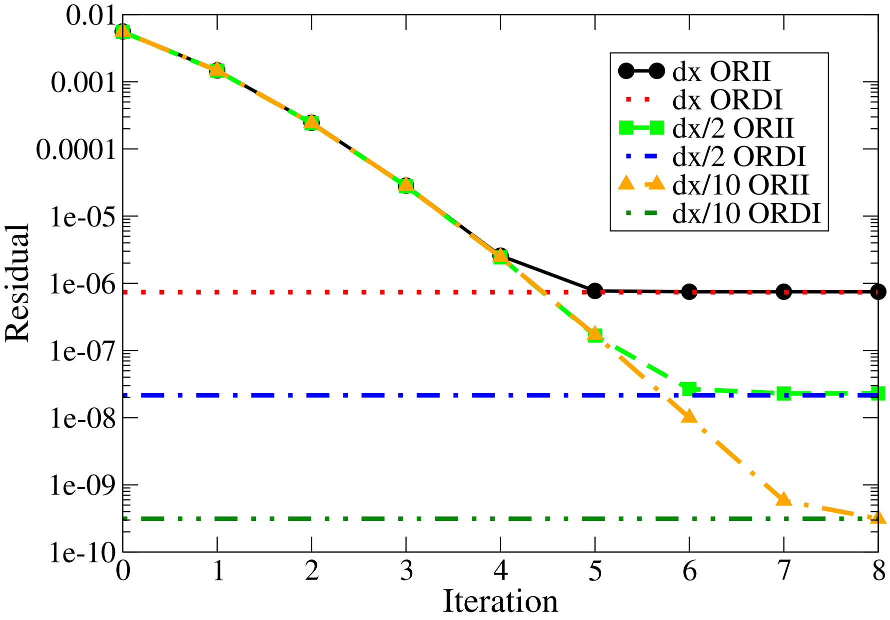

Figure 4.1: Residuals of equation (4.23) for the iterative solutions as a function of the iteration step. The constant horizontal lines represent the residuals from the ORDI solutions for comparison purposes. The different resolutions used are $dx = 0.018M$, $dx/2$ and $dx/10$. The residuals of the iterative solutions approach those of the ORDI solutions after a sufficient number of iteration steps. (We note in passing the convergence order measured for solutions obtained with the ORDI and the ORII methods—for a sufficient number of iterations in the latter case—is consistent with the 4th order accuracy of our solver.)

Figure 4.1 displays, for the case $\epsilon = 0.01$, the *order reduced* residual of the extended Hamiltonian constraint (eqn. (4.23)) for solutions obtained with the ORDI and ORII approaches as a function of the number of iterations performed. The figure shows the results with spatial resolutions $dx = 0.018M$, $dx/2$, and $dx/10$. For the iterated option (ORII), several iterations are required to converge to the solution, which, in turn, depends on the spatial resolution. For higher resolutions, a larger number of iterations is required to achieve such a solution. The ORDI method provides a solution that, from the get-go, gives a residual consistent with that obtained via the iterative method in the “asymptotic” (large number of iterations) regime. Figure 4.2 shows the same residual but now for different values of ϵ and a single discretization resolution. As can be appreciated, a higher number of iterations is required in the ORII method to obtain the solution for larger values of the coupling. The ORDI method, on the other hand, achieves such a solution at once.

It is important, however, to also examine the behavior of the FSII. To that end, we contrast the norm of the extended Hamiltonian residual—in full form, i.e., not the order reduced one— equation (4.23) evaluated with the solution obtained with the ORDI and FSII methods. Figure 4.3 shows the residual norm for $dx = 0.009M$ as a function of ϵ. For small coupling values, the residual obtained with the FSII method converges with a higher power of ϵ for more iterations, but this behavior degrades as the coupling increases. This is a consequence of "corrections" to the Hamiltonian in GR becoming too strong and a related loss of convergence with iteration. The solution provided by the ORDI method gives an error consistent with the expected ϵ^2 behavior as the original Hamiltonian was reduced to such order (as discussed, this can be formally improved to higher order in a rather direct fashion).

The behavior of residuals obtained from the extended momentum constraint is simple for our adopted free data. In this equation, the contributions from the extension are non-zero only close to the matter sources. Indeed, having chosen an initial scalar field profile supported far from the black hole, the beyond GR terms are significantly smaller than the matter terms. As a consequence, the different methods provide solutions of similar accuracy (the latter with just one iteration) in all cases studied. Of course, this behavior need not be true for other boundary conditions, gauge choice, or location of matter sources.

From these studies, one can draw that, in broad terms, the different approaches can be exploited to obtain solutions reaching comparable accuracy. In the ORII iterative method, a sufficient number of iterations must be however performed. This number is dependent on truncation error (i.e., governed by dx) and physical (i.e., ϵ) parameters. The ORDI method, on the other hand, produces a residual only dependent on truncation error (with respect to the order-reduced form of the constraint). Finally, the FSII approach yields an increasingly accurate solution in terms of ϵ for sufficiently small couplings, but convergence is lost for stronger ones. We note in passing that these results also provide some sense of the error magnitude that can accumulate using a perturbative method during the evolution. Depending on the number of iterations (or the perturbative order kept), an error of the order seen in figure 4.2 would arguably be introduced, and its accumulation over the time-length of the simulation can be significant unless the coupling considered is sufficiently small.

Henceforth, we will adopt the solutions obtained with the ORDI method to study the behavior of perturbed black holes in this theory.

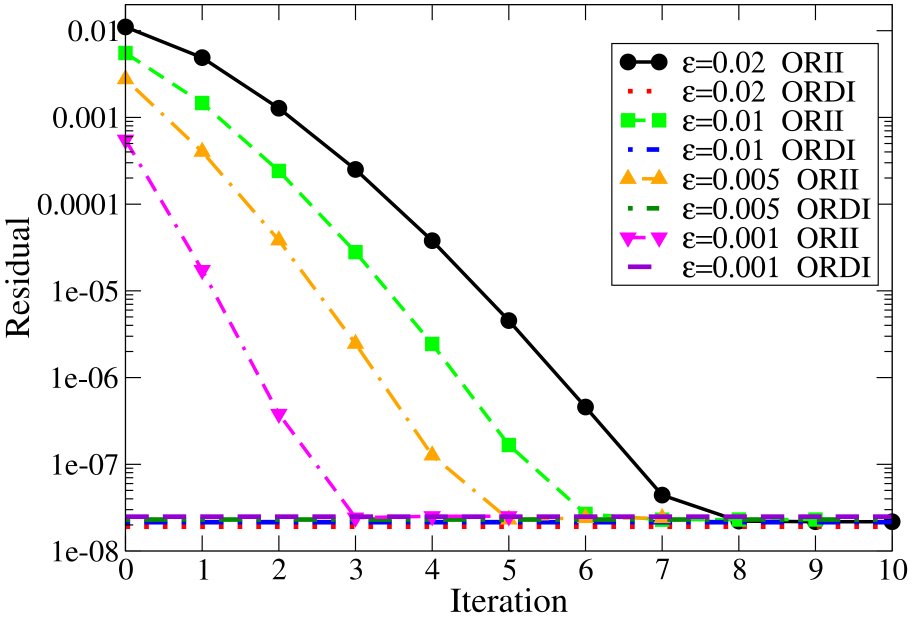

Figure 4.2: Residuals of equation (4.23) for the iterative solutions with respect to the number of iterations and for a range of coupling values for $dx = 0.009M$. The horizontal dashed lines represent the residuals from the ORDI solutions.

Solutions' dependence on the coupling parameter

It is informative to examine the dependence of the apparent horizon on the coupling parameter ϵ. Figure 4.4 displays the apparent horizon areal radius and its change as the coupling ϵ increases for our initial data. The figure shows the value of the areal radius of the apparent horizons found numerically with our solutions as well as with the analytical (perturbative) solutions found in [54] as a function of $\epsilon\, M^{-6}$. A fit to our numerical data of the form $r_A^H = 2M + s\,\epsilon\, M^{-6} + q\,(\epsilon\, M^{-6})^2$ gives $s = 1.234$ and $q = -3.179$. This is in agreement with the expression obtained from the analytical (linear) solution where $s_{analytical} = 1.25$. Recall that while the equations giving rise to the solution of [54], and ours are linear in ϵ, the solutions will differ at higher orders due to boundary conditions and our solution with the ORDI method, which, in essence, provides a resummed solution. Thus, differences at order ϵ^2 are expected. Figure 4.4 illustrates both curves; as ϵ increases, the quadratic contribution leads the numerical solutions peeling off the analytical ones, with respect to the apparent horizon radius, though the difference is smaller than 3% for $\epsilon = 0.05M^6$.

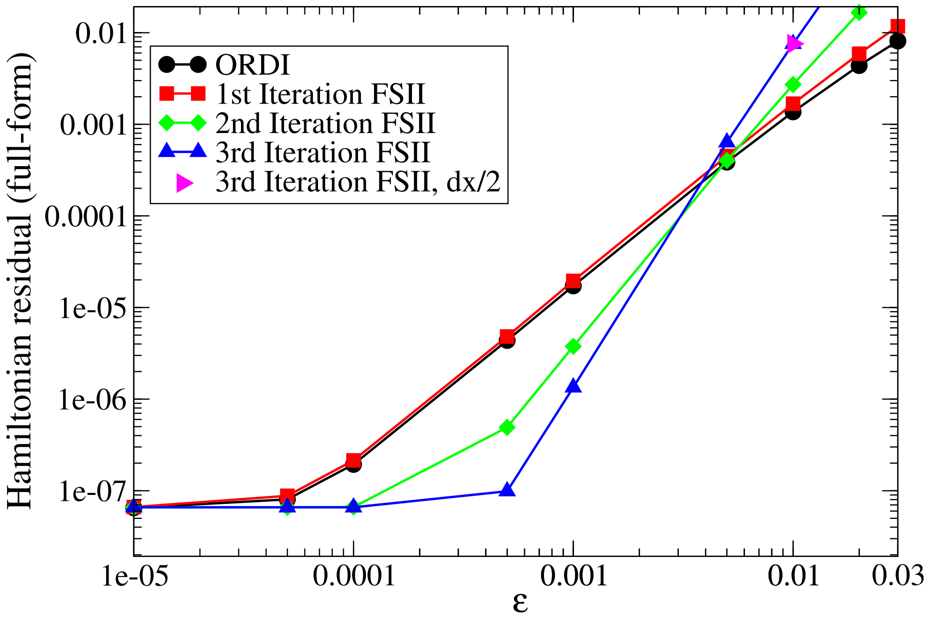

Figure 4.3: Full-form Hamiltonian residual norm for ORDI and FSII solutions for $dx = 0.009M$ as a function of ϵ.

To get a sense of the differences (magnitude and radial dependence) introduced by the correcting terms, figure 4.5 shows the relative difference between the conformal factor ψ obtained for different values of ϵ and the GR solution ($\epsilon = 0$). Departures from the GR solution, while very small asymptotically, become larger as the radius decreases, reaching values above 1%.

4.6.2 Dynamical behavior

We now turn our attention to the dynamical evolution of a (mainly) incoming self-gravitating scalar field configuration with different choices for its amplitude A together with several values for the coupling parameter ϵ. The values of $dx = 0.019M$, $\sigma = 0.018M$, and $r_c = 20M$ are fixed for all the results presented in this section.

As the evolution proceeds, a common qualitative behavior is seen in all cases; namely, much of the scalar field falls towards the black hole interacting with it while a small portion of the initial scalar field leaves the computational domain in a short time (afterward, the resulting spacetime has an asymptotic mass $M_{as} = 0.9998$ in the domain explored by

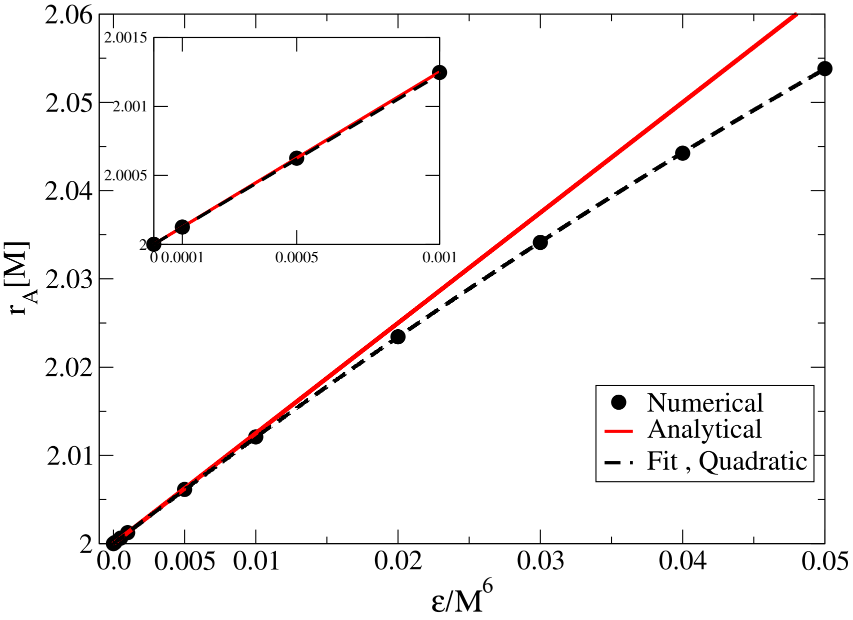

Figure 4.4: Areal radius of the apparent horizon for different values of the coupling ϵ, for initial data with $A = 0$. Black dots correspond to our numerical solutions, the black dashed line represents the quadratic fit to such data and the red solid line represents the areal radius of the horizon for the analytical solutions found in [54].

the numerical implementation). To provide a quantitative understanding of the ensuing dynamics, we focus on the behavior of the: *apparent horizon*, *quasi-normal behavior of the scalar radiation* and *suitable geometric invariants*.

Apparent horizon

As the scalar field falls into the black hole, the area of the event horizon (an thus its mass) grows but a closer inspection reveals a subtle and a priori unexpected dependence on ϵ.

Figure 4.6 shows the apparent horizon area (normalized by the initial area in the $\epsilon = 0$ case) as a function of time for different values of the coupling parameter ϵ. All of the simulations used to make Figure 4.6 present a black hole with initial irreducible mass $M_i = 0.8933$ a final mass of $M_f = 0.9998$, while the initial mass of the full spacetime is $M = 1.0$ and the amplitude of the scalar pulse is $A = 1 \times 10^{-3}$.

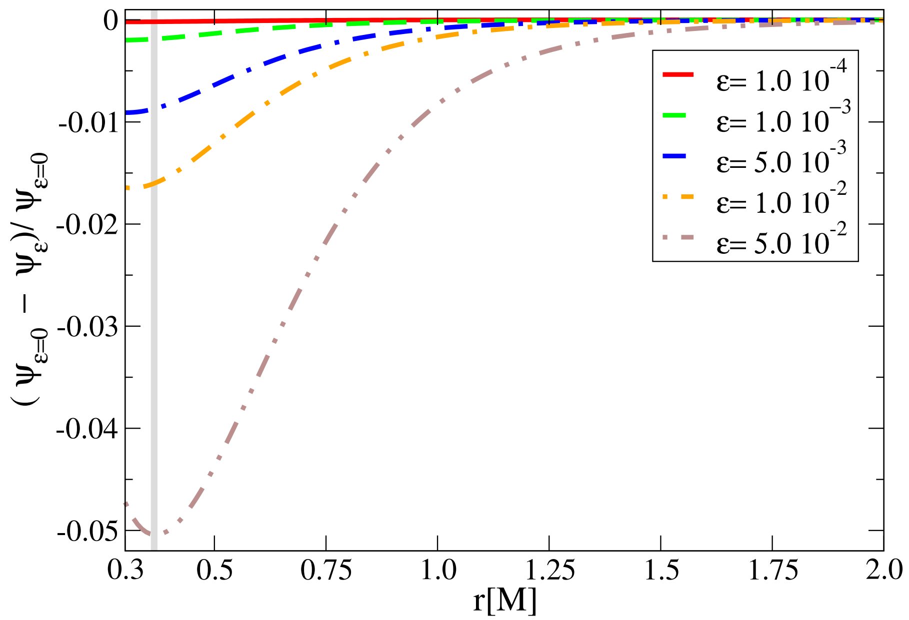

Figure 4.5: Relative difference $(\psi_{\epsilon=0} - \psi_\epsilon)/\psi_{\epsilon=0}$ for different values of the coupling parameter ϵ as a function of the coordinate radius r. The gray vertical line is included to guide the eye, indicating the apparent horizon locations(which vary with ϵ) .

The overall behavior for all of these curves is similar; namely, the horizon grows as scalar field energy is accreted until it reaches an approximately stationary state describing a black hole with a mass up to ≈ 12% larger. The case with $\epsilon = 0$, as expected, gives rise to a non-decreasing behavior of the apparent horizon area. However, subtle details can be seen with $\epsilon \neq 0$, which are more marked for larger values of the coupling parameter.

First, one observes an initial transient growth in the apparent horizon area even though no scalar field energy has been accreted. This behavior is not surprising, however, as it related to the initial data adopted, which is non-stationary. The future development of the initial data after the transient stage reveals a transition to a new intermediate (i) stage when the apparent horizon area does not change until the (main) accretion stage ensues. At late times, the solution is described by an essentially stationary final (f) configuration. The asymptotic state described by the apparent horizon (and thus an excellent approximation to the event horizon), can be understood by computing the fraction $A_\epsilon(M_f)/A_0(M_f)$ of the black hole and compared it to the fraction $A_\epsilon(M_i)/A_0(M_i)$ at the initial time, or with the area during the intermediate stage. In figure 4.7 we show these quantities as well as the one corresponding to the analytical solution from [54] as a function of ϵ. As this figure

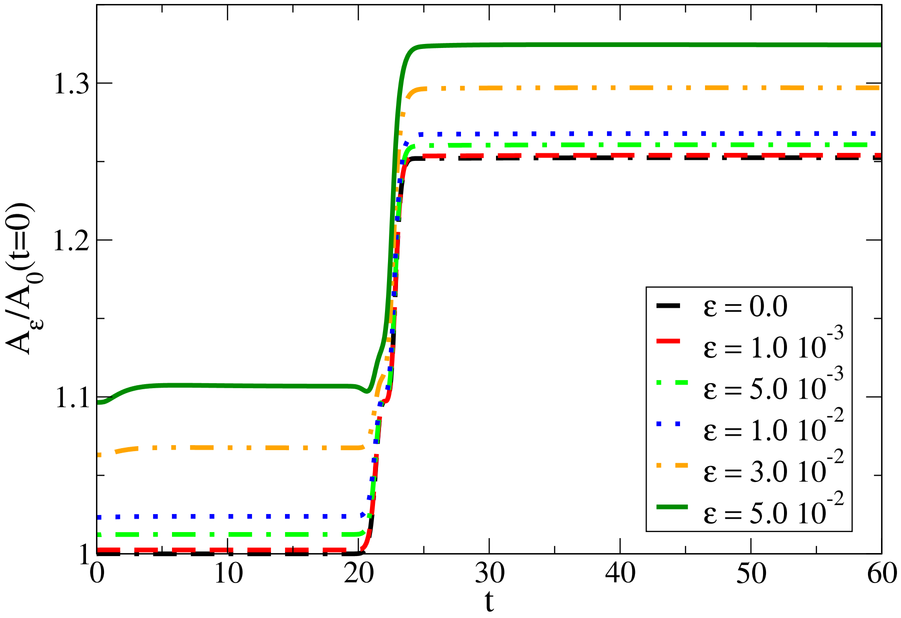

Figure 4.6: Area of the apparent horizon as a function of time for different values of ϵ. All curves are normalized by the corresponding initial area in GR (i.e., $\epsilon = 0$). The initial irreducible mass for all cases is $M_i = 0.8933$, the final $M_f = 0.9998$, and the total mass of the spacetime $M = 1.0$.

shows, the curves for intermediate and late-time solutions match the curve for the analytical solution at small couplings and for the corresponding masses. Indeed, a quadratic fit of the form $A_\epsilon/A_0 = 1 + s\,\epsilon\, M_e^{-6} + q\ (\epsilon\, M_e^{-6})^2$ to our data to the area gives, $s_i = 1.251$ and $s_f = 1.252$ (here M_e is the irreducible mass estimated during the intermediate and final stages respectively: $M_e = 0.8933$ or $M_e = 0.9998$). These values agree with the analytical (linear) solution $s_a = 1.25$. Furthermore, the obtained values of q_i and q_f are also consistent with each other.

Second, and at first sight surprising, one sees a momentary *small decrease* in the area of the apparent horizon as the scalar field interacts with it; this behavior is more marked for larger values of ϵ. This effect, when seen through the lens of GR can be traced to the failure of the null convergence condition (NCC). In such cases, the area of the event horizon—and hence that of the apparent horizon—can decrease in size [110, 111, 22].

To examine the NCC, we monitor $R_\pm \equiv R_{ab} k^a_\pm k^b_\pm$, where $k^a_\pm$ are the only (up to multiplicative factors) future-directed null vectors present in spherical symmetry. Their expres-

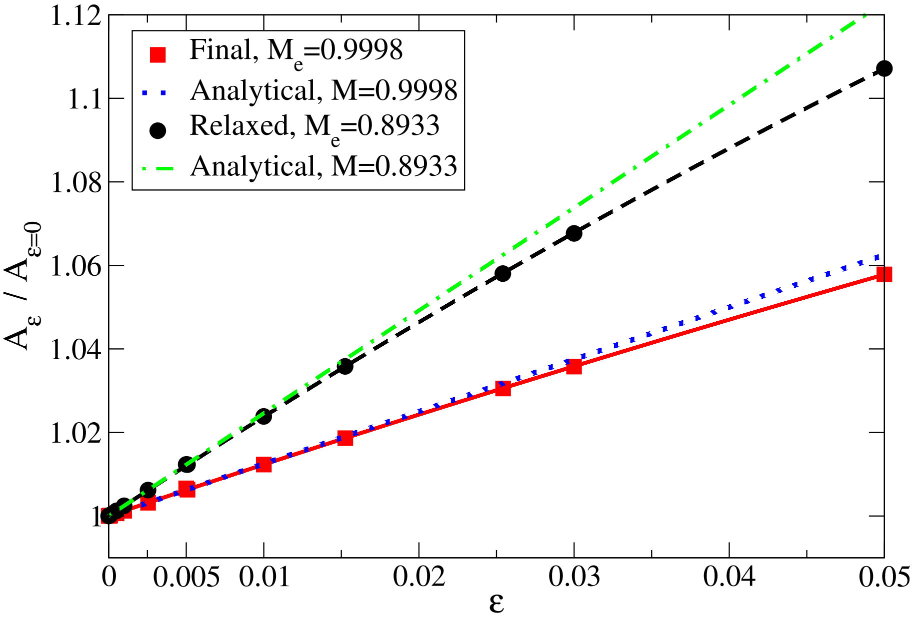

Figure 4.7: A_ϵ/A_0 as a function of ϵ at two particular instances. Red squares denote the late-time solution, and the solid red line is its quadratic fit. Black circles correspond to the intermediate solution, and the dashed black line is its quadratic fit. The dotted blue and dashed and dotted green lines correspond to the analytical solutions of [54] for $M = 0.9998$ and $M = 0.8933$ respectively.

sions are given by:

$$k^a_\pm = \left(1, -\beta \pm \frac{\alpha}{\sqrt{g_{rr}}}, 0, 0\right) \tag{4.42}$$

Figure 4.8 shows the value of R_- evaluated at the apparent horizon as a function of time for several values of ϵ. Clearly, the NCC is violated at all times for the $\epsilon \neq 0$ solutions, and this violation becomes more marked as the coupling ϵ increases.

Figure 4.9 presents a snapshot of R_- as a function of coordinate radius r at coordinate time $t = 150M$ for different values of ϵ. The NCC violations They are not only present in the vicinity of the apparent horizon but persist in the whole spatial domain.

Similar results are found for R_+, for which the NCC is also violated. The violation of the NCC also stresses that the dynamics within extensions to GR can display surprising phenomena that must be understood for potential implications on gravitational wave data.

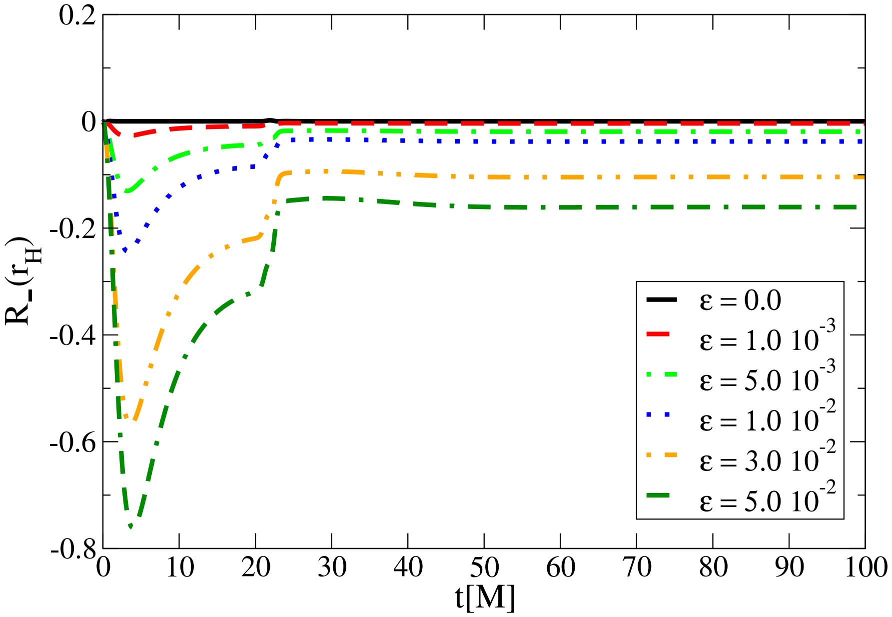

Figure 4.8: R_{-} evaluated at the apparent horizon as a function of coordinate time t for several values of ϵ.

Ringing and QNM

In GR, the (linearized) study of perturbed black holes reveals a quasi-normal behavior where the radiation fields (scalar, vector or tensor modes) are largely described by a set of exponentially decaying oscillations with decay rate and oscillation frequency tightly tied to the black hole parameters (mass and angular momentum). While the existence of analog modes for black holes in generic EFT-motivated theories have not been rigorously analyzed, at an intuitive level, a similar behavior is expected if black holes in such theories (and within the EFT regime) are stable[3]. We here study this behavior for the scalar field in spherical symmetry ($l = m = 0$), which we fit to a behavior given by,

$$\phi(t,r) = \sum_{n=0}^{\infty} c_n \exp(i\omega_n(t-r)), \tag{4.43}$$

---

[3] After all, perturbations are described still by propagating waves in a leaky cavity—losing energy into the black hole or radiated to infinity—and the spacetime is described by a small set of parameters $\{M, J, \epsilon\}$ which would determine the decaying/oscillatory behavior.

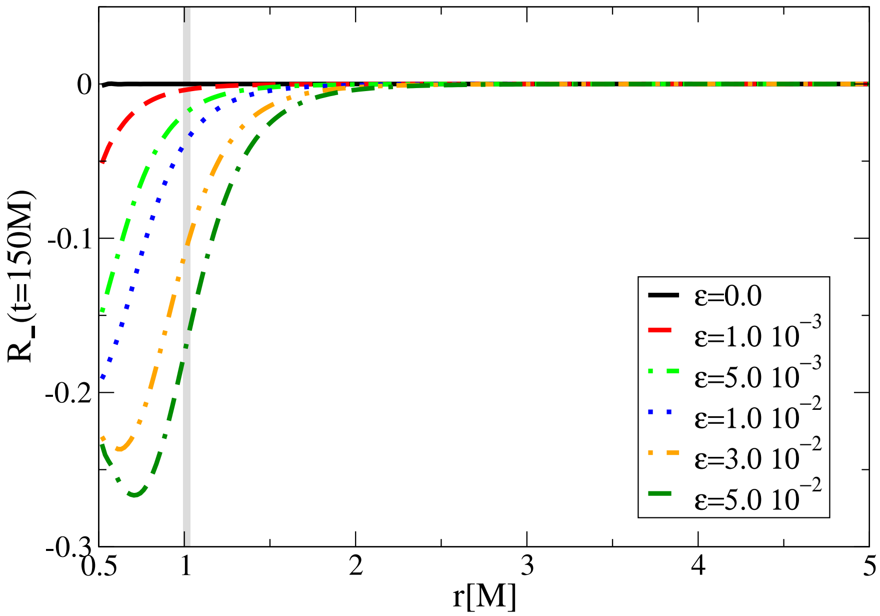

Figure 4.9: R_{-} at $t = 150M$ as a function of coordinate radius r for several values of ϵ. The gray vertical line is included to guide the eye, indicating the apparent horizon locations.)

where ω_n are complex frequencies and n is the overtone index. As expected, a behavior akin to the familiar quasi-normal ringing is observed, as can be appreciated in figure 4.10 which shows the scalar field behavior at a large distance vs. time. The field is dominated by the presence of damped oscillations with a subtle dependence on ϵ. This figure also shows a transition between a QNM behavior and a power-law tail-dominated one. The power law exponent we observe on these curves is t^{-3} and is thus consistent with analytical and numerical predictions for this mode in the GR case.

For a quantitative analysis, we focus on the least damped $l = m = n = 0$ mode. We extract the value of the field at an areal radius $r_A = 60M$ for three cases defined by initial amplitudes of the scalar field, a weak one of $A = 10^{-9}$, and two strong ones with $A = 10^{-3}$ or $A = 1.5\,10^{-3}$) centered initially at coordinate radius $r = 20M$ and width $\sigma = 1.0M$. In the strong field cases, the final mass of the black hole increases by $\approx 12\%$ and $\approx 32\%$ respectively after accretion. We extract both the real, ω^R, and imaginary ω^I frequencies and focus on their dependence on the coupling parameter ϵ. Figure 4.11 illustrates our results taking the ratio of the obtained values with respect to the ones for the GR case. The QNM frequencies values obtained for the GR simulation ($\epsilon = 0$) are $\omega^R = 0.109$ and $\omega^I = 0.104$ and are within 1% from the known values predicted by linear perturbation

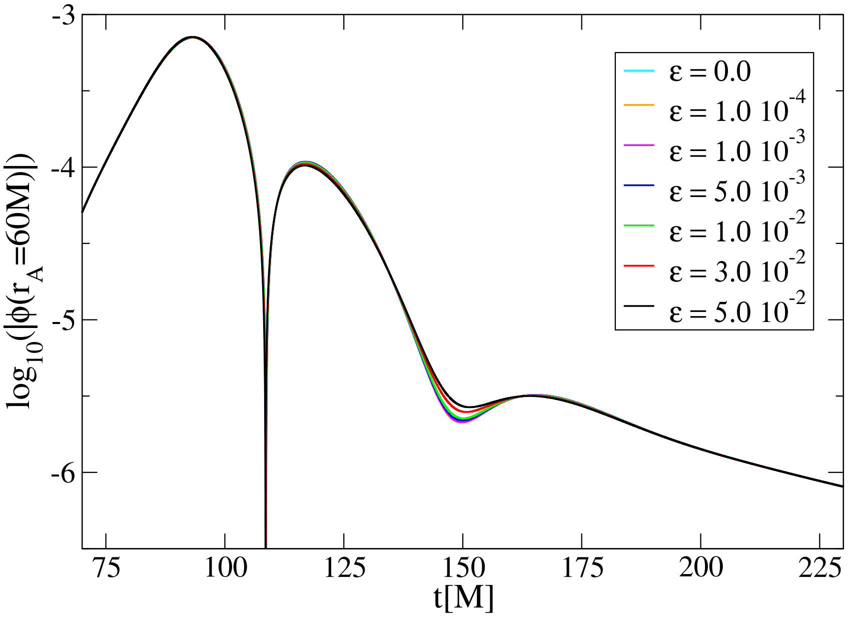

Figure 4.10: $\log(|\phi|)$ at areal radius $r_A = 60M$ as a function of coordinate (i.e., asymptotic) time for a wide range of values of ϵ.

theory [132, 31]. As can be appreciated in the figure, there is a somewhat larger deviation for ω^R than for ω^I. A general, simple, quadratic fit for both cases is,

$$\omega^R = \omega^R_{GR}(1 - 0.54\epsilon + 0.77\epsilon^2), \tag{4.44}$$

$$\omega^I = \omega^I_{GR}(1 + 0.45\epsilon - 1.33\epsilon^2). \tag{4.45}$$

Furthermore, we have observed that this scaling is independent of the initial amplitudes A of the scalar field and of the timescale τ introduced in equation (4.14). We have found that this scaling is in good agreement with the analytical study of QNM frequencies for black holes in higher derivative theories [51] (including the one studied here). In our notation, their predictions translate to:

$$\omega^R_{analytical} = \omega^R_{GR}(1 - 0.503\epsilon), \tag{4.46}$$

$$\omega^I_{analytical} = \omega^I_{GR}(1 + 0.484\epsilon). \tag{4.47}$$

The discrepancy in the correcting factor is $\approx 7\%$ between our numerical prediction and their perturbative, analytical treatment.

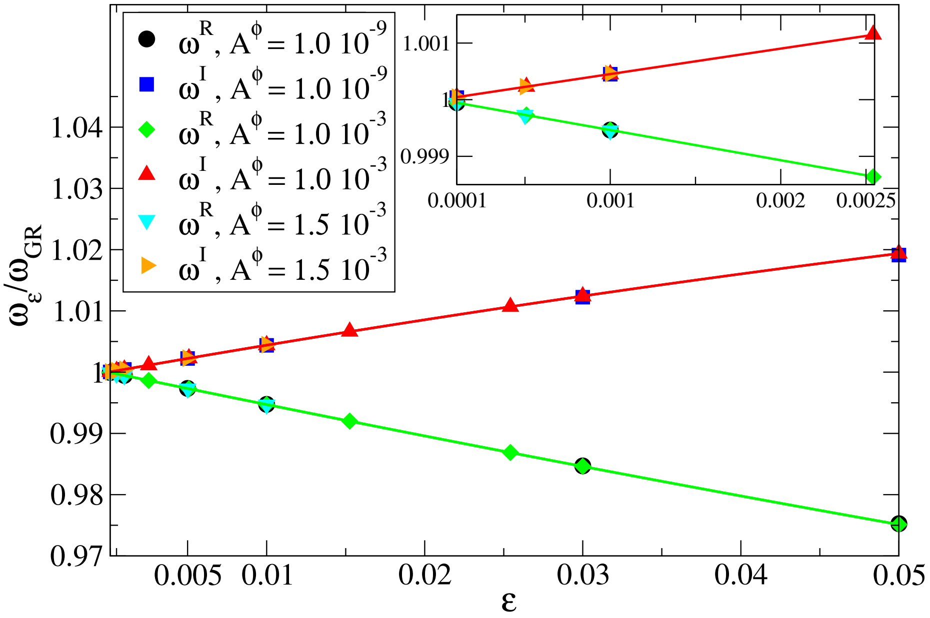

Figure 4.11: Relative QNM frequency for the strong and weak field cases as a function of ϵ. The solid lines in the plot are quadratic fits to the numerical data. The obtained parameters are in agreement between the weak and strong field cases.

Curvature invariant

As a final step, we monitor the scalar curvature invariant $\mathcal{C} \equiv R^{abcd}R_{abcd}$ to obtain further insights on the spacetime.

Figure 4.12 shows the value of $\mathcal{C}_N \equiv 4/3\,\mathcal{C}M_H^4$ (normalized this way as $\mathcal{C}_N = 1$ for a Schwarzschild black hole) evaluated at the apparent horizon as a function of time for different values of the coupling parameter ϵ (where M_H is the irreducible mass of the apparent horizon, an ϵ-dependent quantity in this theory). Note that the $\epsilon = 0$ curve departs from 1 only when the black hole is accreting the scalar pulse, and the Schwarzschild geometry does not describe the local solution. For non-zero coupling values, $\mathcal{C}_N$ departs further from 1 as ϵ increases. Since the black hole grows via accretion, the difference with respect to the value for Schwarzschild decreases after it increases as corrections in the theory are governed by curvature. Turning our attention to the transient (accreting) stage, fluctuations induced by accretion vary strongly with ϵ, both in amplitude and functional dependence. This indicates interactions of the black hole and the scalar field are strongly modified in this theory. The figure also includes two curves ($\tau = 0.002$ and $\tau = 0.005$)

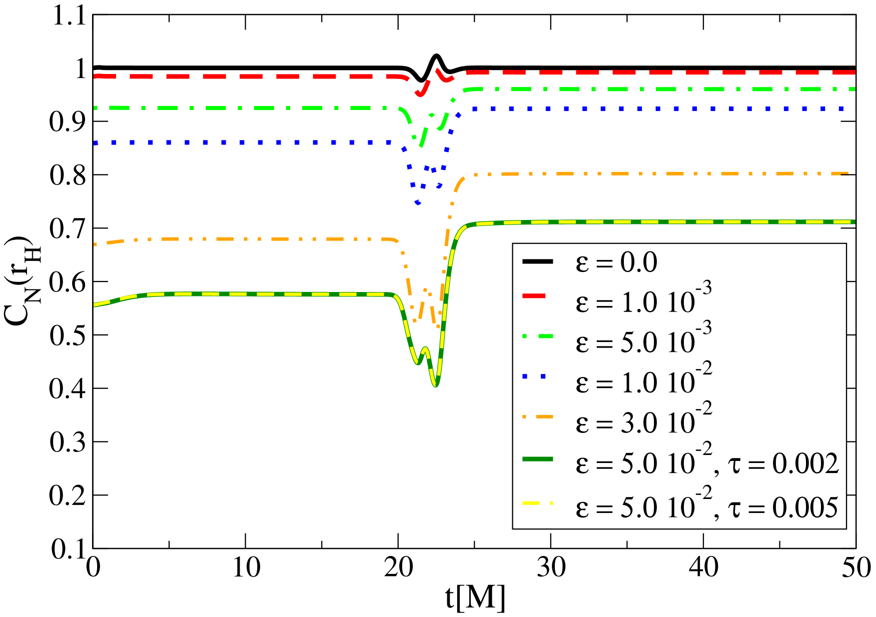

Figure 4.12: $\mathcal{C}_N \equiv 4/3\,\mathcal{C}M_H^4$ evaluated at the apparent horizon as a function of t for different values of ϵ. The case $\epsilon = 0.05$ is also presented with a longer time scale $\tau = 0.005$.

for the strongest coupling case ($\epsilon = 0.05$) to illustrate our results are independent of the timescale τ.

Figure 4.13 shows the values of $\mathcal{C}_N$ (evaluated at the apparent horizon) as a function of ϵ at two particular times, $t = 10M$ and $t = 150M$, that describe black holes that are approximately stationary during the intermediate and final stages. Additionally, we include the analytical value computed with the black hole solution found on [54] and fits to our numerical values. The most evident feature of this figure is the apparent departure of our numerical solutions from the linear result, (which gives by $\mathcal{C}_N = 1 - 33/4\,\epsilon(M_H^{GR})^{-6}$ (where M_H^{GR} is the irreducible mass of the black hole in the $\epsilon = 0$ case.) for large enough values of ϵ. Performing a cubic fit of the form $\mathcal{C}_N = 1 + s\,\epsilon(M_e)^{-6} + q\,(\epsilon(M_e)^{-6})^2 + c\,(\epsilon(M_e)^{-6})^3$ to our data points, the fitted values of the linear term coefficient for the $t = 10M$ and $t = 150M$ solutions are $s = -8.22$ and $s = -8.23$ respectively. The results for the linear coefficients are in good agreement with the value $s = 8.25$ obtained with the analytical solution. We note that if $\mathcal{C}_N$ is plotted as a function of $\epsilon(M_e)^{-6}$ then the curves drawn for $t = 10M$ and $t = 150M$ match to an excellent degree.

In figure 4.14 we show the behavior of of $\mathcal{C}_S \equiv \mathcal{C}r_A^6/(48\,M_e^2)$ as function of the areal radius r_A for $t = 150M$ for a wide range of ϵ values along with the linear analytical

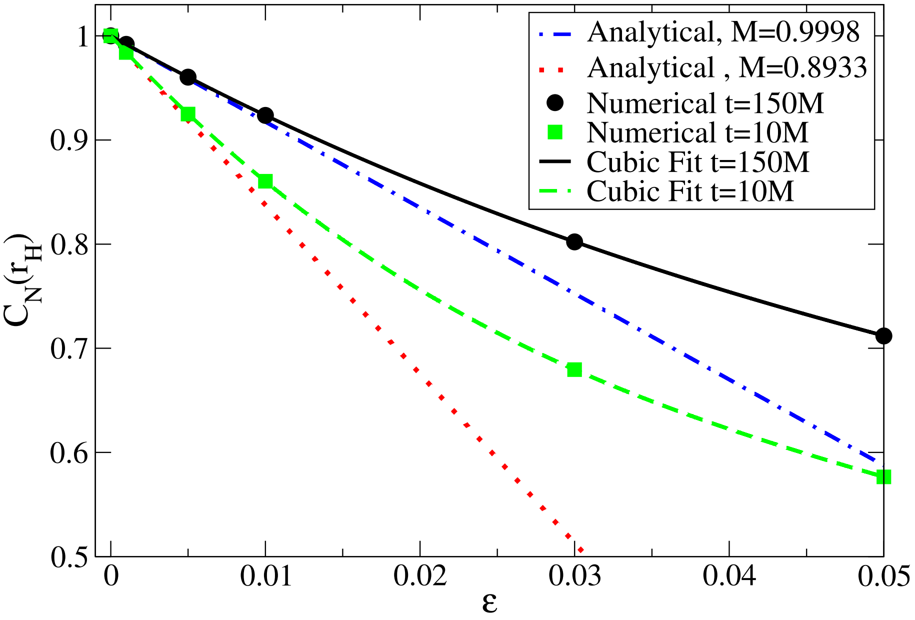

Figure 4.13: Green squares and black dots represent the value of $\mathcal{C}_N$ at the horizon for two coordinate times $t = 10M$ and $t = 150M$ as a function of ϵ. The green dashed line and the solid black lines are cubic fits to our numerical data. The dashed and dotted blue and dotted red lines display the prediction of $\mathcal{C}_N(r_H)$ from the solutions obtained in [54] for masses of $M = 0.9998$ and $M = 0.8933$ respectively.

predictions for this quantity. At far distances from the black hole, all curves approach the value 1 expected for a Schwarzschild black hole as expected—since corrections decay at a high rate with distance. The quantity peels off from the Schwarzschild value close to the black hole, and while such behavior is more marked—inside the black hole—it is non-trivial in its outer vicinity.

4.7 Discussion

In this chapter, we illustrated the implementation of a method to control the presence of higher derivative terms in extensions to GR. Using reduction of order techniques, we traded higher-time derivatives to eliminate Ostrogradsky's type ghosts and through the use of the *fixing the equations* method [56] we controlled higher-spatial derivatives. This combined approach allows us to treat highly complex non-linear theories with higher derivative con-

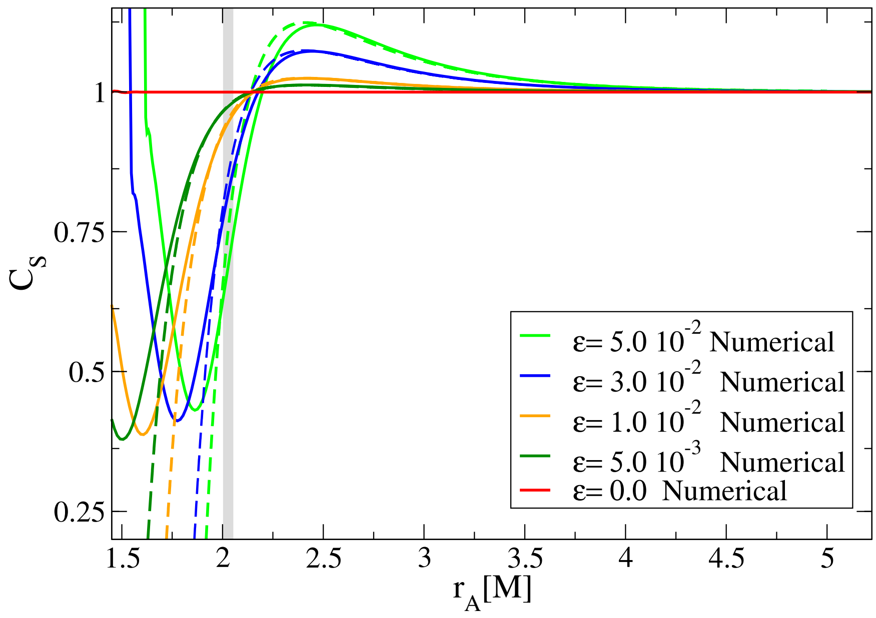

Figure 4.14: $\mathcal{C}_S$ as a function of areal radius r_A for different values of ϵ. The solid lines represent our numerical solutions for $t = 150M$ (describing a black hole of mass $M_{GR} = 0.9998$), while the dashed lines correspond to the analytical predictions of $\mathcal{C}_S$ from the solution in [54]. The gray vertical line is included to guide the eye, indicating the apparent horizon locations.

tributions in a non-iterative fashion (which can also be referred to as non-perturbative from the point of view of how correcting terms are handled. See e.g. [151] for such a perturbative approach).

We illustrated the benefits of proceeding this way by studying the dynamics of a self-gravitating scalar field in a spherically symmetric black hole spacetime within a theory displaying derivatives up to 4th order and corrections to GR (with combined gradient co, requiring$\lambda^{-8}\Lambda^{-6}$). We described how initial data can be constructed directly integrating the resulting constraint equations and contrasted the solution with those obtained with iterated/perturbative approaches. Our results demonstrate that, for sufficiently weak couplings, the solutions agree, but for larger ones there is increasing disagreement, and a larger number of iterations might be required to achieve a sufficiently small residual. In particular, this observation gives a sense of the potential size of the error that would be incurred and accumulated in dynamical studies utilizing an iterated approach restricted to just the first correction (or treated perturbatively to first order).

Studying the future development of data describing a scalar field perturbing a black hole in such theories, we observed the apparent horizon can reduce in size due to the NCC being violated. The scalar field also displays a QNM behavior reminiscent of that familiar in GR, but with decaying and frequency rates that differ more strongly for larger couplings. In particular, we find that the relative differences in decay rate and oscillatory frequency scale as $\simeq 0.5\epsilon$. These results can help further inform approaches to parameterize deviations from GR signals by making explicit connections with putative theories.

We note a potential further challenge at a practical level; namely, accurately evaluating high derivatives requires sufficient precision. Otherwise, a significant loss of accuracy might ensue. This point can be relevant in deciding the most convenient discretization technique at the numerical level. Alternatively, it is tempting to employ field redefinitions to (attempt to) reduce higher derivatives as non-linear combinations of lower order ones (see e.g. [173]). The extent to which this program would be successful will depend on the particular theory being explored. Regardless, even if one could reduce all higher derivatives to, at most second-order ones, one would still face mathematical obstructions (see e.g. [153, 161, 29, 128]). At a practical level, this would require an approach like the one explored in this work to control them.

Finally, while this study is restricted to a particular theory and within the simpler setting of spherical symmetry, the robustness, and generalities of the techniques adopted give strong backing for their use in general scenarios.

Chapter 5

Black hole binary mergers in Effective field theory extension to GR

5.1 Introduction

In the previous chapter, we demonstrated how it is possible to conduct studies of highly nonlinear gravitational spacetimes in the context of an EFT extension to GR. In this chapter, we go a step further to consider less restrictive (e.i., no symmetry assumptions) scenarios, which are also extremely relevant from an astrophysical standpoint. This is to study the evolution of BH binaries in quasi-circular orbits all the way to the merger. This scenario requires further considerations not arising in the previously simplified regimes; here, the BHs will move through the grid to reach relativistic speeds, so the strategy we employ has to be able to properly track this motion. In spirit, the methods used in this chapter are the same as the ones used in 4, both a *Fixing* strategy and *Order Reduction* will be used to recast the equations in a form we can evolve numerically. However, the specific implementation of these methods differs to better adapt to the scenario of interest. To build up to the binary scenario, we first study a simplified prototypical example as well as the single-boosted BH scenario. With these new considerations, we are able to carry out simulations in the binary merger scenario and study the effects of modifications on the dynamics and the GW emission.

The chapter is organized as follows. In section 5.2, we present the theory of interest and the relevant field equations. Section 5.3 presents a prototypical example of a higher-derivative wave-like equation. The treatment of this toy model helps to motivate the proposed treatment of the gravitational system, which is presented in section 5.4. Details of the initial data prescription and the evolution scheme are detailed in sections 5.5 and 5.6, respectively. Results for the single boosted BH case are presented in section 5.7, while results for the binary BH scenario and GW emission are discussed in section 5.8. Sections 5.9 and 5.10 discuss considerations in the choice of fixing parameters and the choice of fixing equation, respectively. The chapter concludes in section 5.11 with a discussion. Further details on excision and convergence are presented in Appendix D. Lastly, we employ geometrized units ($G = c = 1$), use early Latin letters in the alphabet to denote spacetime indices, and use the latter part of the Latin alphabet for spatial indices.

5.2 Focusing on a specific theory

While we could take any of a plethora of proposed beyond GR theories –almost all sharing the problems alluded to earlier–, for definiteness here we consider a specific extension to GR derived naturally from EFT arguments [84]. In this approach, high energy (i.e., above the cut-off scale) degrees of freedom are integrated out, and their effects are effectively accounted for through higher-order operators acting on the lower energy ones. For the case of gravitational interactions, in vacuum, assuming parity symmetry and accounting for the simplest contribution, such an approach yields under natural assumptions:[1]

$$I_{\text{eff}} = \frac{1}{16\pi G}\int d^4x\,\sqrt{-g}\{R - \frac{1}{\Lambda^6}\,\mathcal{C}^2 + \cdots\},, \tag{5.1}$$

where $\mathcal{C} = R_{abcd}R^{abcd}$ and the coupling scale Λ has units of $[M_S]^{-1}$ for some scale M_S. The equations of motion are $G_{ab} = 8\,\epsilon\, H_{ab}$, with G_{ab} the Einstein tensor, $\epsilon \equiv \Lambda^{-6}$ and

$$\begin{aligned} H_{ab} &= \mathcal{C}\left(\Box R_{ab} - \frac{1}{2}\nabla_a\nabla_b R - \frac{1}{16}\mathcal{C}g_{ab} - R_{ac}\,R^{c}{}_{b} + R^{cd}R_{acbd} + \frac{1}{2}\,R_{adec}R_{b}{}^{dec}\right) \\ &\quad +2(\nabla^c\mathcal{C})\left(\nabla_c R_{ab} - \nabla_{(a}R_{b)c}\right) + R_{a}{}^{c}{}_{b}{}^{d}\nabla_c\nabla_d\mathcal{C}\,. \end{aligned} \tag{5.2}$$

H_{ab} is covariantly conserved since it is derived from an action possessing local diffeomorphism invariance.

In GR ($\epsilon = 0$) the resulting EOMs can be shown to define a hyperbolic, linearly degenerate, nonlinear, second order, PDE system of equations with constraints (e.g., [163]). With suitable coordinate conditions, characteristics are given by the light cones and do not

---

[1] Other operators at this (and even lower) orders can be considered, though without loss of generality with regards to our goals, we ignore them here to not overly complicate the presentation.

cross –thus shocks or discontinuities cannot arise. The right-hand side (RHS), however, spoils all these considerations. Derivative operators higher than second order appear – which render the equations outside formal PDE classifications. *How is one to approach the study of this problem?* First, one can simplify the EOMs somewhat by applying an order reduction and replacing the Ricci tensor and the Ricci scalar. Since in this work we consider vacuum spacetimes $R \sim \mathcal{O}(\epsilon)$, the contribution of the Ricci tensor to the RHS is $\mathcal{O}(\epsilon^2)$ and we can ignore it at the order that we are considering. We are left with the following EOMs at $\mathcal{O}(\epsilon)$:

$$G_{ab} = \epsilon \left(4\,\mathcal{C}\, W_a{}^{cde}\, W_{bcde} - \frac{g_{ab}}{2}\,\mathcal{C}^2 + 8\, W_a{}^c{}_b{}^d \nabla_c \nabla_d \mathcal{C} \right) , \tag{5.3}$$

where W_{abcd} is the Weyl tensor since $R_{abcd} = W_{abcd} + \mathcal{O}(\epsilon)$. Then, $\mathcal{C} = W_{abcd}\, W^{abcd}$. System (5.3), containing derivatives up to fourth order of the spacetime metric (in $\nabla_a \nabla_b \mathcal{C}$), has no proper classification within PDE theory.

5.3 Prototypical model

For interacting binaries one must deal with strong curvature regions which move and, crucially, merge. A successful general strategy must account for the backreaction of corrections onto the motion itself. Otherwise, at least secular terms will spoil the accuracy (and hence usefulness) of the solution [16, 149, 159]. As a preliminary challenge, consider the following model that captures key aspects of the problem,

$$\Box \phi = -\epsilon\, \partial_t^4 \phi\,, \tag{5.4}$$

with $\Box$ denoting the standard d'Alembertian in Cartesian coordinates and a RHS, which spoils its mathematical character. At an intuitive level, one would regard the RHS as introducing small modulations on a solution that travels at the speed of light (assuming both a small parameter ϵ and regarding ϕ described by long-wavelength modes). However, a straightforward analysis indicates that the higher time derivatives lead to ghost modes that grow without bound. One can try to address this issue by 'order reduction'. That is, replacing: (A) $\partial_t^4 \phi \approx \partial_t^2 C(\phi)$, with $C(\phi) = \partial_{xx}\phi$ (the RHS of $\partial_t^2 \phi$ at zeroth order), or even (B) $\partial_t^4 \phi \approx \partial_x^4 \phi$. Depending on the sign of ϵ, Option (A) leads to high-frequency modes not propagating or blowing up, while (B) leads to even faster blowing up modes or acausal propagation. Neither is consistent with the intuition above. Generically, high-frequency modes are problematic.[2] While in linear problems a frequency cut-off could be introduced,

---

[2] Recall, numerical implementations continuously feed high-frequency modes through the discretization employed.

in nonlinear ones, such a strategy is uncertain due to mode couplings potentially feeding long wavelengths into short ones, and vice versa. The challenge is to control the equation, render the problem of interest well posed and achieve a method that incorporates the effect of corrections contemplated by the theory at long wavelengths while sensibly controlling short wavelengths; and, doing so without unduly increasing the cost of obtaining trustable solutions. In particular, it should allow inquiring whether a significant flow to the UV takes place, which would indicate that the original theory generically abandons the EFT regime for problems of interest –unless such UV flow takes place hidden behind a stable horizon. If the opposite is the case, to consistently incorporate the effect of corrections to the theory. To address this challenge, starting from option (A) above,[3] we fix the equation as

$$\Box\phi = -\epsilon\,\partial_t^2\hat{C}\,, \tag{5.5}$$

$$\tau\partial_0\hat{C} + \sigma(\partial_t^2 - 2\beta^i\partial_{ti} + \beta^i\beta^j\partial_{ij})\hat{C} = C(\phi) - \hat{C}\,, \tag{5.6}$$

with $\partial_0 = \partial_t - \beta^i\partial_i$ and β^i an "advection" vector. The resulting second-order system determines the evolution of the variable $\hat{C}$ that is damped towards the "source" $C(\phi)$ on a timescale σ/τ. Notice that a non-trivial stationary solution such that $C(\phi) = \hat{C}$ cannot be achieved for non-zero values of τ and σ (as the RHS is damped to zero, the left-hand side would continue to source it otherwise). The difference between $\hat{C}$ and its target value $C(\phi)$ decreases with τ and σ, and ultimately these parameters should be chosen to minimize this difference while preserving numerical stability. To demonstrate the effectiveness of $\hat{C}$ accounting for $C(\phi)$ (which we call "*Tracking*") and the numerical stability of the fixed system, we carried out a parameter exploration of τ and σ. We implement a 1D simulation in a periodic domain of size $L = 200$, discretized by a uniform grid, sixth-order accurate spatial derivatives, Runge-Kutta of fourth order for time stepping, and Kreiss-Oliger dissipation with $\Delta t/\Delta x = 1/4$. As initial data, we adopt $\phi(0,x) = 10^{-3}\,e^{-\frac{1}{2}(x-100)^2}$, with $\hat{C} = \phi_{,xx}$ and $\{\phi_{,t} = \phi_{,x}; \hat{C}_{,t} = \phi_{xxx}\}$ and fix $\epsilon = 10^{-3}$. We also choose $\beta^i = \delta^i_x$, coincident with the speed of propagation of the main pulse in the uncorrected equation. During the evolution, beyond the advection of the main 'pulse', the solution develops a distinctive long oscillatory tail as a result of the "correcting term", without high-frequency modes spoiling it. We evolve the system until the spatial extent of the tail becomes comparable to the size of the domain and compute a tracking measure as: $\mathcal{T}(C,\hat{C}) = \frac{||C(\phi)-\hat{C}||_2}{||C(\phi)||_2}$. This is shown in figure 5.1 for a range of $\{\sigma,\tau\}$, overall obtaining good tracking. Notice the existence of a region where evolutions fail for values of $\sigma < 10^{-4}$ as the equations become stiff, but we checked that a smaller timestep resolves this issue. Second, $\mathcal{T}$ improves linearly with

---

[3] Which is the most closely associated to our desired problem.

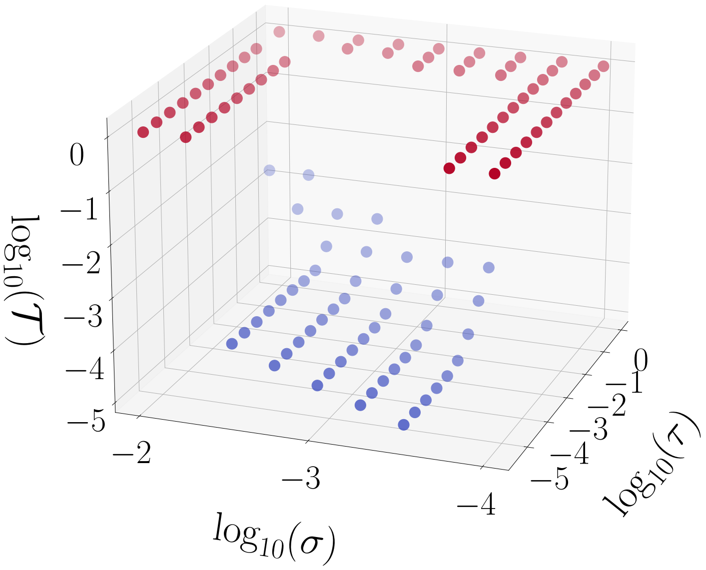

Figure 5.1: Tracking $\mathcal{T}$ for several values of σ and τ for a fixed value of $\epsilon = 10^{-3}$. In red we display the simulations that failed due to instabilities, and in blue the stable ones.

decreasing σ. Third, there is a linear dependence of $\mathcal{T}$ with τ for large values, while it flattens for smaller ones and $\mathcal{T}$ depends only on σ.

5.4 Gravity and Black holes

We turn now to the demanding task of simulating dynamical BH spacetimes (with single boosted BHs and binaries) in the chosen EFT extension to GR. Motivated by the previous discussion we *fix* the system (5.3) by introducing a new independent variable $\hat{\mathcal{C}}$ in the following way,

$$G_{ab} = \epsilon\Big(4\,\hat{\mathcal{C}}\,W_a{}^{cde}\,W_{bcde} - \frac{g_{ab}}{2}\,\hat{\mathcal{C}}^2 + 8\,W_a{}^c{}_b{}^d\,\nabla_c\nabla_d\hat{\mathcal{C}}\Big) \tag{5.7}$$

$$\left(\partial_t^2 - 2\beta^i\partial_{ti} + \beta^i\beta^j\partial_{ij}\right)\hat{\mathcal{C}} = \frac{1}{\sigma}\left(\mathcal{C} - \hat{\mathcal{C}} - \tau\partial_0\hat{\mathcal{C}}\right), \tag{5.8}$$

where second-time derivatives of the metric in the RHS are replaced –following a reduction of order strategy– using the zeroth order Einstein equations. The resulting system of equations involves at most second-time derivatives and $\hat{\mathcal{C}}$ is damped to the physical $\mathcal{C}$ on a timescale $\simeq \sigma/\tau$ (for our choices, up to $\simeq 10M_S$, which is shorter than any dynamical timescales in the system). As a result, beyond a lengthscale $\simeq \sigma^{1/2}$ (for our choices, up to $\simeq 0.2M_S$) the the system reduces to the original one, while shorter ones are damped and controlled, and we can explore even shorter scales through suitable extrapolation of our results. Notice that the operator ∂_0 with the advection vector (corresponding to the shift vector in the 3+1 decomposition) helps ensuring inflow towards the BH(s). As we shall see, this is enough to control the whole system. That a single scalar suffices to do so is related to such scalar encoding the only contribution of higher derivatives. Controlling it results in an overall effect ensuring high-frequency modes are kept at bay. Depending on the structure in other theories, one might need to introduce further quantities (see, e.g., [93]). Nevertheless, the overall strategy remains unchanged.

5.5 Initial data

We define initial data by a single (for the single BH case) or a superposition of boosted BHs as described in GR and dynamically "turn on" the coupling ϵ, bringing it from 0 to the desired value with a quadratic function in a window $t \in [10, 30]M$. This allows the coordinate conditions to settle before incorporating deviations from GR, inducing only smooth constraint violations (which are damped through the now standard use of constraint damping [40, 108]) and by-passing the solution of initial data problem within the EFT theory. This task in itself has also received limited formal and numerical attention. Again the presence of higher derivatives obscures the treatment.[4]

For initial data in the single BH case, we use a boosted BH solution derived from the conformal transverse-traceless decomposition [134, 185, 186], which uses an approximate conformal factor solution to the Hamiltonian constraint, valid for small boosts. For the binary BHs, we adopt Bowen-York-type-of initial data [39] describing two superposed equal mass, boosted, non-spinning BHs in a quasi-circular orbit. The individual masses are $m_i \approx 0.5M$, $i = 1, 2$, and the separation is $D \sim 12M$ (initial orbital frequency $\simeq 0.025/M$). The momenta are tuned so this binary is initially in quasi-circular motion, and in GR it describes 12 orbits before the merger (the initial BHs velocities are similar to those in the single boosted BH case).

---

[4] See [59] for the case of a perturbed BH in spherical symmetry and [127] for the construction of initial data in scalar-tensor theories of gravity.

5.6 Evolution

We use the `GRChombo` code [65, 17] and the CCZ4 formulation of the Einstein equations [14] (see also [30]) which implements the system (5.7)-(5.8) with a distributed adaptive mesh refinement capabilities,[5] using 6th order finite difference operators for the spatial derivatives and the method of lines for time integration through a Runge Kutta of 4th order.[6] In this way, we only need to use three ghost cells along each coordinate direction. We adopt a standard 1+log slicing condition for the lapse α and the Gamma-driver for the shift β^i, as implemented in the public version of the code and adopt Sommerfeld boundary conditions at the outer boundaries. We redefine the damping parameter $\kappa_1 \to \kappa_1/\alpha$ to ensure that it remains active inside the apparent horizon (AH) [15]; we decrease the damping parameter in the shift condition as well as increase σ in (5.8) at large distances from the center of the binary to ensure that no violation of the CFL condition arises due to grids becoming coarser with our explicit time-stepping strategy (e.g., [164]). Otherwise, the chosen values for the constraint damping, shift, and lapse conditions are $\{\kappa_1 = 1, \kappa_2 = -0.8, \kappa_3 = 1, \alpha_2 = \alpha_3 = 1, \alpha_1 = 2, \eta_1 = 0.75, \eta_2 = 1/M\}$ ([65]). In the code, the additional evolution equation (5.8) is implemented in the obvious first-order form. We excise a region of the interior of BHs as in [86], which removes the role of correcting terms, achieving stable evolutions with unduly high resolution.

With the total ADM mass M of the system setting a scale, our domain for the boosted BH case corresponds to the quadrant $x \in [-L, L]$ and $y, z \in [0, L]$ as symmetry allows for restricting it. We adopt $L = 384M$ with the coarsest grid spacing (for production runs) $\Delta = 2M$; we then add another six levels of refinement. For the BH binary case, the computational domain, exploiting symmetries, is given by $x, y \in [-L, L]$ and $z \in [0, L]$. In this case, we adopt $L = 512M$ and coarsest grid spacing (for production runs) $\Delta = 4M$; we then add another 8 levels of refinement (for convergence tests we consider up to $\Delta = 8/3M$ and the same number of refined levels). We extract the gravitational waves at six equally spaced radii between $R = 50M$ and $R = 100M$ and extrapolate the result to null infinity. In both cases we use the second (spatial) derivatives of the conformal factor[7] χ to estimate the local numerical error and determine whether a new level of refinement needs to be added; in addition, we fix the spatial extent of certain refinement levels to ensure that the resolution at the chosen extraction radii is high enough. Lastly, we choose a scale value $|\epsilon| = 10^{-5} M_S^6$, which implies a coupling scale for new physics beyond GR of $\Lambda \approx 7/M_S \simeq$

---

[5] Here we use a 2:1 mesh refinement ratio.

[6] We use 6th Kreiss-Oliger dissipation with a dissipation coefficient $\sigma_{\text{diss}} = 2$ (e.g., [49]).

[7] Recall that the conformal factor χ is one of the evolution variables in the CCZ4 formulation and it is related to the induced metric on the spatial slices γ_{ij} as $\chi = 1/(\det \gamma)^{\frac{1}{3}}$.

$5M_\odot/M_S$ km^{-1}. Notice for this small scale, correction effects will be undoubtedly subtle, with consequent high accuracy requirements to capture them. Here we undertake a first study mainly focused on demonstrating the ability of the method to control the system. We will concentrate on assessing this and obtaining a qualitative description of observed consequences. We consider both signs for ϵ, the negative case satisfies the constraints argued for in [72], and the positive one also provided azimuthal numbers of the solution are not large, which is our case. We here choose a conservative scale $M_S = 10M_\odot$, i.e., somewhat below (but comparable) to the curvature scale set by the masses of the individual BHs for all detected gravitational wave events. Choosing a smaller scale would imply that the modifications become $\mathcal{O}(1)$ during the inspiral [165] with arguably clear imprints on the observed signal, which is inconsistent with observations. Further, we note that it is natural to expect the scale to remain fixed, thus the larger the BH mass, the smaller the effect of corrections are. This observation is particularly relevant as the BHs merge, as corrections after such regime would naturally become smaller.[8] Since for larger masses corrections would be smaller, we here focus on masses comparable to the length scale M_S we thus adopt individual BH masses $m_i = M_S/2 = 5M_\odot$.

5.7 Single boosted black holes

We confirmed our strategy's ability to evolve boosted (and stationary) BHs, with the solution reaching a steady state behavior shortly after the corrections are fully turned on. The solution is smooth without inducing growth in high-frequency modes or signs of instability. Beyond GR effects are naturally larger in the BH region. By comparing the value of $\hat{\mathcal{C}}$ and $\mathcal{C}$, we confirm the former tracks the physical one quite well and that lower values of $\{\sigma, \tau\}$ improve the tracking behavior. Figure 5.2 shows profiles of $\mathcal{C}$ and $\hat{\mathcal{C}}$ for a fixed value of $\tau = 0.005$ and different values of σ. Figure 5.3 illustrates the observed behavior of $\mathcal{T}(\mathcal{C}, \hat{\mathcal{C}})$ for a collection of $\{\sigma, \tau\}$ values. Importantly, examination of the relative difference between two values of $\hat{\mathcal{C}}$ obtained with two different values of σ (and analogously with $\mathcal{C}$) indicates errors associated to the choice of this parameter do not severely accumulate, thus the solution is not degraded by strong secular effects (see Fig. 5.9). For instance, it would take $\approx 10^6 M$ for the relative error for Kretschmann scalar with $\sigma = 0.1$ and 0.05 to be of order $\mathcal{O}(1)$. Numerical instabilities develop for smaller values of σ around the excision region, well inside the AH; these instabilities are sensitive to the details of the excision. Other forms of excision could be more robust as σ is decreased

---

[8] Data analysis techniques can exploit these observations (e.g., [170, 75]).

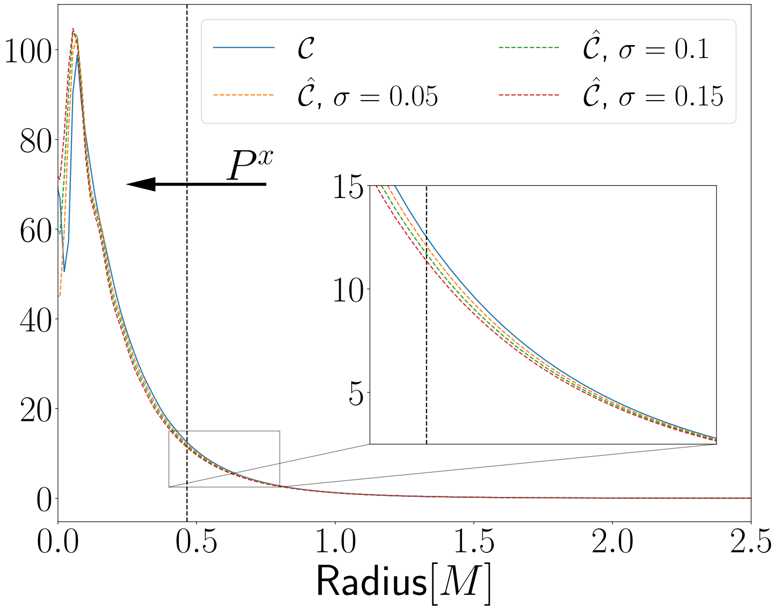

Figure 5.2: $\mathcal{C}$ and $\hat{\mathcal{C}}$ on a line starting from the puncture and trailing the boosted BH – where differences in tracking are larger– (at $t = 75M$, when all transients related to gauge and initial data have passed) for a fixed value of $\tau = 0.005$. The BH has mass $M = 0.5$ and momentum $P^x = 0.08M$. The vertical dashed black line denotes the location of the AH and the arrow indicates the direction of motion of the BH.

(e.g., [59]). With a successful handling of correction effects in single, moving BHs, we turn next to the challenging setting of binary BH mergers.

5.8 Black hole binary mergers

The binary tightens due to the emission of gravitational waves, which radiate energy and angular momentum from the system. The solution is smooth, without any signs of instability throughout the inspiral, merger, and ringdown. This can be seen in Figure 5.4, which shows snapshots of $\hat{\mathcal{C}}$ on the equatorial plane at these different stages. Figure 5.5 shows the gravitational wave strains for different values of ϵ and contrasts them with the corresponding one in GR. The corrections to GR and their high degree of non-linearity and higher gradients contributions certainly tax resolution requirements. Our studies here are not focused on quantitatively sharp answers, but on testing the approach with enough

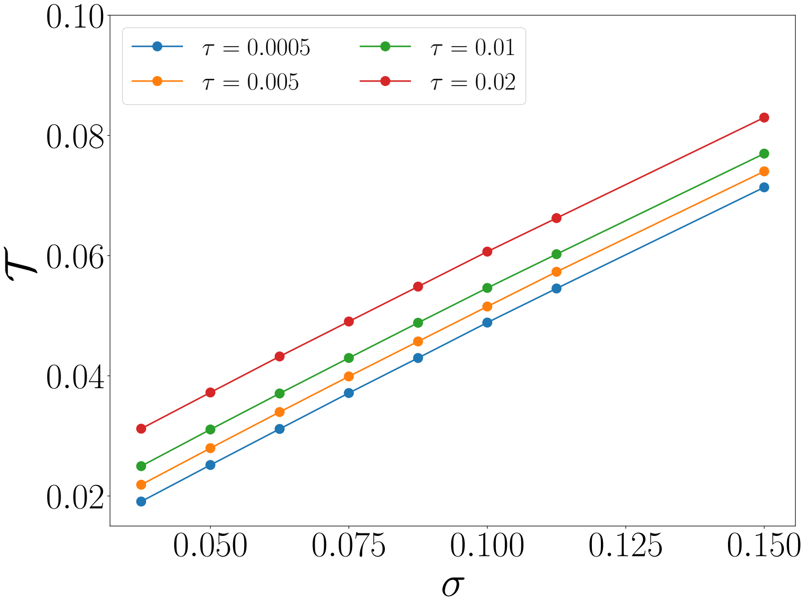

Figure 5.3: Bottom: $\mathcal{T}$ for a range of $\{\sigma, \tau\}$ computed over the profile displayed in Figure 5.2 outside the AH up to $r = 5M$ (the results do not change by a larger integration domain).

resolution for qualitatively informative results and contrasting them with results in GR. In particular, we see that positive/negative values of ϵ induce a (slight) merger phase delay/advance. This is consistent with expectations, where BHs in this theory have non-zero tidal effects, encoded to leading order in the Tidal Love Number $\kappa \propto \epsilon$ [54]. The binary behavior in the inspiral regime can be captured through a Post-Newtonian analysis which shows tidal effects induce a phase offset $\propto -\kappa$ (hence $\propto -\epsilon$) [89] (see also [155, 84]) for BHs with size comparable to M_S. Leading order Post-Newtonian estimates for the phase difference give $\approx \pm 5 \times 10^{-3}$ radians up to a common gravitational wave frequency ($Mf = 0.01$) for negative/positive values of ϵ in Fig. 5.5. Our obtained offsets –extrapolated to $\sigma \rightarrow 0$– are consistent with the sign, though about 200 times larger (for a related study in Einstein-Scalar-Gauss Bonnet theory see [66]).

The BHs coalesce, and the resulting peak strain is comparatively similar to that in GR, and no significant further structure is induced in the multipolar decomposition of the waveforms, confirming that the solution stays within the EFT regime. Furthermore, the peak amplitude obtained when the simulation starts with the BHs are initially closer, so that the merger takes place in only $\approx 200M$, agrees with the case taking $\approx 2000M$

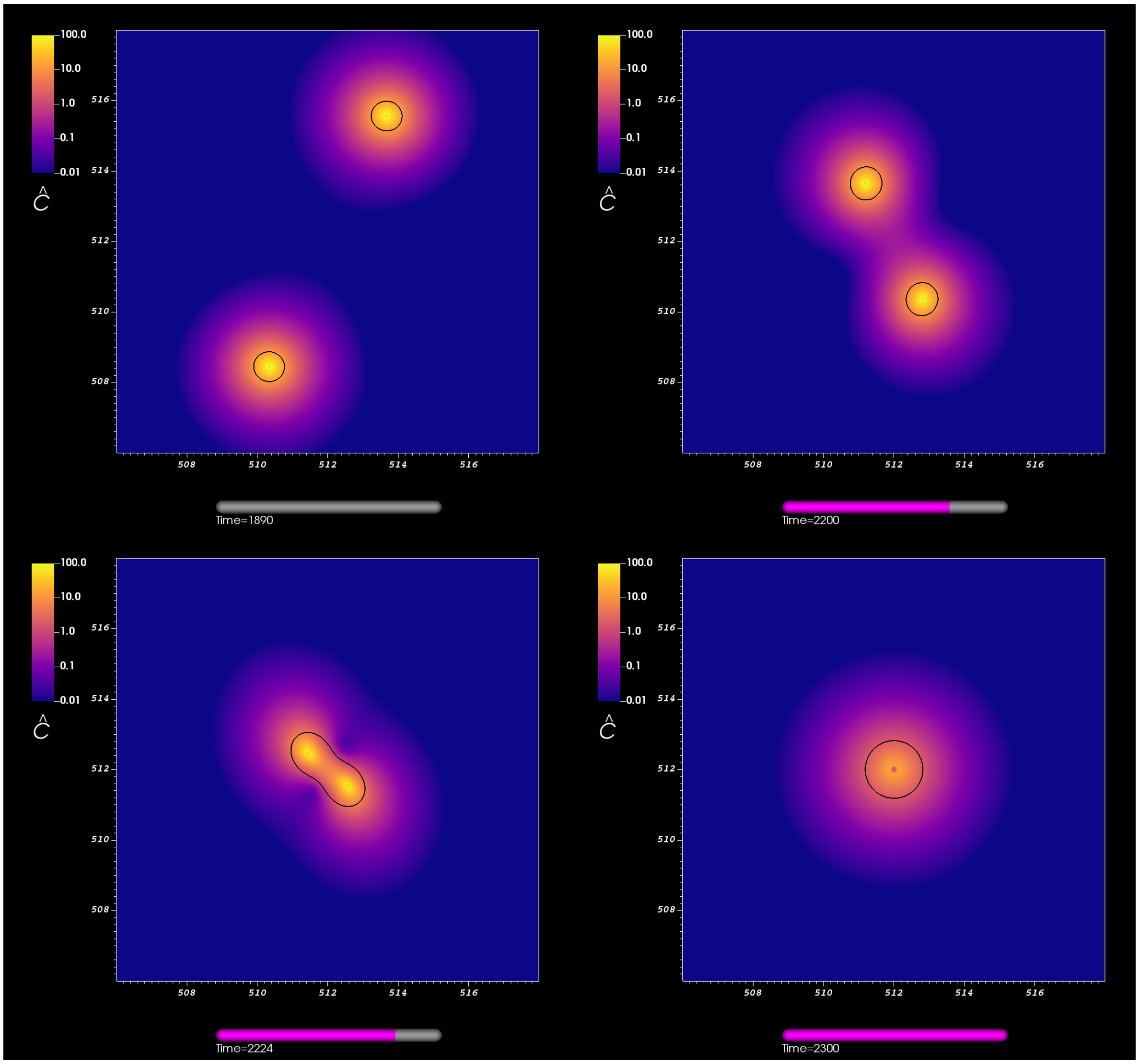

Figure 5.4: Snapshots of the value of $\hat{\mathcal{C}}$ on the equatorial plane for the EFT theory with $\epsilon = 10^{-5}$, $\sigma = 0.0625$ and $\tau = 0.005$. The black shapes surrounding each black hole's center indicate the apparent horizons' approximate location.

to less than 1% relative difference. Moreover, since the merger gives rise to a BH with roughly twice the individual masses, corrections are reduced by $\approx 2^{-6}$. Thus the final BH is closer to a GR solution than the initial ones. This can be appreciated as well in Figure 5.4, where $\hat{\mathcal{C}}$ is larger for the individual BHs than it is for the BH remnant.

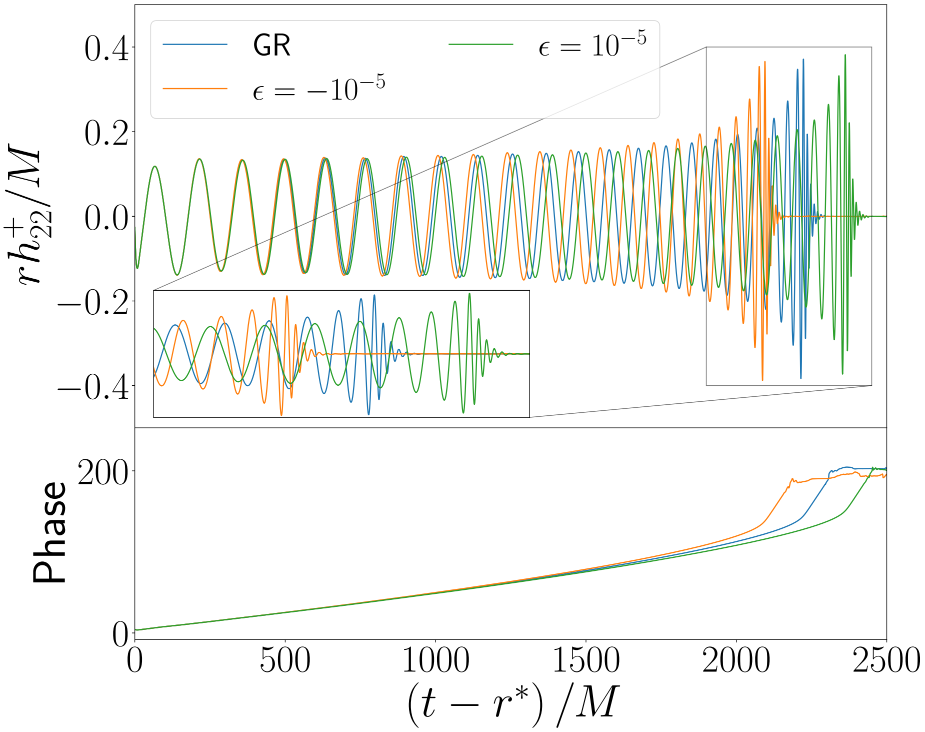

Figure 5.5: Gravitational waves in GR and in the EFT theory ($\epsilon = \pm 10^{-5}$) with $\sigma = 0.0625, \tau = 0.005$. Top: $(\ell, m) = (2, 2)$ mode of the $+$ polarization h_{22}^{+}, extrapolated to null infinity as a function of the retarded time $u = t - r^*$, where r^* is the tortoise radius. Bottom: gravitational wave phase of h_{22}.

After the peak amplitude, the system settles quickly into a stationary BH solution. This transition is described by an exponential, oscillatory behavior described by quasi-normal modes (QNM). While QNM spectra have only been computed for slowly rotating BHs in this theory [54, 51], the departure observed in decay rates is consistent with extrapolation to higher spin values, though this is not the case in the oscillatory frequency. We note, however, that the extracted values for the case in GR have relative errors $\approx 0.1\%$; since GR corrections to the QNMs in the case studied here are subleading by an order of magnitude such potential discrepancy can be attributed to a need for even higher accuracy to capture them sharply.

Also, as the system approaches its stationary final state, we confirm it is axisymmetric. Such symmetry is expected in stationary BH solutions in EFTs of gravity [117]. To assess the axisymmetry of the final state, we evaluate two scalar quantities, namely the conformal

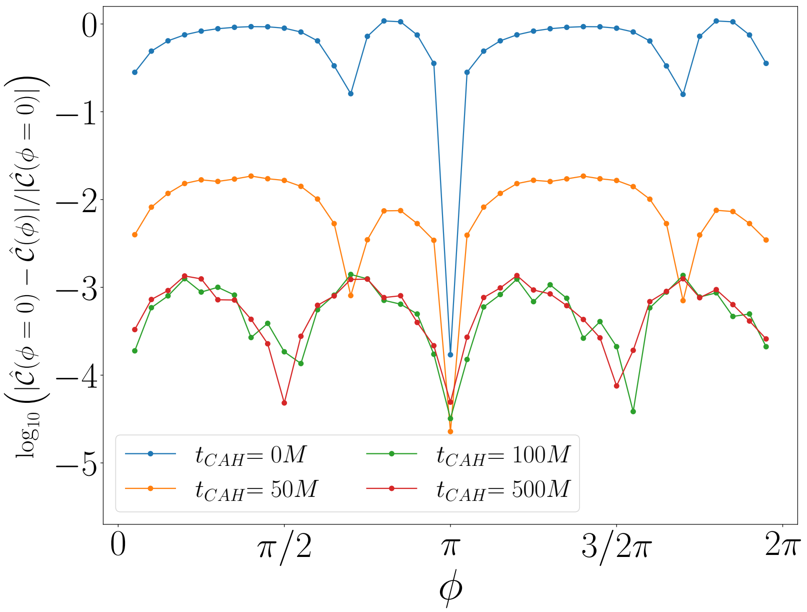

Figure 5.6: Relative difference between $\hat{\mathcal{C}}(\phi)$ and $\hat{\mathcal{C}}(\phi = 0)$ evaluated at different azimuthal angles ϕ at the equator of the common AH formed after the merger at different times starting from such time at which a first common AH is found ($t_{CAH} = 0$). The configuration evolves towards an axisymmetric state.

factor χ on the t = const slices and $\hat{\mathcal{C}}$, at the intersection of the common AH with the equatorial plane and compute their relative differences with the (arbitrary) point $\phi = 0$, where ϕ is the usual azimuthal angle on the AH two-sphere; (see figures 5.6,5.7). As time progresses, such difference reduces significantly indicating a high degree of axisymmetry, consistent with the result of [117].

Last, note that the difference in the innermost stable circular orbit frequency between slowly rotating BHs in this theory and GR goes as $\delta\Omega_{\rm ISCO} \propto -\epsilon$. Thus, extrapolating this observation to general spins, and following the successful strategy to estimate the final (dimensionless) spin in BH coalescence in GR [43], one can argue that the final BH spin should be higher/(lower) for positive/(negative) values of ϵ as the final 'plunge' takes place with a higher/(lower) contribution of orbital angular momentum to the final BH. Cautioning that higher accuracy is required to confirm this expectation, our results are consistent with it.

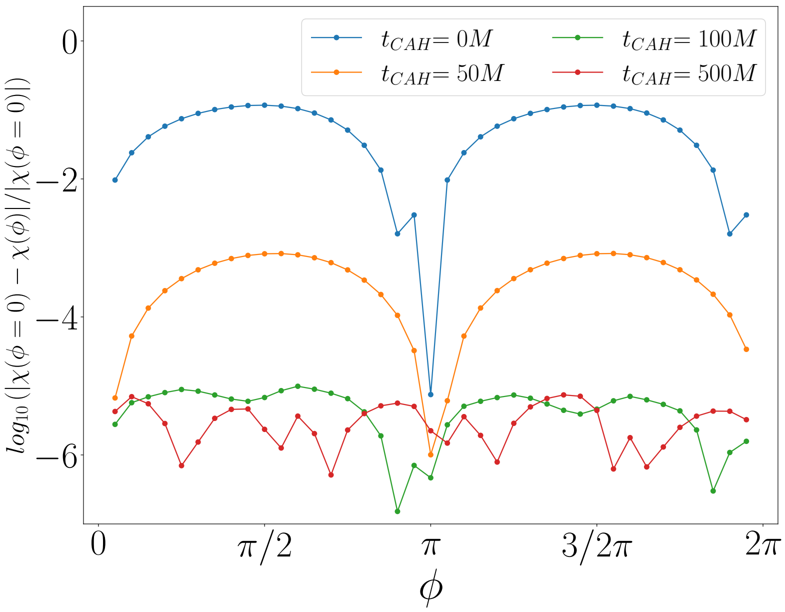

Figure 5.7: Relative difference between the conformal factor $\chi(\phi)$ and $\chi(\phi = 0)$ as in Fig. 5.6. As time progresses a clear trend to axisymmetry is evident.

5.9 Impact of ad-hoc parameters

The parameters $\{\sigma, \tau\}$ appearing in the evolution equation for $\hat{\mathcal{C}}$ (5.8) are ad-hoc and define a scale.[9] Their role is to control scales shorter (heavier) than theirs, thus controlling the mathematical pathologies discussed. Naturally, the solution obtained for any set of values of such parameters can depend on their values. Such dependency will be strong if the solution displays a significant cascade to the UV, as in such case the system tends to abandon the EFT regime, and the *Fixing* strategy would force it to remain in it, damping energy in high-frequency modes. On the other hand, such dependency could be mild, not affecting the solution's behavior qualitatively but might introduce minor variations in quantitative characteristics. Whenever the *Fixing* strategy is employed (and arguably any other strategy) to address the mathematical shortcomings, assessing the solution's dependency on whichever strategy is paramount. In our case, it means examining dependency on $\{\sigma, \tau\}$.

By varying their values, we do identify a mild dependency on them, which we trace

---

[9] The analogous parameters appearing in Israel-Stewart formulations of relativistic viscous hydrodynamics can be related to transport coefficients of the underlying microscopic theory.

back to the role of the advection vector β^i and the terms it multiplies in (5.8), and not to a UV cascade taking place outside the BH(s). These terms, which were introduced to ensure advection into the BH, also affect the tracking, to a small degree, as we have seen. In particular, the difference between $\hat{\mathcal{C}}$ and $\mathcal{C}$ is linear, and increasing with σ especially where the curvature is strong. This difference, although small, over long times affects somewhat physical quantities or observables. One can, nevertheless, extrapolate such difference to values of $\tau, \sigma \to 0$ (see also [33]). For instance, as displayed in figure 5.8 we perform such extrapolation to obtain the time of peak amplitude of the strain for $\sigma \to 0$. This figure shows that such quantity depends linearly with σ, and the extrapolated time delay for the peak amplitude is $\approx 30M$. This extrapolation is further supported by the weak dependence on τ and the fact that a linear behavior with σ is present in our toy model until very small values of this parameter.

Furthermore, we can monitor the difference between values of $\hat{\mathcal{C}}$, or $\mathcal{C}$, upon varying σ as time proceeds. Figure 5.9 illustrates the observed behavior for the single boosted BH case, illustrating that errors related to the value of σ accumulate slowly. Indeed, it would take about $t \approx 10^6 M$ for the relative error for Kretschmann scalar with $\sigma = 0.1$ and 0.05 to be $\mathcal{O}(1)$.

5.10 Choice of fixing equation

As was mentioned in the last section, we attribute the dependence of the solution on the fixing parameters $\{\sigma, \tau\}$ to the contribution of the terms in the fixing equation (5.8) (which in this section we will refer to as the "Advection" system) that contain factors of β^i. Analyzing (5.8) for a time-independent solution can help see why that is the case. In that case 5.8 reduces to,

$$\beta^i \beta^j \partial_{ij} \hat{\mathcal{C}} - \frac{\tau}{\sigma} \beta^i \partial_i \hat{\mathcal{C}} = \frac{1}{\sigma} \left(\mathcal{C} - \hat{\mathcal{C}} \right). \tag{5.9}$$

If we were able to perfectly track the time-independent solution of the original system, let us call it $\mathcal{C}_0$, into a time-independent solution of our new variable, let us call it $\hat{\mathcal{C}}_0$, this would imply $\hat{\mathcal{C}}_0 = \mathcal{C}_0$, and the fixing equation would further simplify to,

$$\sigma \beta^i \beta^j \partial_{ij} \mathcal{C}_0 - \tau \beta^i \partial_i \mathcal{C}_0 = 0. \tag{5.10}$$

However, the time-independent solution $\mathcal{C}_0$ of the original system need not satisfy (5.10) (and does not for the spherically symmetric BH). This brings us to a contradiction, and

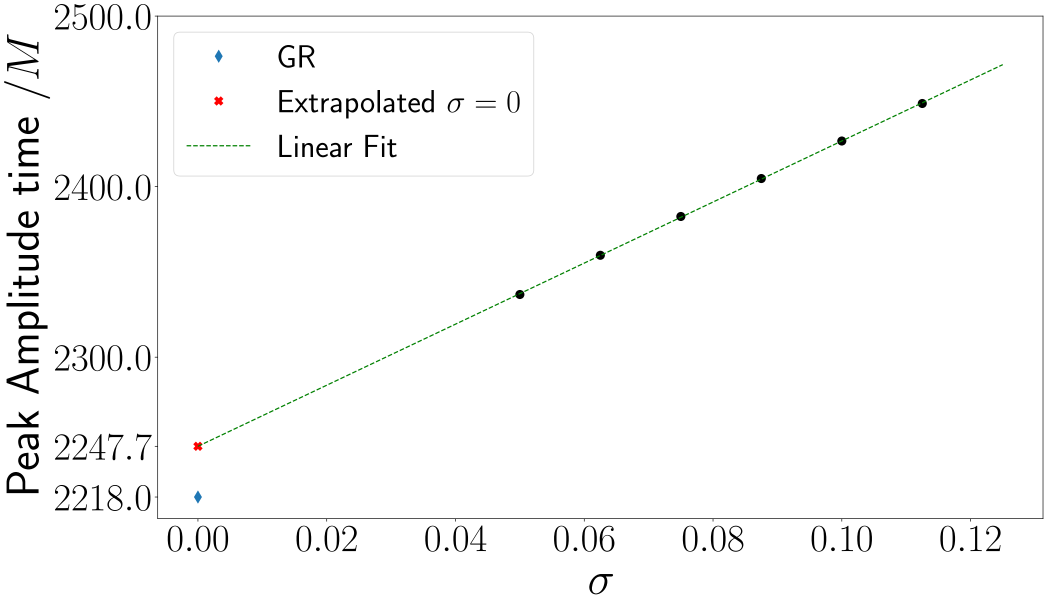

Figure 5.8: Retarded time for peak amplitude of h_{22} of BH binary mergers for a fixed value of $\tau = 0.005$ and several values of σ (black dots). The dashed green line is a linear fit to the data given by the black dots. The red cross is a linear extrapolation for the peak amplitude time for $\sigma = 0$, which has a value of $t^{peak}_{\sigma\to 0} = 2247.7M$, while the blue diamond is the peak amplitude time for the GR case and has a value of $t^{peak}_{GR} = 2218.0M$.

hence we conclude that $\hat{\mathcal{C}}_0 \neq \mathcal{C}_0$. The degree to which $\hat{\mathcal{C}}_0$ differs from $\mathcal{C}_0$ is determined by

$$\sigma\beta^i\beta^j\partial_{ij}\hat{\mathcal{C}}_0 - \tau\beta^i\partial_i\hat{\mathcal{C}}_0 = \mathcal{C}_0 - \hat{\mathcal{C}}_0. \tag{5.11}$$

The difference between $\mathcal{C}$ and $\hat{\mathcal{C}}$ can be reduced by decreasing the value of σ and τ. However, as we discussed earlier, there is a limit two how small these parameters can be before the simulations become unstable. A clear solution to this shortcoming would then be to get rid of all the β^i proportional terms in (5.8) and evolve with the following fixing equation,

$$\partial_t^2\hat{\mathcal{C}} = \frac{1}{\sigma}\left(\mathcal{C} - \hat{\mathcal{C}} - \tau\partial_t\hat{\mathcal{C}}\right), \tag{5.12}$$

which we shall call the "time derivatives" system. However, we found that equation (5.12), lacking the advective capabilities of our choice of equation (5.8), was not able to control

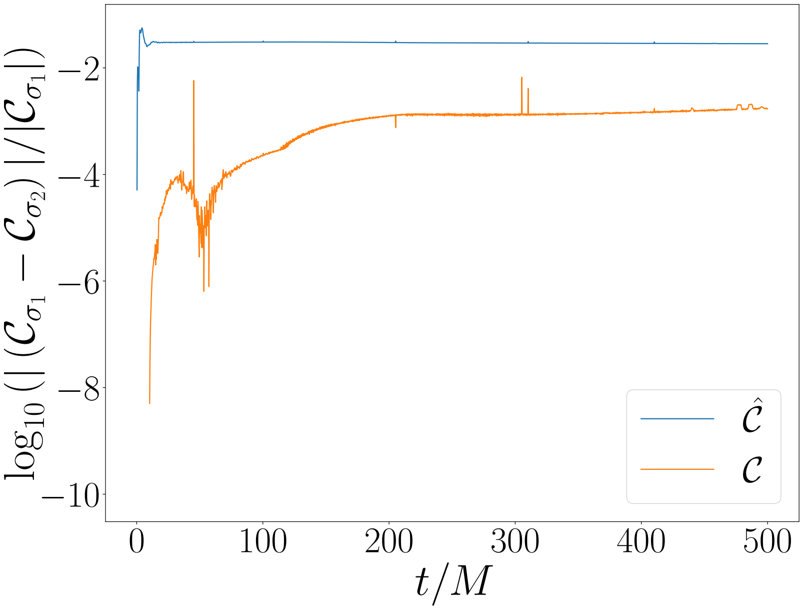

Figure 5.9: Relative difference between the maximum value of $\hat{\mathcal{C}}$ ($\mathcal{C}$) on the AH for single boosted BHs for two values of σ ($\sigma_1 = 0.05$ and $\sigma_2 = 0.1$).

the appearance of spurious noise in the vicinity of the excision region, which ultimately grows out of proportion and the simulations crash. We can, however, point out that in the short time before these simulations crash, the difference between $\hat{\mathcal{C}}$ and $\mathcal{C}$ is considerably smaller than the advective case.

Besides the two previously discussed fixing equations, we considered a third choice where the $\hat{\mathcal{C}}$ is evolved using a $\Box$ operator of the spacetime, namely,

$$-\sigma\Box\hat{\mathcal{C}} = -\tau\partial_t\hat{\mathcal{C}} - (\hat{\mathcal{C}} - \mathcal{C}). \tag{5.13}$$

This system, which we will refer to as the "Box" system, proves to render the system stable in a wide range of the fixing parameters $\{\sigma, \tau\}$, the structure provided by the $\Box$ operator forces the noise generated in the excision region to fall deeper into the BH, where $\epsilon \to 0$. However, the same shortcomings discovered for the time-independent solution in the advection system affect this equation. For the available values of $\{\sigma, \tau\}$ the difference between $\hat{\mathcal{C}}$ and $\mathcal{C}$ tend to be considerably larger than the ones obtained for the advection system. Figure 5.10 shows the Tracking measure $\mathcal{T}$ for the three different choices of fixing equation as a function of time in the scenario of single boosted BHs. The simulations were

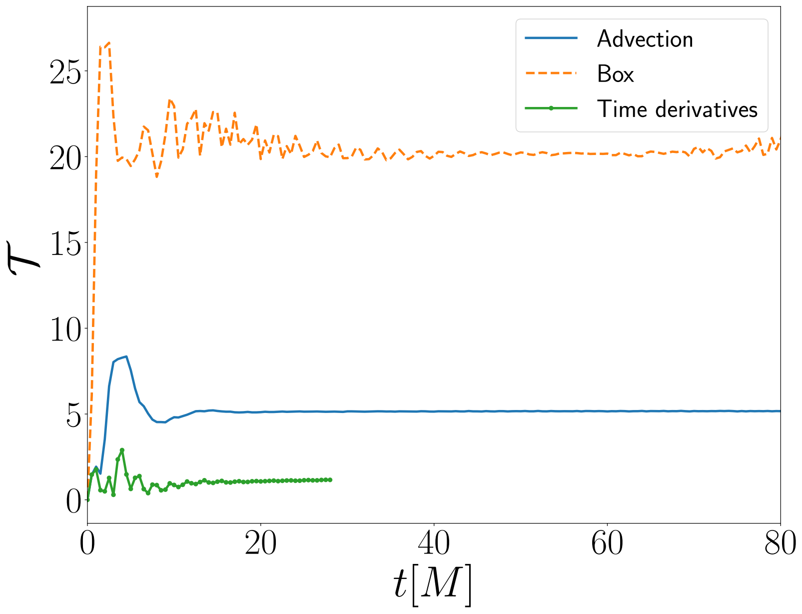

Figure 5.10: Tracking measure $\mathcal{T}$ as a function of time for the three different choices of fixing equation. For the three simulations, the values $\sigma = 0.1$, $\tau = 0.005$ and $\epsilon = 10^{-5}$.

run with the same parameters, $\sigma = 0.1$, $\tau = 0.005$, and $\epsilon = 10^{-5}$. In green dotted lines, we show the value $\mathcal{T}$ for the "time derivatives" system (5.12), even though it displays the better Tracking ($\approx 1\%$) out of the three choices, the simulation becomes unstable at $t \approx 30M$. The value of $\mathcal{T}$ for the "Box" system (5.13) is displayed in orange dotted lines, giving a tracking error of $\approx 20\%$. Lastly, on blue lines, we show the value of $\mathcal{T}$ for the "Advection" system (5.8), the tracking error is $\approx 5\%$ and hence bigger than in the "time derivatives" case, but this system remains stable through the evolution. From the three choices of fixing equation that we presented, the best choice is the "Advection" system, and for this reason we chose it as the system to carry out the binary BH scenario.

Having understood the different limitations of the studied fixing equations, we can now consider possible improvements. The main issue with the choices of equations that give rise to stable evolutions, is that they can change physics at scales relevant to the dynamics of the problem. As we saw in Figure 5.2, there are small but non-negligible changes in the solutions close to the BH horizons. Having this in mind, let us then see what equation should $\hat{\mathcal{C}}$ satisfy to not alter the physics. From Bianchi's identity, it can be shown that the Weyl tensor in vacuum (in our case $R_{ab} = 0 + \mathcal{O}(\epsilon)$) satisfies the following wave-like equation,

$$\Box W_{abcd} = -W_{ab}{}^{ef}W_{efcd} + 2W^{e}{}_{ac}{}^{f}W_{ebdf} - 2W_{ead}{}^{f}W^{e}{}_{bcf}. \tag{5.14}$$

Contracting equation (5.14) with another Weyl would give rise to the following equation for $\mathcal{C}$.

$$\Box\mathcal{C} = 2\,W^{abcd}\big(4\,W^{e}{}_{ac}{}^{f}\,W_{ebdf} - W_{ab}{}^{ef}W_{efcd}\big) + 2\,\nabla^{e}W^{abcd}\nabla_{e}W_{abcd}. \tag{5.15}$$

With this equation in hand, it is easy to see the pieces "missing" on the right-hand side of equation (5.13), and incorporating such terms in that equation with result in the fixing equation,

$$\begin{aligned} -\sigma\Box\hat{\mathcal{C}} =& -\sigma\left(2\,W^{abcd}\big(4\,W^{e}{}_{ac}{}^{f}\,W_{ebdf} - W_{ab}{}^{ef}W_{efcd}\big) + 2\,\nabla^{e}W^{abcd}\nabla_{e}W_{abcd}\right)\\ &- \tau\partial_t\hat{\mathcal{C}} - (\hat{\mathcal{C}} - \mathcal{C}). \end{aligned} \tag{5.16}$$

If we carried out the same analysis for the time-independent solutions we carried out for the advection system, we would see that under the assumption that $\hat{\mathcal{C}}_0 = \mathcal{C}_0$, the requirement on $\mathcal{C}_0$ would be to satisfy the time-independent version of equation(5.14), which is physical, unlike (5.10).

Even though such implementation is achievable, it is not practical and potentially problematic. Equation (5.16) contains terms that are nonlinear in second and third-order derivatives of the metric. Being able to eliminate higher than second-order derivatives of the metric easily was the main motivation for using the $\hat{\mathcal{C}}$ as the new dynamical variable.

Noticing that (5.14) contains on its right-hand side only factors of the Weyl tensor and no covariant derivatives, the following alternative fixed system becomes appealing,

$$G_{ab} = \epsilon\Big(4\,\hat{\mathcal{C}}\,\hat{W}_{a}{}^{cde}\,\hat{W}_{bcde} - \frac{g_{ab}}{2}\,\hat{\mathcal{C}}^2 + 8\,\hat{W}_{a}{}^{c}{}_{b}{}^{d}\,\nabla_c\nabla_d\hat{\mathcal{C}}\Big), \tag{5.17}$$

$$\begin{aligned} -\sigma\Box\hat{W}_{abcd} =& -\sigma\left(-\hat{W}_{ab}{}^{ef}\hat{W}_{efcd} + 2\hat{W}^{e}{}_{ac}{}^{f}\hat{W}_{ebdf} - 2\hat{W}_{ead}{}^{f}\hat{W}^{e}{}_{bcf}\right)\\ &-\tau\partial_t\hat{W}_{abcd} - \left(\hat{W}_{abcd} - W_{abcd}\right), \end{aligned} \tag{5.18}$$

where $\hat{W}_{abcd}$ are the new variables introduced to the system, and $\hat{\mathcal{C}} \equiv \hat{W}_{abcd}\hat{W}^{abcd}$. This system possesses another advantage besides the fact that it would bypass the issues raised for the previously discussed alternatives. In this system, the first two terms of (5.17) no longer belong to the principal part, while for systems using only $\hat{\mathcal{C}}$ as the sole new dynamical (see (5.7)), the first of these terms still contains second derivatives of the metric. There is the obvious disadvantage that instead of having to evolve one extra variable, namely $\hat{\mathcal{C}}$, the evolution of this system involves evolving ten (the Weyl tensor has only ten independent components) new variables. One can as well, decompose the Weyl tensor into its Electric and Magnetic components E_{ij} and B_{ij} and write a system in terms of new dynamical variables $\hat{E}_{ij}$ and $\hat{B}_{ij}$, which also evolve through wave-like equations. We do not treat this case in this thesis since it is still a work in progress. It is relevant to point out that this last choice of fixing equation is directly applicable to the dimension-six operator case as well, while the system with only $\hat{\mathcal{C}}$ was highly tailored to the dimension-eight operator EFT field equations.

5.11 Discussion

We have demonstrated the ability of the *Fixing* approach to enable studies beyond GR theories. This approach, in particular, provides a practical way to explore phenomenology in the highly nonlinear and dynamical regime of compact binary mergers. Especially relevant is that it enables assessing whether the solution for cases of interest remains in the EFT regime and the impact of corrections in gravitational wave observations. From this first analysis, we conclude the solution remains in this regime for comparable mass, quasicircular mergers in the observable region, i.e., the BH(s) exterior. Thus, much like in the case of GR, a strong UV energy flow takes place inside the horizon but not in the outside region, staying within the valid EFT regime. While in the current work we have focused on a specific theory and scale, our choice was motivated by stress-testing the approach with highly demanding challenges –brought by higher than second-order derivatives and in the context of BH collisions. However, the underlying strategy is also applicable beyond GR theories with second-order equations that can induce a change of character in the equation of motion (e.g., [161, 93]). We note that for a particular class of nonlinear theories (with second-order equations of motion), consistent nonlinear studies have been presented [66, 19, 32]. However, they required significant supporting theoretical efforts to identify appropriate gauge conditions, and merging BH solutions have been obtained up to some maximum coupling value. Otherwise, mathematical pathologies arise. Our approach, in principle, can provide a way to explore beyond such coupling and, in general, study beyond GR theories self-consistently. Of course, the practical application of the approach described here should be mindful of checking results upon variations of ad-hoc parameters to ensure, given a coupling length, scales are sufficiently resolved.

Chapter 6

Gravitational collapse in Quadratic Gravity

6.1 Introduction

In the previous chapters, we focused on an EFT extension to GR built using dimension-8 operators in the effective action. In the absence of matter, for example, in a binary merger of BHs, dimension-six and dimension-eight operators are the leading and next-to-leading order corrections. When matter is present, the leading order curvature operators in the EFT construction are dimension-four operators (R^2, $R_{ab}R^{ab}$ and $R_{abcd}R^{abcd}$). In this context, neutron star (NS) binaries become one of the most relevant scenarios. Modifications to GR may not only affect the dynamics during the inspiral and merger phases, but the behavior and signatures of the merger remnant could also be highly altered. Given that these theories are constructed from powers of curvature invariants, it is natural that the effects of the modifications grow with the curvature, and small black holes (BHs) would give rise to the strongest effects. The merger of binary NSs [3] presents an ideal scenario for the formation of some of the smallest astrophysical black holes, with masses of approximately $3M_{\odot}$. The post-merger dynamics of such an object could be one of the best windows to observe deviations from GR [80]. Exotic formation channels for smaller BHs could result in scenarios where such BHs interact with NSs in regimes of large spacetime curvature, where significant corrections could arise from these types of modifications to GR [1].

The theory built from these four-dimensional operators is commonly called Quadratic

---

[1] See [78] for a study of a NS being consumed by a much less massive BH residing inside the star.

Gravity [174], and there has been recent work performing fully nonlinear numerical simulations in spherical symmetry and very recently in the BH binary merger scenario [112, 113]. However, these works have focused on the vacuum scenario, most specifically in the Ricci-flat case, which, from the perspective of EFT, solutions and dynamics should be indistinguishable from GR.

In this chapter, we explore the dynamics of this dimension-four operator EFT extension to GR in the presence of matter, where modifications should arise. For simplicity, the considered system has spherical symmetry, and we evolve the collapse of a massless minimally coupled scalar field into a BH. There are several objectives to this work. First, we want to present an alternative approach to that presented in [112, 113], as well as incorporate matter into the system to study gravitational collapse. The second one is to study how the modifying terms affect the dynamics of the system. And finally, to determine in what region of the parameter space the system stays within the EFT description, simulations are well-behaved, and when predictions can be trusted.

This chapter is structured as follows: In section 6.2, the four-dimensional operator EFT, its action, and its corresponding field equations are presented. In section 6.3, the evolution and constraint equations are presented, and the "Order Reduction" procedure is introduced to deal with the higher derivatives in such equations. Section 6.4 contains detailed information about the target problem and setup, including the prescription for initial data, the numerical implementation, and relevant monitoring quantities. The paper's main results are presented in Section 6.5. A brief discussion on the observed results and future outlook can be found in Section 6.6. The appendices contain additional information regarding the convergence test and constraint violations observed in the simulations. The following notation is adopted: The beginning of the Latin alphabet $(a, b, c, d, ...)$ will be used to denote full spacetime indices, while the Latin letters $(i, j, k, l...)$ will be used to indicate spatial ones. The $(-, +, +, +)$ signature is used, and the speed of light is set to $c = 1$.

6.2 Leading order EFT, non vacuum equations

The leading order terms in an EFT extension to GR, which introduce no new light degrees of freedom and satisfy parity symmetry, are the ones built with the dimension-four operator curvature invariants R^2, $R_{ab}R^{ab}$ and $R_{abcd}R^{abcd}$. Using the fact that the Gauss-Bonnet invariant is topological in four spacetime dimensions, one can exclude the Riemann-squared term from the effective action. The effective action can be written as:

$$S_{\text{eff}} = \frac{1}{16\pi G}\int d^4x\sqrt{-g}\left(R - \frac{a_1}{\Lambda^2}R_{ab}R^{ab} + \frac{a_2}{\Lambda^2}R^2 + \cdots\right), \tag{6.1}$$

where a_1 and a_2 are dimensionless coefficients and Λ has units of inverse length and determines the cut-off of the EFT. Notice that in the vacuum case, since $R_{ab} = 0 + \mathcal{O}(1/\Lambda^2)$, then these terms would be pushed to higher orders of the perturbative scheme, and six-dimensional operators would dominate. This work includes matter in the form of a minimally coupled scalar field, so these terms are the leading order operators.

Upon variation of this action, the following field equations are obtained,

$$\begin{aligned} &R_{ab} - \frac{1}{2}g_{ab}R + \frac{1}{2}\epsilon_1 R_{cd}R^{cd}g_{ab} + 2\epsilon_2 R_{ab}R - \frac{1}{2}\epsilon_2 g_{ab}R^2 - 2\epsilon_1 R^{cd}R_{acbd} \\ &+ (\epsilon_1 - 2\epsilon_2)\nabla_b\nabla_a R - \epsilon_1\nabla^2 R_{ab} - g_{ab}(\frac{1}{2}\epsilon_1 - 2\epsilon_2)\nabla_c\nabla^c R = 8\pi T_{ab}, \end{aligned} \tag{6.2}$$

$$\nabla^a T_{ab} = 0, \tag{6.3}$$

where $\epsilon_1 = a_1/\Lambda^2$, $\epsilon_2 = a_2/\Lambda^2$ (which will occasionally be called couplings) and T_{ab} is the usual energy-momentum tensor defined as,

$$T_{ab} = \nabla_a\phi\nabla_b\phi - \frac{1}{2}g_{ab}\nabla_c\phi\nabla^c\phi. \tag{6.4}$$

For convenience equation (6.2) will expressed as,

$$R_{ab} - \frac{1}{2}g_{ab}R = 8\pi T_{ab} + M_{ab}, \tag{6.5}$$

where now M_{ab} encompasses all modifications to the equations. The M_{ab} tensor contains up to 4th-order derivatives of the metric; In general, these sorts of modifications make the task of formulating the problem as well-posed [109, 163] a challenging one, if not an impossible one with the standard techniques. [2]

---

[2] Remarkably, this theory possesses a formulation that allows to define a well-posed initial value problem [147]. However, as we shall describe in the next section, there exists some tension between such formulation and the EFT framework.

6.3 Evolution equations and constraints

Before addressing the issues raised at the end of the previous section, the equations will be first expressed in a formulation that, in the absence of correcting terms, renders the problem well-posed. To this end, the Generalized Harmonic formulation [91, 157, 135] that is written in terms of the usual 3+1 variables [41] is adopted. Under this formulation, the full set of evolution equations and constraints are expressed as,

$$\partial_\perp \gamma_{ij} = - 2\alpha K_{ij}, \tag{6.6a}$$

$$\begin{aligned}\partial_\perp K_{ij} =& \alpha \left[R^{(3)}_{ij} - 2K_{ik}K^k_j - \widetilde{\pi} K_{ij}\right] - D_i D_j \alpha - \alpha D_{(i}\mathcal{C}_{j)} - \kappa\alpha\gamma_{ij}\mathcal{C}_T/2 \\ & - 8\pi G\alpha\left[S_{ij} - \gamma_{ij}(S-\rho)/2\right] - \alpha\left[S^M_{ij} - \gamma_{ij}(S^M - \rho^M)/2\right],\end{aligned} \tag{6.6b}$$

$$\partial_\perp \alpha = \alpha^2 \widetilde{\pi} - \alpha^2 H_T, \tag{6.6c}$$

$$\partial_t \beta^i = \beta^j \bar{D}_j \beta^i + \alpha^2 \rho^i - \alpha D^i \alpha + \alpha^2 H^i, \tag{6.6d}$$

$$\partial_\perp \widetilde{\pi} = - \alpha K_{ij} K^{ij} + D_i D^i \alpha + \mathcal{C}^i D_i \alpha - \kappa\alpha\mathcal{C}_T/2 - 4\pi G\alpha(\rho + S) - \frac{\alpha}{2}(\rho^M + S^M), \tag{6.6e}$$

$$\begin{aligned}\partial_\perp \rho^i =& \gamma^{k\ell}\bar{D}_k \bar{D}_\ell \beta^i + \alpha D^i \widetilde{\pi} - \widetilde{\pi} D^i \alpha - 2K^{ij} D_j \alpha + 2\alpha K^{jk}\Delta\Gamma^i_{jk} + \kappa\alpha\mathcal{C}^i \\ & - 16\pi G\alpha j^i - 2\alpha j^i_M,\end{aligned} \tag{6.6f}$$

with the constraints,

$$\mathcal{C}_T \equiv \widetilde{\pi} + K, \tag{6.7a}$$

$$\mathcal{C}^i \equiv -\rho^i + \Delta\Gamma^i_{jk}\gamma^{jk}, \tag{6.7b}$$

$$\mathcal{H} \equiv K^2 - K_{ij}K^{ij} + R - 16\pi G\rho - 2\epsilon\rho^M, \tag{6.7c}$$

$$\mathcal{M}_i \equiv D_j K^j_i - D_i K - 8\pi G j_i - \epsilon j^M_i, \tag{6.7d}$$

where $K \equiv \gamma^{ij}K_{ij}$, D_i and $\bar{D}_i$ are the covariant derivatives for the three-metric γ_{ij} and the background 3-metric $\bar{\gamma}_{ij}$ respectively. The derivative operator $\partial_\perp$ is defined as $\partial_\perp = \partial_t - \mathcal{L}_\beta$, where $\mathcal{L}_\beta$ is the Lie derivative along the shift vector β^i. Defining $\Delta\Gamma^i_{jk} :=^{(3)} \Gamma^i_{jk} -^{(3)} \bar{\Gamma}^i{}_{jk}$, where these are the Christoffel symbols for the induced metric and background metric (flat in spherical coordinates) respectively. Defining also $H_T := H^a n_a$, where n_a is the normal vector to the spatial hypersurfaces defined by the spacetime foliation. The new dynamical variables $\widetilde{\pi}$ and ρ^i are introduced through equations (6.6c-6.6d) to make the system (ignoring the extensions to gravity) first order in time derivatives. S_{ij}, S, ρ and j^i are the matter variables constructed from the energy-momentum tensor T_{ab} as,

$S_{ij} = P^a_i P^b_j T_{ab}$, its trace $S = \gamma^{ij} S_{ij}$, $\rho = n_a n_b T^{ab}$, and $j^i = -P^{ia} n^b T_{ab}$. Where P^{ia} is a projection tensor to the spatial hypersurface. Here the definitions for S^M_{ij} ,S^M, ρ^M and j^i_M are analogous to the ones for the matter sources, but instead of using T_{ab}, we use M_{ab}.

Let us now analyze the structure of the terms introduced by M_{ab}, which modify Einstein's equations. These terms contain up to 4th-order time and spatial derivatives of metric components. In addition, they contain nonlinear combinations of derivatives that would make the usual hyperbolicity analysis [106] inapplicable. Furthermore, the constraint equations (6.7c)-(6.7d) contain time derivatives, which are not present in the Hamiltonian and Momentum constraints in GR. These sorts of issues are not uncommon when dealing with modified gravity theories, even in Horndeski theories, which are second order in derivatives and incorporate a non-minimally coupled scalar field, suffer from pathologies that can render the problem of interest ill-posed [161, 29, 86, 177]. In those cases, after significant theoretical efforts, appropriate new gauges were formulated [129, 128] that ameliorate these issues to the point where nonlinear studies of compact binary mergers are possible [81, 66, 19, 79] for some regime of small coupling values. In the case of higher derivative extensions to GR, fully nonlinear evolution has been performed [58, 59] for an eight-dimensional operator EFT extension through controlling pathological higher frequencies via a "fixing" method [56, 16, 131, 93] leaving the long wavelength physics unaltered.

Coming back to this paper's theory of interest works like [112, 113] tackle these issues by re-writing the theory following the work of Noakes [147], in which the Ricci scalar and the traceless part of the Ricci tensor can be elevated to massive spin-0 and spin-2 fields and are evolved with equations derived directly from the field equations of the theory. With this prescription, they can verify numerical stability in the Ricci-flat subsector and confirm that it is indistinguishable from GR. However, an opposing view to this method can be formed from the perspective of EFT. The extra modes that this theory introduces and that this approach makes explicit have masses that are above the cut-off scale of the EFT; hence the dynamics of these modes should be irrelevant in the EFT regime [114] [3]. Furthermore, depending on the signs and values of ϵ_1 and ϵ_2, these massive degrees of freedom can become tachyonic, which would take them outside the regime of applicability of the EFT. In contrast, this work, taking this intuition from EFT, will actively remove these extra degrees of freedom by eliminating the higher order time derivatives in the field equations via an *Order Reduction* [173] procedure [4]. Proceeding as done in [59] (see Section II-C of that work for more details), one can use the evolution and constraint equations to

---

[3] See [42] for a similar argument on the massive degrees of freedom in six-dimensional operators EFT.

[4] This *Order Reduction* approach is not to be confused with the *Perturbative Order Reduction* techniques used in [149, 148], where order-reducing refers to replacing some problematic terms and solving them iteratively/perturbatively.

0th order in ϵ_1 and ϵ_2 to find expressions of higher order time and spatial derivatives of the metric components in terms of lower order derivatives.

Schematically,

$$\frac{\partial^2 \boldsymbol{g}}{\partial t^2} = \boldsymbol{E}(\boldsymbol{g}, \partial_a \boldsymbol{g}, \partial_i^2 \boldsymbol{g}) + \epsilon \boldsymbol{M}(\boldsymbol{g}, \partial_a \boldsymbol{g}, \partial_a^2 \boldsymbol{g}, \partial_a^3 \boldsymbol{g}, \partial_a^4 \boldsymbol{g}) + \mathcal{O}(\epsilon^2), \tag{6.8}$$

represents the evolution system of equations (6.6) written in terms of the variables $\boldsymbol{g} = \{\gamma_{ij}, \alpha, \beta\}$. Here $\boldsymbol{E}$ represents the GR terms, which depend only up to first time derivatives and second spatial derivatives of $\boldsymbol{g}$. $\boldsymbol{M}$ represents the terms from the modified theory, which depend on up to fourth-order spacetime derivatives. Truncating (6.8) to order $\mathcal{O}(\epsilon^0)$

$$\frac{\partial^2 \boldsymbol{g}}{\partial t^2} = \boldsymbol{E}(\boldsymbol{g}, \partial_a \boldsymbol{g}, \partial_i^2 \boldsymbol{g}) + \mathcal{O}(\epsilon), \tag{6.9}$$

and taking derivatives of it gives expressions to higher than second-time derivatives of $\mathbf{g}$ in terms of lower order derivatives. This way (6.9) and its derivatives can be used to replace $\{\partial_a^2 \boldsymbol{g}, \partial_a^3 \boldsymbol{g}, \partial_a^4 \boldsymbol{g}\}$ in $\boldsymbol{M}$, in favor of $\widetilde{\boldsymbol{M}}$, to obtain redefinitions of (6.8) that are lower in time derivatives and valid to $\mathcal{O}(\epsilon)$,

$$\frac{\partial^2 \boldsymbol{g}}{\partial t^2} = \boldsymbol{E}(\boldsymbol{g}, \partial_a \boldsymbol{g}, \partial_i^2 \boldsymbol{g}) + \epsilon \widetilde{\boldsymbol{M}}(\boldsymbol{g}, \partial_a \boldsymbol{g}, \partial_a \partial_i \boldsymbol{g}, \partial_a \partial_i^2 \boldsymbol{g}, \partial_a \partial_i^3 \boldsymbol{g}) + \mathcal{O}(\epsilon^2), \tag{6.10}$$

This way, expressions for S^M_{ij}, S^M, ρ^M and j^i_M, let us call them $\widetilde{S^M_{ij}}$, $\widetilde{S^M}$, $\widetilde{\rho^M}$ and $\widetilde{j^i_M}$ can be obtained, which no longer contain higher derivatives in time and that are valid to $\mathcal{O}(\epsilon_1)$ and $\mathcal{O}(\epsilon_2)$. Once all undesired time derivatives are eliminated, the constraint equations, which now only contain spatial derivatives, can be used to find expressions for some (not all) higher spatial derivative derivatives of the metric components in terms of lower derivatives. In spherical symmetry, even though not all higher spatial derivatives expressions are available through an order reduction of the constraints, this procedure is enough to eliminate all higher-than-second spatial derivatives of the metric components. During this procedure, one introduces higher-order spatial derivatives (up to third) of the scalar field ϕ. In some way, all of the higher-order time and spatial derivatives of gravity variables have been traded for 3rd derivatives of the scalar field. This is seen easily by noticing that this reduction of order is equivalent to replacing R_{ab} and R through T_{ab} in all the ϵ proportional terms in (6.2). One could proceed as done in the previous chapters and control the higher frequencies via the *Fixing* approach. One of the objectives of this work is to explore under what circumstances the system is well-behaved after performing the order reduction without attempting to control the higher frequencies.

6.4 Target problem and setup

The objective is to study this theory and its equations in dynamical scenarios where non-linearities are important. We want to explore in which regime of the parameter space one can carry out numerical evolution without instabilities. If such instabilities do appear, the objective is to asses whether this happens within the regime of applicability of the EFT. To this end, we evolve spacetimes consisting of an initial in-falling scalar Gaussian profile, ultimately collapsing into a BH. This work will avoid treating critical collapse [61], mainly because the EFT is doomed to be outside of its regime of validity during such a process.

Reducing the problem to spherical symmetry, the line element for this problem is given by,

$$ds^2 = (-\alpha^2 + g_{rr}\beta^2)dt^2 + 2\beta g_{rr} dr dt + g_{rr} dr^2 + r^2 g_T (d\theta^2 + \sin^2\theta d\varphi^2), \tag{6.11}$$

where α is the lapse function, β is the radial component of the shift vector, and g_{rr} and g_T are the radial and angular components of the spatial metric γ_{ij}.

The equations that arise from this ansatz contain factors of r^{-p}, which lead to divergences at the origin $r = 0$. Using L'Hopital's rule, one can carefully redefine the equations at the origin to avoid these coordinate singularities. This technique is essential when dealing with the high p exponents that corrections to GR introduce.

6.4.1 Initial data

What determines whether the scalar field collapses into a BH or bounces back to infinity depends on the properties of the initial profile of the field. All of this will be encoded in the initial data prescribed. In this section, we discuss how we construct initial data consistent with the constraints of the modified theory.

Starting from the conformal decomposition of the spatial metric as

$$\gamma_{ij} = \psi^4 \tilde{\gamma}_{ij}, \tag{6.12}$$

where ψ is the conformal factor and $\tilde{\gamma}_{ij}$ being the flat metric in spherical coordinates. With this choice, the *Hamiltonian Constraint* takes the form,

$$8\nabla^2_{\mathit{flat}}\psi + \psi^5(A_{ij}A^{ij} - \frac{2}{3}K^2) + 16\pi\psi^5\rho + 2\epsilon\psi^5\widetilde{\rho^M} = 0, \tag{6.13}$$

where A_{ij} is the traceless part of the extrinsic curvature tensor K_{ij} and now the additional term $2\psi^5\widetilde{\rho^M}$ contains the modifications to GR.

The *Momentum Constraint* takes the form,

$$\nabla_j A^{ij} - \frac{2}{3}\nabla^i K - 8\pi j^i - \epsilon \widetilde{j^i_M} = 0, \tag{6.14}$$

which includes the additional current-like term $-\epsilon\widetilde{j^i_M}$. We take the extrinsic curvature to be traceless by setting the ansatz,

$$A_{ij} = \begin{pmatrix} K_{rr} & 0 & 0 \\ 0 & -r^2 \frac{K_{rr}}{2} & 0 \\ 0 & 0 & -r^2 \frac{K_{rr}\sin^2\theta}{2} \end{pmatrix}. \tag{6.15}$$

The expressions of the Hamiltonian and Momentum constraint under such ansatz read,

$$\frac{\partial^2\psi}{\partial r^2} = -\frac{2}{r}\frac{\partial\psi}{\partial r} - \frac{3}{16}\frac{K_{rr}^2}{\psi^3} - \pi\psi\left(\frac{\partial\phi}{\partial r}\right)^2 - \pi\psi^5\Sigma^2 - \frac{1}{4}\epsilon\psi^5\widetilde{\rho^M}, \tag{6.16}$$

$$\frac{\partial K_{rr}}{\partial r} = -2\psi^{-1}K_{rr}\frac{\partial\psi}{\partial r} - \frac{3}{r}K_{rr} + 8\pi\psi^4\Sigma\frac{\partial\phi}{\partial r} + \epsilon\psi^8\widetilde{j^r_M}. \tag{6.17}$$

Notice that $\widetilde{\rho^M}$ and $\widetilde{j^i_M}$ are the order reduced expressions that we obtained after the order reduction procedure, and when evaluated under this ansatz possess only up to first order derivatives of ψ and no derivatives of K_{rr}. In this form, these equations can be integrated directly to find solutions once the scalar field initial data is specified and appropriate boundary conditions set. This technique was used in [59], as "order-reduced direct integration", to successfully construct BH initial data in spacetimes in the presence of a scalar field for an eight-dimensional operator EFT of GR.

Scalar field

The initial scalar field is prescribed such that it is initially mostly in-falling towards the origin, this can be achieved by having a field of the form,

$$\phi(t,r) = \frac{\Phi(u)}{r}, \tag{6.18}$$

where $u \equiv r + t$ and,

$$\Phi(u) = Au^2 \exp\left(-\frac{(u-r_c)^2}{\sigma^2}\right), \tag{6.19}$$

where A, r_c and σ are the amplitude, pulse enter, and width, respectively. Under this choice, the initial values of scalar field variables are given by,

$$\phi_0 \equiv \phi(t=0,r) = Ar\exp\left(-\frac{(r-r_c)^2}{\sigma^2}\right), \tag{6.20}$$

$$\Sigma(t=0,r) = \frac{\phi_0}{\alpha}\left(\beta\left(\frac{1}{r}-\frac{2(r-r_c)}{\sigma^2}\right)-\left(\frac{2}{r}-\frac{2(r-r_c)}{\sigma^2}\right)\right), \tag{6.21}$$

where Σ is defined as,

$$\Sigma(t,r) = \frac{1}{\alpha}\left(\beta\frac{\partial\phi}{\partial_r}-\frac{\partial\phi}{\partial_t}\right). \tag{6.22}$$

Boundary conditions

To construct the initial data, boundary conditions for the fields must be prescribed. Regularity at the origin imposes $\Omega(r=0) \equiv \partial_r\psi(r=0) = 0$. For convenience, we can set $K_{rr} = 0$ at the origin. To determine the remaining condition on the ψ field, we impose that the exterior boundary conditions should have the following form,

$$\psi|_{r_{out}} = 1 + \frac{M}{2r_{out}}, \tag{6.23}$$

$$\left.\frac{\partial\psi}{\partial r}\right|_{r_{out}} = -\frac{M}{2r_{out}^2}, \tag{6.24}$$

where r_{out} is the exterior grid boundary, and M is the ADM mass (which will depend on the scalar field initial configuration). A way to achieve this is to perform a shooting procedure on the value of $\psi(r=0)$ such that the integrated solution on the outer boundary satisfies,

$$\psi|_{r_{out}} = 1 - r_{out}\left.\frac{\partial\psi}{\partial r}\right|_{r_{out}}, \tag{6.25}$$

we achieve this by implementing a Newton-Raphson method.

We impose that the initial values of gauge variables satisfy,

$$\alpha(t=0) = 1, \tag{6.26}$$

$$\beta(t=0) = 0, \tag{6.27}$$

$$\widetilde{\pi}(t=0) = 0, \tag{6.28}$$

$$\rho^i(t=0) = -2\psi^{-5}\Omega, \tag{6.29}$$

where the last two are required to initially satisfy the constraints (6.7a)-(6.7b).

6.4.2 Numerical implementation

The following numerical scheme is implemented to evolve the system presented in section 6.3. Time is integrated through a 4th-order Runge-Kutta with a CFL coefficient such that $dt = 0.25dx$, where dt is the time-step and dx denotes the uniform spatial grid spacing. Spatial derivatives are discretized via Finite Differences operators, which are 6th-order accurate in the interior and 3rd-order in the boundaries. Kreiss-Oliger dissipation is implemented with operators that are 8th-order accurate in the interior and 4th-order in the boundary. When no BH is present in the simulation, the grid extends from $r_i = 0$ to $r_{out} = 200$. During the evolution, the appearance of an apparent horizon is monitored; if one appears, then the code will excise a portion (including $r = 0$) of the domain contained inside this apparent horizon. A damped harmonic gauge [62, 136, 179] is adopted, which sets the gauge source vector to satisfy: $H_a = z(\log(\sqrt{g_{rr}}g_T\alpha^{-1})n_a - g_{ab}\beta^b\alpha^{-1})$. We take a fixed value of $z = 0.5$.

6.4.3 Monitoring quantities

As previously mentioned, an EFT description of a system involves a truncated expansion of a tower of curvature operators, and control over this expansion is lost if the curvature becomes too large. Determining whether the system remains within the regime of applicability of the EFT throughout evolution is a necessary condition [5] to guarantee that the observed behavior is representative of the true physics of the underlying theory in the low energy regime.

A reasonable indicator of whether the system is within the regime of applicability of the EFT is to compare if terms that are higher order in the perturbation scheme remain subdominant to lower order ones [70, 60]. For example one expects that $\mid R \mid > \mid \epsilon_1 R_{ab}R^{ab} \mid + \mid \epsilon_2 R^2 \mid$. Using the fact that $R_{ab} = 8\pi(T_{ab} - 1/2T g_{ab}) + \mathcal{O}(\epsilon_1, \epsilon_2)$, (ignoring higher order terms in ϵ_1 and ϵ_2) the inequality can be expressed as:

$$\mathcal{E}_R \equiv 8\pi(\mid \epsilon_1 \mid + \mid \epsilon_2 \mid) \mid \left(-\Sigma^2 g_{rr} + (\partial_r\phi)^2\right) \mid g_{rr}^{-1} < 1. \tag{6.30}$$

Another indicator that can be used to discern whether the theory remains in the EFT regime of applicability is through some curvature invariant that is non-vanishing for vacuum

---

[5] Even if the theory is at all times within the EFT's regime of validity, undesired issues such as secular effects [149, 148] could emerge and spoil the physics.

spacetimes, for instance, the Kretschmann scalar $\mathcal{C} \equiv R_{abcd}R^{abcd}$. Using this invariant, a natural threshold for the regime of applicability of the EFT is given by $\Lambda^{-2}\mathcal{C} > \Lambda^{-6}\mathcal{C}^2$, which can be easily rewritten as,

$$\mathcal{E}_{\mathcal{C}} \equiv \mathcal{C}\Lambda^{-4} \approx \mathcal{C}\max(\epsilon_1^2, \epsilon_2^2) < 1. \tag{6.31}$$

During evolution, these two quantities will be monitored to get an idea whether the system is in the validity regime of the EFT, close to leaving it or outside of it[6].

The way the equations have been rewritten after the order reduction is now somewhat more familiar to the equations we might encounter in GR, where metric components appear at most as second derivatives, and these second derivatives appear linearly in the equations. The system's characteristic speeds are usually evaluated to study hyperbolicity and, consequently, the well-posedness of an initial value problem. However, the presence of the third-order derivative of the scalar field in the gravitational equations prevents us from carrying out this analysis. One can, however, attempt to get some insight out of that procedure by computing the characteristic speeds by considering solely the gravitational sector (6.6c-6.6f) and considering the ϕ field as a source[7]. The characteristic matrix of that system is diagonalizable and possesses the following eigenvalues (characteristic speeds):

$$\lambda_{1\pm} = \beta \pm \frac{\alpha}{\sqrt{g_{rr}}}, \tag{6.32a}$$

$$\lambda_{2\pm} = \beta \pm \frac{\alpha\sqrt{8\pi(2\epsilon_1 - 4\epsilon_2)(\partial_r\phi)^2 + g_{rr}}}{g_{rr}}, \tag{6.32b}$$

$$\lambda_{3\pm} = \beta \pm \frac{\alpha\sqrt{8\pi(4\epsilon_1 - 8\epsilon_2)(\Sigma^2 g_{rr} - (\partial_r\phi)^2) + g_{rr}}}{g_{rr}}. \tag{6.32c}$$

Notice how all velocities in (6.32) reduce to what one obtains in GR when $\phi = 0$, when $\epsilon_1 = \epsilon_2 = 0$ or when $\epsilon_1 = 2\epsilon_2$. While the two first conditions imply that the theory reduces to GR, for the last one $\epsilon_1 = 2\epsilon_2$, the equations are still different from GR. When neither of those conditions is met, these speeds are modified from the GR ones and are real only under certain conditions. The radicand on $\lambda_{2\pm}$:

$$\chi_2 \equiv 8\pi(2\epsilon_1 - 4\epsilon_2)(\partial_r\phi)^2 + g_{rr}, \tag{6.33}$$

---

[6] There are, of course, many other quantities one could check, for example, checking that the six-dimensional operators should be subdominant to the four-dimensional ones, for example, $R_{ab}R^{ab}\Lambda^{-2} > R_{ab}{}^{ef}R^{abcd}R_{cdef}\Lambda^{-4}$.

[7] Note that ϕ evolves with $\Box\phi = 0$, so in a very local sense, its evolution should be well-posed

can become negative if $\epsilon_1 - 2\epsilon_2 < 0$ and $g_{rr} < -8\pi(2\epsilon_1 - 4\epsilon_2)(\partial_r\phi)^2$ which is possible if the scalar field gradients are large enough. Furthermore, regardless of the sign of $(\epsilon_1 - 2\epsilon_2)$ the radicand of $\lambda_{3\pm}$:

$$\chi_3 \equiv 8\pi(4\epsilon_1 - 8\epsilon_2)(\Sigma^2 g_{rr} - (\partial_r\phi)^2) + g_{rr}, \tag{6.34}$$

can become negative, the factor $(\Sigma^2 g_{rr} - (\partial_r\phi)^2)$ does not have definite sign and for large enough Σ or $\partial_r\phi$ then $\chi_3 < 0$ is a possibility.

This (simplified) analysis tells us that the system could undergo a character transition [29] during evolution rendering the problem ill-posed. The appearance of this transition could depend on the initial data prescribed; for example, a collapsing field would evolve to have very large gradients and trigger this transition, while a different configuration could avoid it. In this work, we will explore the evolution of a collapsing scalar field for different values of the coupling parameters and try to identify if such a transition happens, whether it triggers instabilities, and whether it occurs inside of the regime of applicability of the EFT.

6.5 Results

We turn our attention now to the evolution of the in-falling self-gravitating scalar field with different choices of the coupling parameters $\{\epsilon_1, \epsilon_2\}$. Whether the incoming pulse collapses into a BH or bounces back to infinity will depend mostly on the choice of its initial parameters, amplitude A, width, σ, and position r_c. To study the collapse case, these three parameters will be fixed to $A = 0.0023$, $\sigma = 1$, and $r_c = 10$. For these values in the initial scalar profile, the ADM mass of the system is $M_{ADM} = 1.024$ when $\epsilon_1 = \epsilon_2 = 0$. The relevant length scales in the modified theory ($|\epsilon_1|^{1/2} \approx |\epsilon_2|^{1/2} \approx \Lambda^{-1}$) should be then compared to the mass of the system. For reference, when these couplings are large $|\epsilon_1| = |\epsilon_2| = 0.1$ the difference in M_{ADM} is at the sub-percent level. Even though this work focuses on the collapsing scenario, the non-collapsing scenario was also studied. The evolution of that scenario in the regime of couplings explored is well-behaved up to $|\epsilon| \approx 10^{-1}$. Above such couplings, the system leaves the regime of applicability of the EFT. The evolution of the collapse scenario is more interesting, as we shall see in this section.

The main objective of these simulations is to explore how the evolution is altered as we modify the coupling parameters $\{\epsilon_1, \epsilon_2\}$, such as the behavior of the apparent horizon and curvature invariants. When couplings are turned off and GR is evolved, the initial

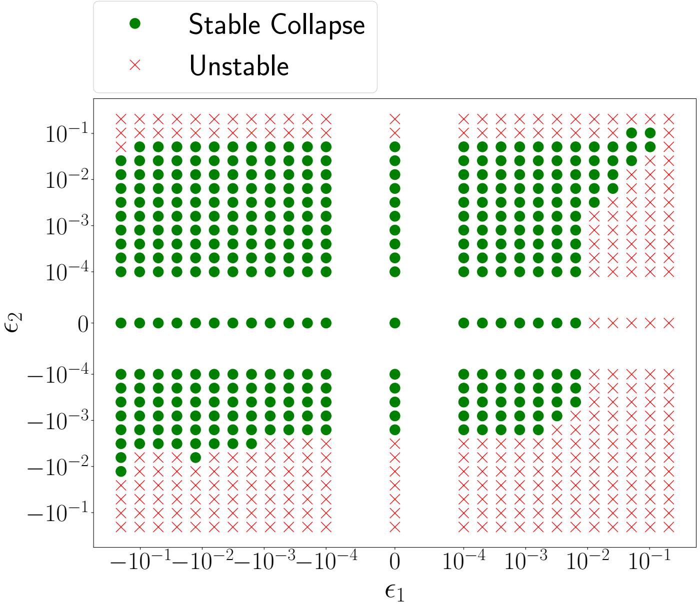

Figure 6.1: Parameter space of simulations for the collapse scenario. In green dots are simulations that are stable and collapse into a BH, and in red crosses are simulations that develop instabilities and crash.

pulse propagates toward the origin until a BH forms. It quickly accretes the scalar field and settles to its final configuration. The final mass of the formed BH is of $M_{BH} \approx 1.022$, indicating that only a very small portion of the scalar field is not accreted by the BH. To study how this same scenario would evolve when couplings are non-vanishing, an array of simulations is run with pairs of ϵ_1 and ϵ_2 taking values from $\{0, \tilde{\epsilon}_{n\pm}\}$, with $\tilde{\epsilon}_{n\pm} = \pm\epsilon_0 2^n$ for $n = 0..11$, with $\epsilon_0 = 10^{-4}$.

Figure 6.1 displays whether the evolution for a pair of values $\{\epsilon_1, \epsilon_2\}$ is stable and collapses into a BH (green dots) or if it develops instabilities and crashes (red crosses). This figure shows that there are a lot of points in the parameter space which develop instabilities, mostly when at least one of the couplings is large, especially for large and positive ϵ_1 and large and negative ϵ_2.

To better understand what is happening, we will first focus on simulations with $\epsilon_1 = 0$ or $\epsilon_2 = 0$ to study those terms individually. In Figure 6.2, we plot the maximum value of the Kretschmann scalar $\mathcal{C}$ in space and time for this subset of the parameter space. Here dots represent simulations that were stable during the evolution and collapsed into BHs, while the crosses represent simulations that crashed. This figure shows how, relative to

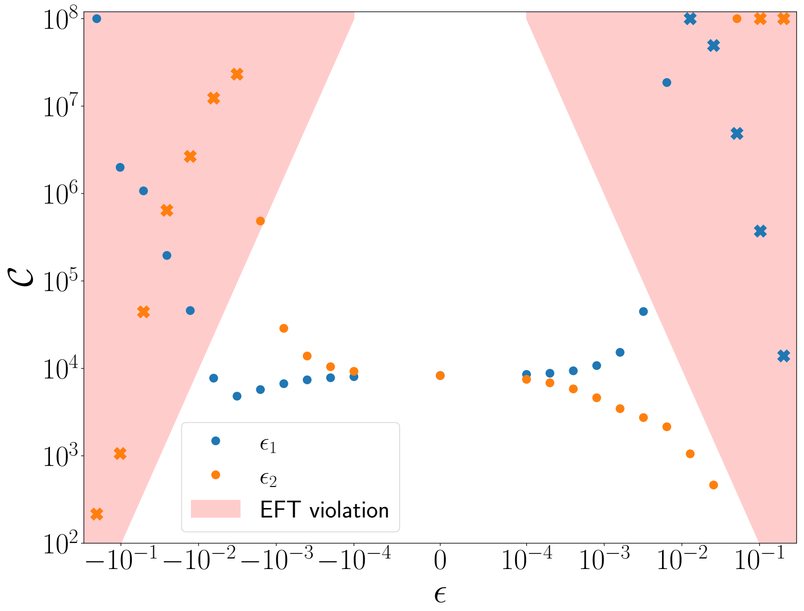

Figure 6.2: Maximum value of $\mathcal{C}$ across space and time for simulations in the collapse scenario for either $\epsilon_1 \neq 0$ or $\epsilon_2 \neq 0$. Dots indicate simulations that collapsed into BHs and remained stable; crosses indicate simulations that crashed. The red shaded region indicates values of $\mathcal{C}$ that lie outside of the regime of applicability of the EFT in accordance with (6.31). Values of $\mathcal{C} > 10^8$ have been labeled as 10^8 for convenience.

GR, a positive(negative) value of $\epsilon_1(\epsilon_2)$ tends to amplify the maximum value of $\mathcal{C}$ achieved during the evolution. Similarly (for small enough) negative(positive) values of $\epsilon_1(\epsilon_2)$ induce a suppression on the maximum value of $\mathcal{C}$. The magnitude of these amplifications or suppression grows as the scalar pulse approaches the origin, and corrections to GR become stronger. In Figure 6.3 we plot several snapshots of the $\mathcal{C}$ radial profile close to the collapse to a BH. Notice however in Figure 6.2 how for $\epsilon_1 \lessapprox -10^{-2}$ the behavior of $\mathcal{C}$ drastically changes to amplification as opposed to suppression.

An indicator that the evolution for $\epsilon_1 \lessapprox -10^{-2}$ is pathological and not physical is its convergence, which we display in Figure E.1. This figure shows how convergence falls rapidly as the scalar field approaches the origin in cases with $\epsilon_1 < 0$ especially losing all convergence for cases with $\epsilon_1 \lessapprox -10^{-2}$. Furthermore, one can see that the constraints in this regime of the couplings, as shown in Figure E.2, show violations above the one percent level, which indicates one should question the validity of the results.

Figure 6.2 also shows in the red shaded region the values of the Kretschmann scalar $\mathcal{C}$

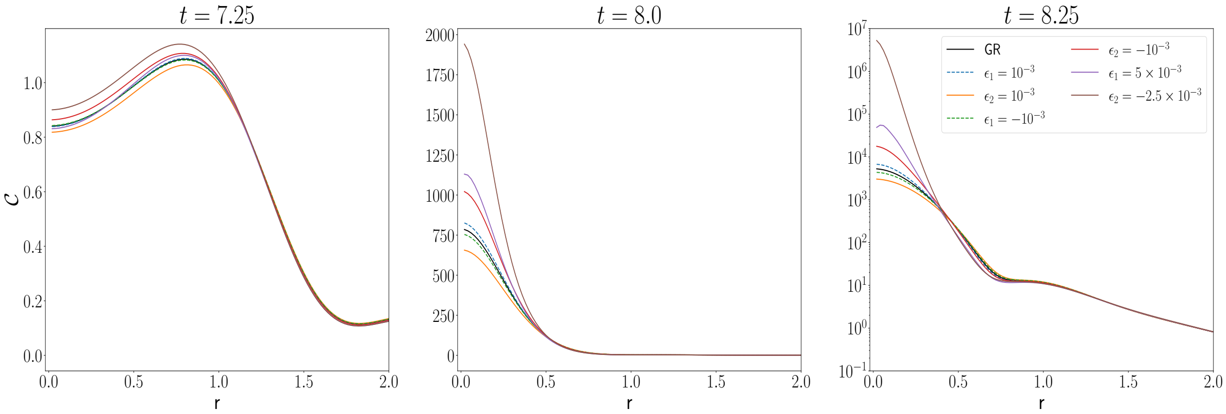

Figure 6.3: Snapshots of radial profiles of $\mathcal{C}$ at different times close to the collapse into a BH for different values of ϵ_1 and ϵ_2.

that would violate the EFT limit for each value of ϵ in accordance with (6.31). Interestingly a small negative value of ϵ_1 shows a suppression of $\mathcal{C}$, which in principle, helps to avoid the restricted region. However, as ϵ_1 becomes more negative at some point, an instability is triggered, generating an amplification of $\mathcal{C}$, clearly driving the system outside of the EFT regime of applicability. Here it is important to stress the order of these events. If an instability was generated once the system was already outside the EFT regime, this means that physics drove the system there and not pathologies. Suppose the system naturally explores higher curvatures and numerical instabilities appear after leaving the regime in which the EFT approach is valid. In that case, we need not worry about these simulations crashing and acknowledge the inadequacy of the EFT prescription to describe these scenarios. This seems to be the case for positive(negative) values of $\epsilon_1(\epsilon_2)$, which induce an amplification on $\mathcal{C}$ which drives the system outside of the valid EFT regime for $\mid \epsilon \mid \gtrapprox 10^{-3}$ and crash. In contrast, positive values of ϵ_2 which induce suppression of $\mathcal{C}$ manage to stay within the regime of applicability of the EFT and stable up to values of $\epsilon_2 \lessapprox 5 \times 10^{-2}$, beyond this values some instabilities are triggered, the system leaves the regime of applicability of the EFT and crashes. Both large negative values of ϵ_1 and large positive values of ϵ_2 seem to be developing instabilities when they are within the regime of applicability of the EFT. Perhaps for these regimes, controlling the higher frequencies via a *Fixing* approach as in [58, 59] could result in the resolution of the instabilities, but this is outside the scope of this work.

Similar behavior is observed on the maximum value of the Ricci scalar R, which we show in Figure 6.4, where we also include the EFT of applicability exclusion region in shaded

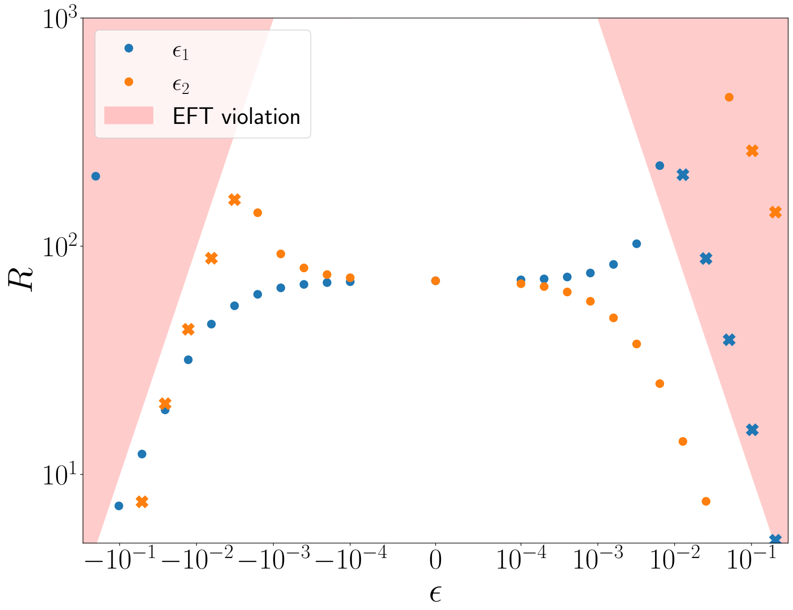

Figure 6.4: Maximum value of the Ricci scalar R across space and time for simulations in the collapse scenario for either $\epsilon_1 \neq 0$ or $\epsilon_2 \neq 0$. Dots indicate simulations that collapsed into BHs and remained stable; crosses indicate simulations that crashed. The red shaded region indicates values of R that lie outside of the regime of applicability of the EFT in accordance with (6.30).

red as indicated by the relation $\mathcal{E}_{\mathcal{R}} < 1$, see eq.(6.30). Interestingly, all of the simulations that crashed for $\epsilon_2 < 0$ do so within the allowed EFT regime dictated by (6.30); however, they are outside of the valid regime according to (6.31).

Another quantity that we can inspect is the radicand χ_3, see eq.(6.34), of the eigenvalue $\lambda_{3\pm}$, which, as we stated before, if it becomes negative could be related to a character transition and the breakdown of the initial value problem. Figure 6.5 shows the spatial minimum value of χ_3 as a function of time for simulations $\epsilon_1 < 0$ or $\epsilon_2 > 0$, which are the cases in which χ_3 decreases towards 0 and negative values. As Figure 6.5 shows for small(large) enough values of $\epsilon_1(\epsilon_2)$ χ_3 can become negative. As mentioned, very negative values of ϵ_1 trigger instabilities, losing convergence and leaving the EFT's applicability regime. Similar issues are present for large positive values of ϵ_2 where also $\chi_3 < 0$. However, such issues manifest before the $\chi_3 < 0$ threshold is violated. This suggests that this violation might not be the root cause of the instabilities but rather serve as a reliable indicator of their presence. This is not unexpected since this condition was built from

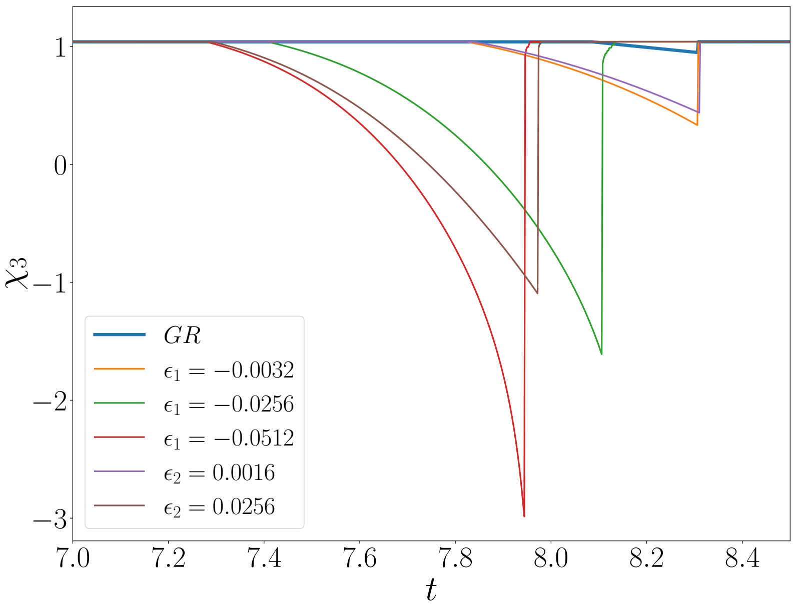

Figure 6.5: Minimum value of χ_3 (the radicand of the eigenvalue $\lambda_{3\pm}$) as a function of time for simulations in the collapse case for different values of ϵ_1 and ϵ_2. Once an apparent horizon is found, the minimum is computed outside the horizon, hiding negative values inside; this explains the sharp transitions.

an incomplete characteristic analysis in which the scalar field was considered a source, ignoring the presence of the higher derivatives of the field in the gravitational equations.

A noticeable effect that can be appreciated in Figure 6.5 is that simulations that develop negative values of χ_3 also form an apparent horizon sooner than the $\chi_3 > 0$ or GR cases. Figure 6.6 shows the areal radius $r_{\mathcal{A}}$ of the formed horizons as a function of time for different values of the couplings. The behavior for the GR case is as expected; around $t \approx 8.3$, an apparent horizon is found, and the areal radius quickly grows until all the scalar profile has been accreted and then relaxes to its final state. This is the same behavior that some of the curves in the plot, for example, for $\epsilon_1 = -0.0032$, $\epsilon_1 = 0.0064$, with the only difference that these curves follow slightly above and below the GR curve respectively. In contrast, for the $\epsilon_1 = -0.0256$, $\epsilon_1 = -0.0512$, $\epsilon_2 = 0.0256$ cases, also shown in Figure 6.6, the systems experience premature collapses to smaller BHs, after that $r_{\mathcal{A}}$ undergoes a brief growth, and then a substantial decrease before a new larger horizon (roughly the same size of the GR horizon) is formed. At this stage, we can see how the $r_{\mathcal{A}}$ grows above the GR

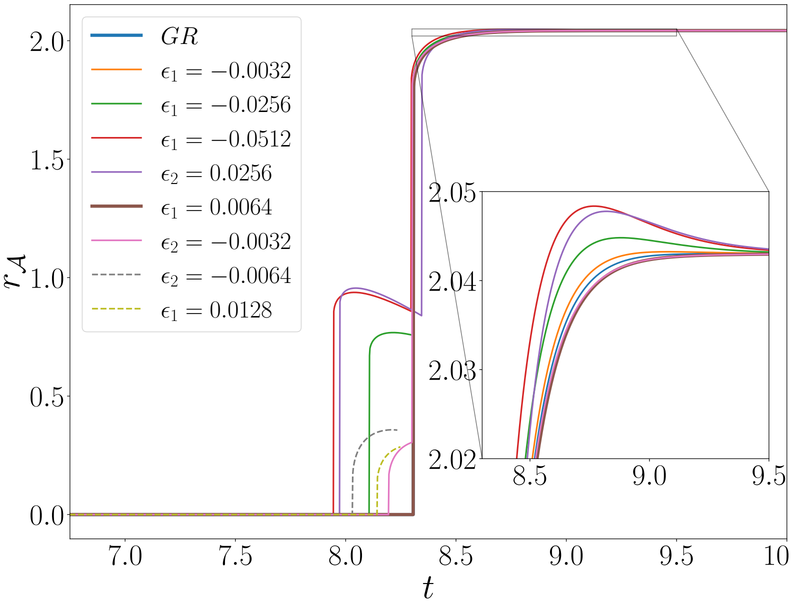

Figure 6.6: Areal radius $r_{\mathcal{A}}$ of the apparent horizon as a function of time for different values of ϵ_1 and ϵ_2. The dashed curves correspond to simulations that crashed after the appearance of the apparent horizon.

curve before decreasing[8] to join it as the final BH relaxes. Figure 6.6 also shows in dotted lines ($\epsilon_1 = 0.0128$ and $\epsilon_2 = -0.0064$) a couple of simulations that crashed, these also display the premature appearance of a small horizon before crashing. It is important to note that all of the simulations that show this type of exotic horizon behavior evolve away from the regime of applicability of the EFT defined by (6.31). The late-time behavior of all simulations, as shown in the plot, is similar; the final BH in all cases is essentially the same. This is not unexpected; once the scalar field has been accreted by the BH and the spacetime is essentially vacuum, the equations (6.2) reduce to Einstein's equation and can be evolved for very long times.

Having studied the ϵ_1 and ϵ_2 cases individually, we can outline a few observations.

1. Positive(negative) values of $\epsilon_1(\epsilon_2)$ strongly amplify the maximum value of curvature invariants such as $\mathcal{C}$ and R in contrast to GR. Their simulations are well behaved as long as the system stays within the regime of applicability of the EFT stipulated by

---

[8] The decrease of the BH's areal radius, and hence, decrease of its area is related to violations of the Null Convergence Condition [110, 111], similar behavior was observed in [59]

(6.30)-(6.31), beyond that regime simulations tend to crash.

2. Negative(positive) values of $\epsilon_1(\epsilon_2)$ strongly suppress the maximum value of curvature invariants such as $\mathcal{C}$ and R in contrast to GR. Even though the suppression of these curvature invariants would help keep the system within the regime of applicability of the EFT, for large enough values of the coupling (especially for ϵ_1), the solutions lose convergence, and the suppression becomes an amplification, driving the system outside of the EFT regime.

3. When the couplings are sufficiently small and within the regime of the EFT, the behavior of the BH formed is very similar to that of the BH formed in the GR case. Once the horizon is formed, the high curvature regions are hidden past the horizon, making modifications extremely small.

4. When the couplings are large enough, the BH formation becomes more exotic. Premature smaller BHs can form before a horizon similar to the one formed in the GR case appears. In addition, these smaller BHs can shrink in size during their short existence. Note, however, that the simulations in these regimes are always outside of the regime of applicability of the EFT, and hence the relevance of these results should be questioned.

With these observations, the interpretation of results where both ϵ_1 and ϵ_2 are non-zero is more direct. With our definitions of $\epsilon_1 = a_1\Lambda^{-2}$ and $\epsilon_2 = a_2\Lambda^{-2}$, Λ has dimension of inverse length and both a_1 and a_2 are dimensionless. For the most part, when one of the couplings is large and the other small, the behavior of the system is closer to the behavior of the large coupling, as we observed in the $\epsilon_1 \neq 0$ or $\epsilon_2 \neq 0$. More interesting behavior is observed when ϵ_1 and ϵ_2 are of the same order. For example, in the case where both ϵ_1 and ϵ_2 are positive, there is a competition between suppression and amplification induced in the curvature invariants, sometimes allowing the system to evolve with larger values of these couplings (in comparison to the individual cases) and stay within the regime of applicability of the EFT. This is the case for simulations with $\epsilon_1 \approx 2\epsilon_2$ as it can be seen in Figure 6.7 were a snapshot of the radial profile for $\mathcal{C}$ is plotted in such configurations. In the case where the signs of the couplings are opposite, the effects of their terms tend to push in the same direction and consequently sometimes take the system outside of the valid regime or trigger instabilities at smaller values of the coupling in comparison to the individual ϵ_1 or ϵ_2 cases.

We will not spend a lot of time going through different cases when both couplings are non-vanishing; however, informative plots are provided showing the different control

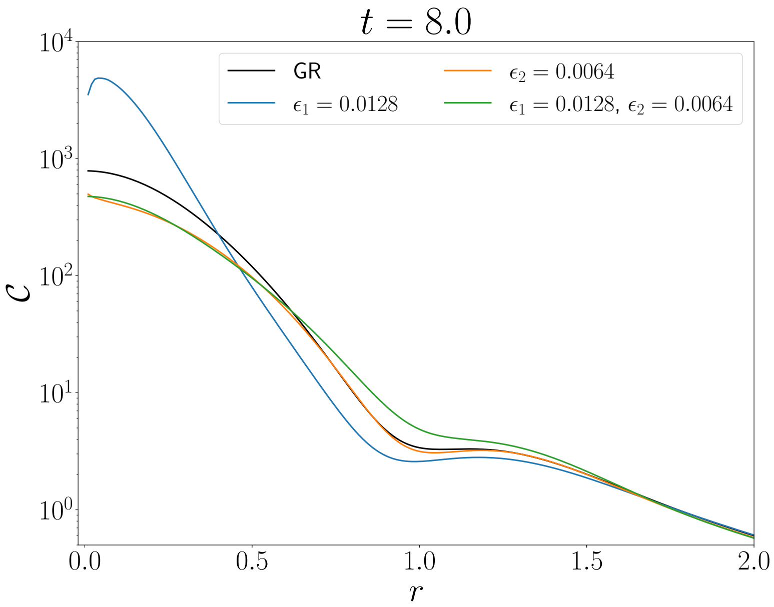

Figure 6.7: Snapshot of radial profile of $\mathcal{C}$ at t=8.11 for simulations with pairs of values of ϵ_1 and ϵ_2. Notice how the simulation with $\epsilon_1 = 0.0128$ and $\epsilon_2 = 0.064$ does not achieve the large values of $\mathcal{C}$ that the simulation with only $\epsilon_1 = 0.0128$ does.

quantities discussed for the ϵ_1 and ϵ_2 individual cases. Figure 6.8 shows the space-time minimum value of the radicand χ_2 of the eigenvalue $\lambda_{2\pm}$. In contrast to the previously observed for the χ_3 quantity, when χ_2 becomes negative, the couplings are already large enough to take the system outside the EFT regime. Figure 6.9 shows the minimum space-time value of χ_3 for each simulation. The interpretation of this plot follows directly from what was observed for the individual coupling cases. As mentioned before we can see that when $\epsilon_1 \approx \epsilon_2$ simulations that would have $\chi_3 < 0$ if only ϵ_2 was turned on, or crash if only ϵ_1 was on, now suffer non of those issues. Similar behavior is observed for the rest of the relevant quantities. Figure 6.10 displays the maximum value of $\mathcal{E}_R$, on it dark red dots correspond to points where the $\mathcal{E}_R > 1$ EFT condition was violated. Figure 6.11 shows the maximum of $\mathcal{E}_\mathcal{C}$ over time and space; the dark red dots represent points at which the EFT condition was violated. Finally, Figure 6.12 shows the maximum spacetime value of $\mathcal{C}$.

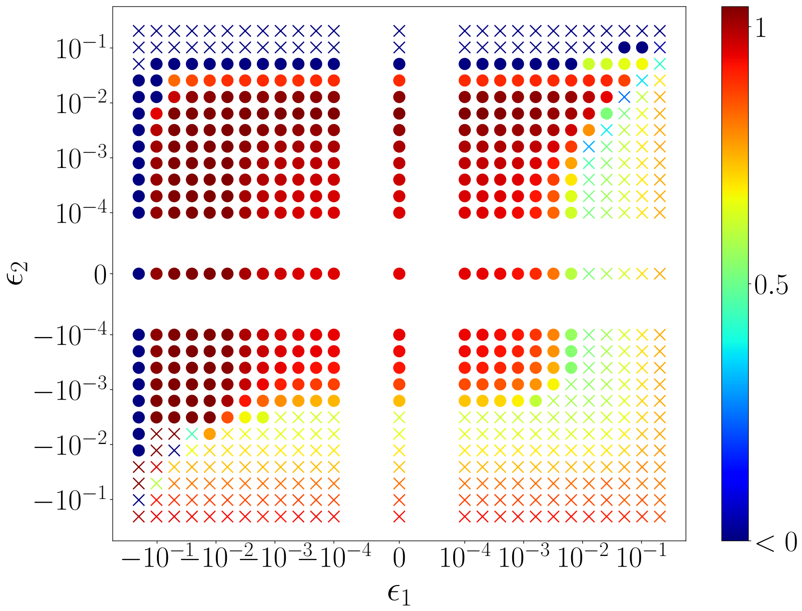

Figure 6.8: Minimum value of χ_2 over time and space for the collapse scenario with $A = 0.0023$. Dark blue marks represent simulations where the minimum value of χ_2 was at some point smaller than 0, making the eigenvalue complex, potentially indicating loss of well-posedness. Here crosses indicate that the simulation crashed.

6.6 Discussion

This study investigates the phenomenon of gravitational collapse in spherical symmetry within the framework of a dimension-four EFT extension to GR, commonly known as Quadratic Gravity. Within the EFT perspective, the solutions derived from this theory are expected to differ from those of GR only in the presence of matter, with the dimension-four operators representing leading-order corrections to GR within an EFT expansion.

In this particular research, instead of treating the additional degrees of freedom associated with higher derivatives as massive spin-0 and spin-2 modes, as done in previous studies such as [113, 112] under Ricci-flat (vacuum) scenarios, an *Order Reduction* technique [173] is employed to eliminate these degrees of freedom. Through numerical simulations, this work is able to dynamically form BHs from the collapse of a scalar field. In addition, we identify a parameter space regime where the system is well-behaved and remains within the applicable range of the EFT. However, strong deviations in the dynamics of curvature invariants during the collapse are observed within this regime. These deviations could

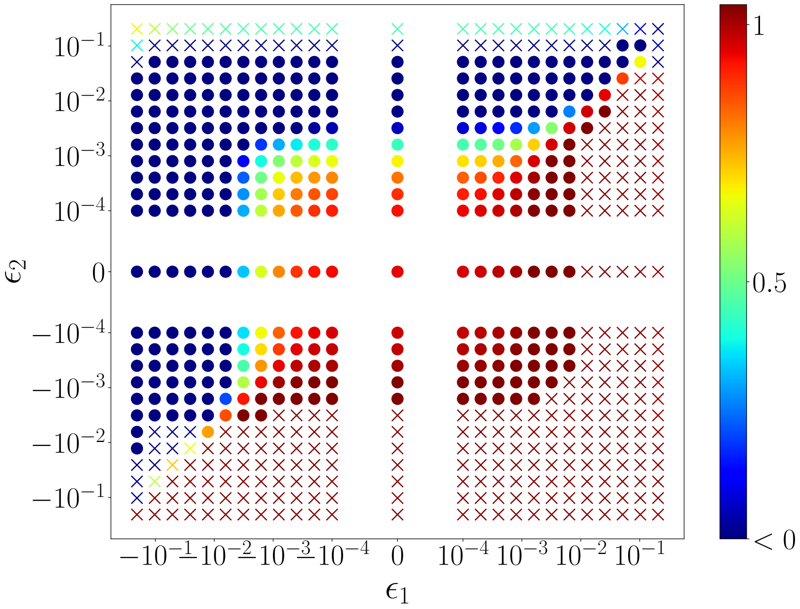

Figure 6.9: Minimum value of χ_3 over time and space for the collapse scenario with $A = 0.0023$. Dark blue dots represent simulations where the minimum value of χ_3 was at some point smaller than 0, making the eigenvalue complex, potentially indicating loss of well-posedness. Here crosses indicate that the simulation crashed.

be particularly relevant in astrophysical scenarios like the merger of a pair of neutron stars, where the altered system dynamics could have discernible effects on the emission of gravitational radiation.

Additionally, instances were found where simulations, initially showing good behavior, venture into high-curvature regimes that exceed the limits of the EFT approximation. In such cases, it becomes necessary to acknowledge the inadequacy of the chosen approach in describing the system dynamics within those specific scenarios. The specific value of the couplings ϵ_1 and ϵ_2 (consequently the value Λ) at which this will be the case is entirely dependent on the characteristics and relevant scales in the system[9]. Furthermore, specific regimes were identified where the system exhibits instabilities before the validity of the EFT description ceases. In these cases, alternative approaches such as *Fixing the Equations* may be implemented to mitigate the emergence of instabilities and control higher frequencies.

---

[9] For instance, allowing the scalar pulse to have a larger width, while adjusting the amplitude to keep the ADM mass fixed, allows to carry out stable simulations that stay within the limits of the EFT for larger values of ϵ_1 and ϵ_2.

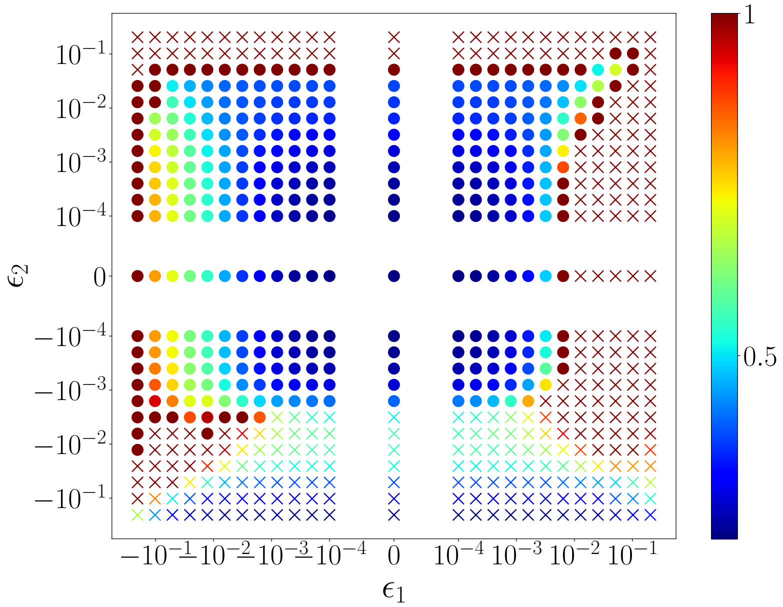

Figure 6.10: Maximum value of $\mathcal{E}_R$ over time and space for the collapse scenario with $A = 0.0023$. Dark red dots correspond to simulations where the EFT regime of applicability condition $\mathcal{E}_R < 1$ was violated at some point. Here crosses indicate that the simulation crashed.

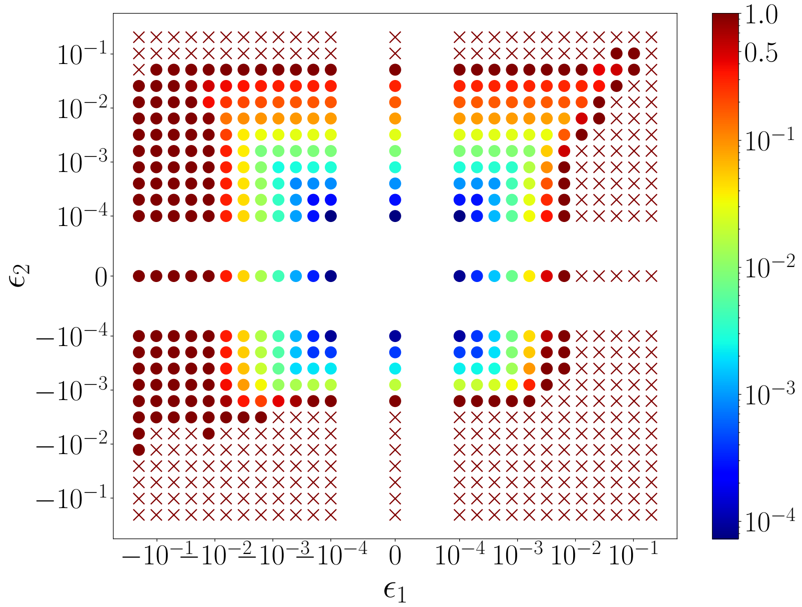

Figure 6.11: Maximum value of $\mathcal{E}_{\mathcal{C}}$ over time and space for the collapse scenario with $A = 0.0023$. Dark red dots correspond to simulations where the EFT regime of applicability condition $\mathcal{E}_{\mathcal{C}} < 1$ was violated at some point. Here crosses indicate that the simulation crashed.

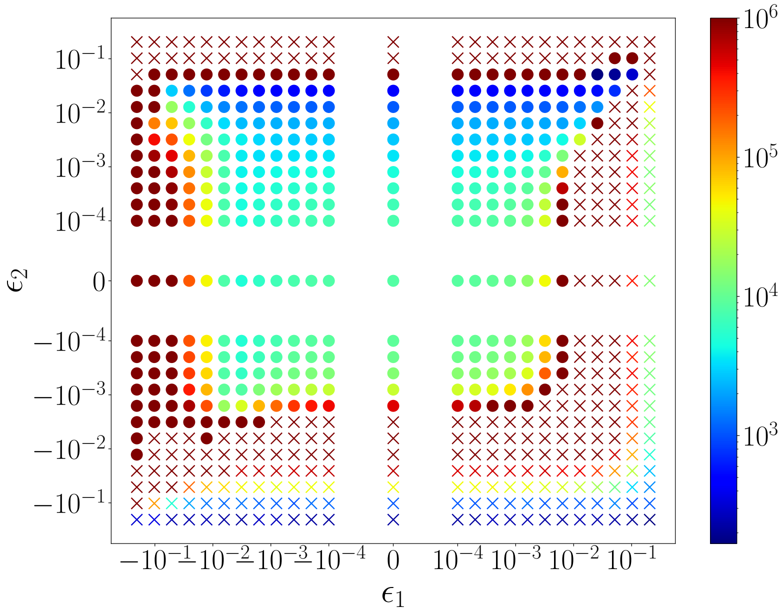

Figure 6.12: Maximum value of $\mathcal{C}$ over time and space for the collapse scenario with $A = 0.0023$. Values of $\mathcal{C} > 10^6$ have been labeled as 10^6 for convenience. Here crosses indicate that the simulation crashed.

Chapter 7

Outlook and future work

The main objective of this thesis was to develop and implement novel mathematical and numerical techniques to enable the study of deviations from GR in the nonlinear regime. The implementation of such methods is directed to theories that contain mathematical pathologies, which, if left untreated, make the understanding and study of phenomenology in nonlinear scenarios challenging. To study the implementation of these techniques, we focused on theories derived from EFT arguments. In these types of theories, modifications introduce higher than second-order derivatives as well as nonlinear terms in derivatives of the metric in the equations of motion. These pathologies are common to a broader class of theories, so a good understanding of handling these issues in the EFTs can be extended to other theories. In Chapters 4 and 5, we studied an EFT built from dimension-eight operators, which adds terms quartic in the Riemann tensor to the Einstein-Hilbert action.

In Chapter 4, we studied the dynamics of BHs in this EFT theory in spherical symmetry. By implementing an *Order reduction* approach, we eliminated the higher-order time derivatives in the equations of motion. A *Fixing the equations* approach was implemented to control the higher order spatial derivatives and the nonlinear in derivative terms. By introducing a minimally coupled scalar field into the system, we were able to study the dynamics of BHs in this theory. The accretion of the scalar pulse into the BH describes a highly nonlinear and dynamical event that serves as an ideal test bench for the novel methods we introduced. This study yielded valuable insights into the properties of BHs within this EFT theory. Firstly, we observed that a violation of the Null Convergence Condition can lead to a decrease in the area of the apparent horizons over time, a phenomenon not encountered in GR. Secondly, we established that after the accretion process, the solution describing the final BH corresponded to the same solution that initially described the BH, represented by (2.57), albeit with an increased mass of the BH. Lastly, our examination of the late-time solutions of the scalar field allowed us to study the QNM behavior of the field scattering off the BH. We found very good agreement between our results and the analytical predictions for the frequencies of these oscillations. This study of the spherically symmetric scenario demonstrated the efficacy of techniques like *Fixing the Equations* and *Order reduction* to deal with a very challenging extension to GR.

Building upon the promising results from Chapter 4, the logical progression in our research was to address the binary BH scenario within this particular EFT of gravity. In Chapter 5, we build up to the binary scenario by first considering a toy model that captures some of the characteristics of our system of interest and motivate a *fixed* system for the gravitational theory. Afterward, we tested the *fixed* system in the scenario of single boosted BHs to demonstrate the ability of our method to capture the dynamics of BHs moving. Having learned from the single BH scenario, we then evolve binary BHs in quasi-circular orbits all the way to the merger. With our methods, we can carry out these simulations for which solutions show no sign of instabilities. We study the GWs emitted from the system and contrast them to the solutions obtained in the GR case. For the cases studied, given the small nature of corrections and the resolution of the simulations, the analysis we carry out is qualitative rather than quantitative. For example, depending on the coupling ϵ sign, we can see a delay or an advance in the phase of the gravitational waveforms extracted from the system. Furthermore, the values of the QNM frequencies can also be studied and contrasted with perturbation theory results to confirm consistency with the sign of the modification. To finish Chapter 5, we discuss the dependence of our solutions in the ad-hoc portions of our model; these are the value of the fixing parameters $\{\sigma, \tau\}$ and the choice of *fixing* equation. We identify a dependence of our solution in the value of these parameters, but we attribute such dependence to the particular choice of *fixing* equation. Given the linear dependence of solutions on the value of σ, we suggest that extrapolations of the solutions to the $\sigma \to 0$ case can be a practical way of obtaining results in the "perfect tracking" case. Furthermore, after demonstrating how such dependence emerges from the choice of *fixing* equation, we propose a new system that has the potential to bypass the limitations of our current implementation. The study of this new system is left for future work. However, many studies can be carried out with the current implementation and our current predictions of gravitational waveforms. It is important to assess for what values of ϵ the waveforms obtained in this theory are distinguishable with respect to waveforms predicted in GR, considering the noise in signals and possible degeneracy. Such studies can also help us determine, for a given value of ϵ, the maximum value of the tracking $\mathcal{T}$ required to be able to claim departures from GR waveforms. In this study, we focused on relatively small values of ϵ, since these are the ones that provided the smallest tracking $\mathcal{T}$ values. Simulations with higher values of ϵ are also possible, showing consequently larger corrections, however, this comes at the cost of bigger $\mathcal{T}$ values. We will explore more of those cases in the future. Once the confidence in our waveforms is satisfactory, they can also be used to complement results obtained in the linear regime. For example, QNMs frequencies in this theory can only be obtained for slowly rotating BHs. In contrast, our solutions explore the ringdown with dimensionless spins of $a \approx 0.7$, and in principle, other final configurations can be explored.

Moving forward, we intend to implement the new alternative of *fixing* system introduced in (5.17) in search of improving the results obtained in Chapter 5. Furthermore, we will implement that *fixing* alternative in the dimension-six EFT, since this methodology is also adaptable to this theory.

In Chapter 6, we studied gravitational collapse in the context of an EFT of gravity built from dimension-four operators. The theory studied, often called Quadratic gravity, represents, in the presence of matter, the leading order corrections to GR from an EFT perspective. Similar to the dimension-eight operators case, the corrections in this theory introduce higher-order time derivatives of the metric. In this theory, the extra degrees of freedom introduced by the higher derivatives can be interpreted as one massive scalar field and one massive spin-2 field. However, the masses of these fields are above the EFT cutoff, so their dynamics should be unphysical. Furthermore, depending on the sign of the coupling, these degrees of freedom can become tachyonic, which would inevitably take the system outside the regime of applicability of the EFT. For these reasons, we opted to eliminate these degrees of freedom by means of an *Order Reduction*. The matter content in our studies was that of a collapsing massless scalar field. The collapsing scenario is ideal for testing the limits of the EFT, the efficacy of our approach to evolving this system, and potential deviations from GR predictions. Through numerical simulations, we identified a regime of the parameter space where the system is well-behaved and remains within the applicable range of the EFT, and we are successful in dynamically forming BHs. Furthermore, strong deviations in the dynamics of curvature invariants during the collapse are observed within this regime. However, there were regimes of the parameter space of couplings where numerical instabilities emerged before the system left the EFT regime of applicability. In such situations, an approach like *Fixing the equations* could be implemented as in Chapters 4 and 5 to obtain stable simulations. We leave this study for future work. Having demonstrated the feasibility of performing nonlinear studies within this theory, a more exciting and astrophysically relevant scenario to study is when the matter content comes from the presence of neutron stars. The study of single neutron star solutions and their dynamics in this theory is a work in progress. Subsequently, combining the lessons learned from the single neutron stars and the binary simulations of BHs in Chapter 5, we intend to tackle the binary neutron star merger scenario within this theory.

Through the different cases explored in this thesis, we demonstrated the feasibility of conducting studies of higher derivatives modified theories of gravity in the nonlinear regime. The methodologies we presented are general enough to address pathologies on a broader class of theories and will hopefully help the community to push forward in the search for deviations of GR.

References

[1] In Heinz-Otto Kreiss and Jens Lorenz, editors, *Initial-Boundary Value Problems and the Navier-Stokes Equations*, volume 136 of *Pure and Applied Mathematics*, page iii. Elsevier, 1989.

[2] B. P. Abbott et al. Observation of Gravitational Waves from a Binary Black Hole Merger. *Phys. Rev. Lett.*, 116(6):061102, 2016.

[3] B. P. Abbott et al. GW170817: Observation of Gravitational Waves from a Binary Neutron Star Inspiral. *Phys. Rev. Lett.*, 119(16):161101, 2017.

[4] R. Abbott et al. GW190814: Gravitational Waves from the Coalescence of a 23 Solar Mass Black Hole with a 2.6 Solar Mass Compact Object. *Astrophys. J. Lett.*, 896(2):L44, 2020.

[5] R. Abbott et al. GWTC-3: Compact Binary Coalescences Observed by LIGO and Virgo During the Second Part of the Third Observing Run. 11 2021.

[6] R. Abbott et al. Tests of General Relativity with GWTC-3. 12 2021.

[7] Marek A. Abramowicz and P. Chris Fragile. Foundations of Black Hole Accretion Disk Theory. *Living Rev. Rel.*, 16:1, 2013.

[8] Manuel Accettulli Huber, Andreas Brandhuber, Stefano De Angelis, and Gabriele Travaglini. From amplitudes to gravitational radiation with cubic interactions and tidal effects. *Phys. Rev. D*, 103(4):045015, 2021.

[9] Michalis Agathos, Walter Del Pozzo, Tjonnie G. F. Li, Chris Van Den Broeck, John Veitch, and Salvatore Vitale. TIGER: A data analysis pipeline for testing the strong-field dynamics of general relativity with gravitational wave signals from coalescing compact binaries. *Phys. Rev. D*, 89(8):082001, 2014.

[10] Gabriella Agazie et al. The NANOGrav 15-year Data Set: Evidence for a Gravitational-Wave Background. *Astrophys. J. Lett.*, 951(1), 2023.

[11] N. Aghanim et al. Planck 2018 results. VI. Cosmological parameters. *Astron. Astrophys.*, 641:A6, 2020. [Erratum: Astron.Astrophys. 652, C4 (2021)].

[12] Miguel Alcubierre, Bernd Bruegmann, Peter Diener, Michael Koppitz, Denis Pollney, Edward Seidel, and Ryoji Takahashi. Gauge conditions for long term numerical black hole evolutions without excision. *Phys. Rev. D*, 67:084023, 2003.

[13] Stephon Alexander and Nicolas Yunes. Chern-Simons Modified General Relativity. *Phys. Rept.*, 480:1–55, 2009.

[14] Daniela Alic, Carles Bona-Casas, Carles Bona, Luciano Rezzolla, and Carlos Palenzuela. Conformal and covariant formulation of the Z4 system with constraint-violation damping. *Phys. Rev. D*, 85:064040, 2012.

[15] Daniela Alic, Wolfgang Kastaun, and Luciano Rezzolla. Constraint damping of the conformal and covariant formulation of the Z4 system in simulations of binary neutron stars. *Phys. Rev. D*, 88(6):064049, 2013.

[16] Gwyneth Allwright and Luis Lehner. Towards the nonlinear regime in extensions to GR: assessing possible options. *Class. Quant. Grav.*, 36(8):084001, 2019.

[17] Tomas Andrade et al. GRChombo: An adaptable numerical relativity code for fundamental physics. *J. Open Source Softw.*, 6(68):3703, 2021.

[18] A. Savas Arapoglu, Cemsinan Deliduman, and K. Yavuz Eksi. Constraints on Perturbative f(R) Gravity via Neutron Stars. *JCAP*, 07:020, 2011.

[19] Llibert Aresté Saló, Katy Clough, and Pau Figueras. Well-Posedness of the Four-Derivative Scalar-Tensor Theory of Gravity in Singularity Avoiding Coordinates. *Phys. Rev. Lett.*, 129(26):261104, 2022.

[20] Richard L. Arnowitt, Stanley Deser, and Charles W. Misner. The Dynamics of general relativity. *Gen. Rel. Grav.*, 40:1997–2027, 2008.

[21] K. G. Arun et al. New horizons for fundamental physics with LISA. *Living Rev. Rel.*, 25(1):4, 2022.

[22] Abhay Ashtekar and Badri Krishnan. Isolated and dynamical horizons and their applications. *Living Rev. Rel.*, 7:10, 2004.

[23] Rudolf Baier, Paul Romatschke, Dam Thanh Son, Andrei O. Starinets, and Mikhail A. Stephanov. Relativistic viscous hydrodynamics, conformal invariance, and holography. *JHEP*, 04:100, 2008.

[24] Enrico Barausse, Carlos Palenzuela, Marcelo Ponce, and Luis Lehner. Neutron-star mergers in scalar-tensor theories of gravity. *Phys. Rev. D*, 87:081506, 2013.

[25] Thomas W. Baumgarte and Stuart L. Shapiro. On the numerical integration of Einstein's field equations. *Phys. Rev. D*, 59:024007, 1998.

[26] K. Becker, M. Becker, and J. H. Schwarz. *String theory and M-theory: A modern introduction.* Cambridge University Press, 12 2006.

[27] Brando Bellazzini, Clifford Cheung, and Grant N. Remmen. Quantum Gravity Constraints from Unitarity and Analyticity. *Phys. Rev. D*, 93(6):064076, 2016.

[28] Zvi Bern, Dimitrios Kosmopoulos, and Alexander Zhiboedov. Gravitational effective field theory islands, low-spin dominance, and the four-graviton amplitude. *J. Phys. A*, 54(34):344002, 2021.

[29] Laura Bernard, Luis Lehner, and Raimon Luna. Challenges to global solutions in Horndeski's theory. *Phys. Rev. D*, 100(2):024011, 2019.

[30] Sebastiano Bernuzzi and David Hilditch. Constraint violation in free evolution schemes: Comparing BSSNOK with a conformal decomposition of Z4. *Phys. Rev. D*, 81:084003, 2010.

[31] Emanuele Berti, Vitor Cardoso, and Andrei O. Starinets. Quasinormal modes of black holes and black branes. *Class. Quant. Grav.*, 26:163001, 2009.

[32] Miguel Bezares, Ricard Aguilera-Miret, Lotte ter Haar, Marco Crisostomi, Carlos Palenzuela, and Enrico Barausse. No Evidence of Kinetic Screening in Simulations of Merging Binary Neutron Stars beyond General Relativity. *Phys. Rev. Lett.*, 128(9):091103, 2022.

[33] Miguel Bezares, Lotte ter Haar, Marco Crisostomi, Enrico Barausse, and Carlos Palenzuela. Kinetic screening in nonlinear stellar oscillations and gravitational collapse. *Phys. Rev. D*, 104(4):044022, 2021.

[34] Taylor Binnington and Eric Poisson. Relativistic theory of tidal Love numbers. *Phys. Rev. D*, 80:084018, 2009.

[35] Luc Blanchet. Gravitational Radiation from Post-Newtonian Sources and Inspiralling Compact Binaries. *Living Rev. Rel.*, 17:2, 2014.

[36] C. Bona, T. Ledvinka, C. Palenzuela, and M. Zacek. General covariant evolution formalism for numerical relativity. *Phys. Rev. D*, 67:104005, 2003.

[37] C. Bona, T. Ledvinka, C. Palenzuela, and M. Zacek. A Symmetry breaking mechanism for the Z4 general covariant evolution system. *Phys. Rev. D*, 69:064036, 2004.

[38] Carles Bona, Joan Masso, Edward Seidel, and Joan Stela. A New formalism for numerical relativity. *Phys. Rev. Lett.*, 75:600–603, 1995.

[39] Jeffrey M. Bowen and James W. York, Jr. Time asymmetric initial data for black holes and black hole collisions. *Phys. Rev. D*, 21:2047–2056, 1980.

[40] Othmar Brodbeck, Simonetta Frittelli, Peter Hubner, and Oscar A. Reula. Einstein's equations with asymptotically stable constraint propagation. *J. Math. Phys.*, 40:909–923, 1999.

[41] J. David Brown. Generalized Harmonic Equations in 3+1 Form. *Phys. Rev. D*, 84:124012, 2011.

[42] Pablo Bueno, Pablo A. Cano, and Robie A. Hennigar. On the stability of Einsteinian Cubic Gravity black holes in EFT. 6 2023.

[43] Alessandra Buonanno, Lawrence E. Kidder, and Luis Lehner. Estimating the final spin of a binary black hole coalescence. *Phys. Rev. D*, 77:026004, 2008.

[44] C. P. Burgess. Quantum gravity in everyday life: General relativity as an effective field theory. *Living Rev. Rel.*, 7:5–56, 2004.

[45] C. P. Burgess. Introduction to Effective Field Theory. *Ann. Rev. Nucl. Part. Sci.*, 57:329–362, 2007.

[46] C. P. Burgess and M. Williams. Who You Gonna Call? Runaway Ghosts, Higher Derivatives and Time-Dependence in EFTs. *JHEP*, 08:074, 2014.

[47] Cliff P. Burgess. *Introduction to Effective Field Theory.* Cambridge University Press, 2021.

[48] Gioel Calabrese, Luis Lehner, David Neilsen, Jorge Pullin, Oscar Reula, Olivier Sarbach, and Manuel Tiglio. Novel finite differencing techniques for numerical relativity: Application to black hole excision. *Class. Quant. Grav.*, 20:L245–L252, 2003.

[49] Gioel Calabrese, Luis Lehner, Oscar Reula, Olivier Sarbach, and Manuel Tiglio. Summation by parts and dissipation for domains with excised regions. *Class. Quant. Grav.*, 21:5735–5758, 2004.

[50] Xian O. Camanho, Jose D. Edelstein, Juan Maldacena, and Alexander Zhiboedov. Causality Constraints on Corrections to the Graviton Three-Point Coupling. *JHEP*, 02:020, 2016.

[51] Pablo A. Cano, Kwinten Fransen, and Thomas Hertog. Ringing of rotating black holes in higher-derivative gravity. *Phys. Rev. D*, 102(4):044047, 2020.

[52] Pablo A. Cano, Kwinten Fransen, Thomas Hertog, and Simon Maenaut. Gravitational ringing of rotating black holes in higher-derivative gravity. *Phys. Rev. D*, 105(2):024064, 2022.

[53] Pablo A. Cano and Alejandro Ruipérez. Leading higher-derivative corrections to Kerr geometry. *JHEP*, 05:189, 2019. [Erratum: JHEP 03, 187 (2020)].

[54] Vitor Cardoso, Masashi Kimura, Andrea Maselli, and Leonardo Senatore. Black Holes in an Effective Field Theory Extension of General Relativity. *Phys. Rev. Lett.*, 121(25):251105, 2018.

[55] Gregorio Carullo. Enhancing modified gravity detection from gravitational-wave observations using the parametrized ringdown spin expansion coeffcients formalism. *Phys. Rev. D*, 103(12):124043, 2021.

[56] Juan Cayuso, Néstor Ortiz, and Luis Lehner. Fixing extensions to general relativity in the nonlinear regime. *Phys. Rev. D*, 96(8):084043, 2017.

[57] Ramiro Cayuso. Gravitational collapse in quadratic gravity. *arXiv:2307.15163*, 2023.

[58] Ramiro Cayuso, Pau Figueras, Tiago França, and Luis Lehner. Modelling self-consistently beyond General Relativity. *arXiv:2303.07246*, 2023.

[59] Ramiro Cayuso and Luis Lehner. Nonlinear, noniterative treatment of EFT-motivated gravity. *Phys. Rev. D*, 102(8):084008, 2020.

[60] Calvin Y. R. Chen, Claudia de Rham, Aoibheann Margalit, and Andrew J. Tolley. A cautionary case of casual causality. *JHEP*, 03:025, 2022.

[61] Matthew W. Choptuik. Universality and scaling in gravitational collapse of a massless scalar field. *Phys. Rev. Lett.*, 70:9–12, 1993.

[62] Matthew W. Choptuik and Frans Pretorius. Ultra Relativistic Particle Collisions. *Phys. Rev. Lett.*, 104:111101, 2010.

[63] D. Christodoulou and S. Klainerman. The Global nonlinear stability of the Minkowski space. 1993.

[64] Timothy Clifton, Pedro G. Ferreira, Antonio Padilla, and Constantinos Skordis. Modified Gravity and Cosmology. *Phys. Rept.*, 513:1–189, 2012.

[65] Katy Clough, Pau Figueras, Hal Finkel, Markus Kunesch, Eugene A. Lim, and Saran Tunyasuvunakool. GRChombo : Numerical Relativity with Adaptive Mesh Refinement. *Class. Quant. Grav.*, 32(24):245011, 2015.

[66] Maxence Corman, Justin L. Ripley, and William E. East. Nonlinear studies of binary black hole mergers in Einstein-scalar-Gauss-Bonnet gravity. *Phys. Rev. D*, 107(2):024014, 2023.

[67] Thibault Damour and Alessandro Nagar. Relativistic tidal properties of neutron stars. *Phys. Rev. D*, 80:084035, 2009.

[68] Claudia de Rham. Massive Gravity. *Living Rev. Rel.*, 17:7, 2014.

[69] Claudia de Rham, Jérémie Francfort, and Jun Zhang. Black Hole Gravitational Waves in the Effective Field Theory of Gravity. *Phys. Rev. D*, 102(2):024079, 2020.

[70] Claudia de Rham and Andrew J. Tolley. Causality in curved spacetimes: The speed of light and gravity. *Phys. Rev. D*, 102(8):084048, 2020.

[71] Claudia de Rham and Andrew J. Tolley. Speed of gravity. *Phys. Rev. D*, 101:063518, Mar 2020.

[72] Claudia de Rham, Andrew J. Tolley, and Jun Zhang. Causality Constraints on Gravitational Effective Field Theories. *Phys. Rev. Lett.*, 128(13):131102, 2022.

[73] Cemsinan Deliduman, K. Y. Eksi, and Vildan Keles. Neutron star solutions in perturbative quadratic gravity. *JCAP*, 05:036, 2012.

[74] Térence Delsate, David Hilditch, and Helvi Witek. Initial value formulation of dynamical Chern-Simons gravity. *Phys. Rev. D*, 91(2):024027, 2015.

[75] Guillaume Dideron, Suvodip Mukherjee, and Luis Lehner. SCoRe: A New Framework to Study Unmodeled Physics from Gravitational Wave Data. 9 2022.

[76] Peter Diener, Ernst Nils Dorband, Erik Schnetter, and Manuel Tiglio. New, efficient, and accurate high order derivative and dissipation operators satisfying summation by parts, and applications in three-dimensional multi-block evolutions. *J. Sci. Comput.*, 32:109–145, 2007.

[77] John F. Donoghue. General relativity as an effective field theory: The leading quantum corrections. *Phys. Rev. D*, 50:3874–3888, 1994.

[78] William E. East and Luis Lehner. Fate of a neutron star with an endoparasitic black hole and implications for dark matter. *Phys. Rev. D*, 100(12):124026, 2019.

[79] William E. East and Frans Pretorius. Binary neutron star mergers in Einstein-scalar-Gauss-Bonnet gravity. *Phys. Rev. D*, 106(10):104055, 2022.

[80] William E. East and Frans Pretorius. Binary neutron star mergers in Einstein-scalar-Gauss-Bonnet gravity, 2022.

[81] William E. East and Justin L. Ripley. Evolution of Einstein-scalar-Gauss-Bonnet gravity using a modified harmonic formulation. *Phys. Rev. D*, 103(4):044040, 2021.

[82] Christopher Eling, Ted Jacobson, and David Mattingly. Einstein-Aether theory. In *Deserfest: A Celebration of the Life and Works of Stanley Deser*, pages 163–179, 10 2004.

[83] Matthew Elley, Hector O. Silva, Helvi Witek, and Nicolás Yunes. Spin-induced dynamical scalarization, descalarization, and stealthness in scalar-Gauss-Bonnet gravity during a black hole coalescence. *Phys. Rev. D*, 106(4):044018, 2022.

[84] Solomon Endlich, Victor Gorbenko, Junwu Huang, and Leonardo Senatore. An effective formalism for testing extensions to General Relativity with gravitational waves. *JHEP*, 09:122, 2017.

[85] Jose María Ezquiaga and Miguel Zumalacárregui. Dark Energy in light of Multi-Messenger Gravitational-Wave astronomy. *Front. Astron. Space Sci.*, 5:44, 2018.

[86] Pau Figueras and Tiago França. Gravitational Collapse in Cubic Horndeski Theories. *Class. Quant. Grav.*, 37(22):225009, 2020.

[87] Pau Figueras and Tiago França. Black hole binaries in cubic Horndeski theories. *Phys. Rev. D*, 105(12):124004, 2022.

[88] Pau Figueras, Markus Kunesch, and Saran Tunyasuvunakool. End Point of Black Ring Instabilities and the Weak Cosmic Censorship Conjecture. *Phys. Rev. Lett.*, 116(7):071102, 2016.

[89] Eanna E. Flanagan and Tanja Hinderer. Constraining neutron star tidal Love numbers with gravitational wave detectors. *Phys. Rev. D*, 77:021502, 2008.

[90] Eanna E. Flanagan and Scott A. Hughes. Measuring gravitational waves from binary black hole coalescences: 1. Signal-to-noise for inspiral, merger, and ringdown. *Phys. Rev. D*, 57:4535–4565, 1998.

[91] Y. Foures-Bruhat. Theoreme d'existence pour certains systemes derivees partielles non lineaires. *Acta Mat.*, 88:141–225, 1952.

[92] Tiago França. *Binary Black Holes in Modified Gravity.* PhD thesis, Queen Mary University of London, 2023.

[93] Nicola Franchini, Miguel Bezares, Enrico Barausse, and Luis Lehner. Fixing the dynamical evolution in scalar-Gauss-Bonnet gravity. *Phys. Rev. D*, 106(6):064061, 2022.

[94] José T. Gálvez Ghersi and Leo C. Stein. Numerical renormalization-group-based approach to secular perturbation theory. *Phys. Rev. E*, 104(3):034219, 2021.

[95] Mary Gerhardinger, John T. Giblin, Jr., Andrew J. Tolley, and Mark Trodden. Well-posed UV completion for simulating scalar Galileons. *Phys. Rev. D*, 106(4):043522, 2022.

[96] Robert Geroch. Relativistic theories of dissipative fluids. *Journal of Mathematical Physics*, 36(8):4226–4241, 08 1995.

[97] Robert P. Geroch. Relativistic theories of dissipative fluids. *J. Math. Phys.*, 36:4226, 1995.

[98] Robert P. Geroch. On hyperbolic 'theories' of relativistic dissipative fluids. 3 2001.

[99] Abhirup Ghosh, Nathan K. Johnson-Mcdaniel, Archisman Ghosh, Chandra Kant Mishra, Parameswaran Ajith, Walter Del Pozzo, Christopher P. L. Berry, Alex B. Nielsen, and Lionel London. Testing general relativity using gravitational wave signals from the inspiral, merger and ringdown of binary black holes. *Class. Quant. Grav.*, 35(1):014002, 2018.

[100] Walter D. Goldberger and Ira Z. Rothstein. An Effective field theory of gravity for extended objects. *Phys. Rev. D*, 73:104029, 2006.

[101] Marc H. Goroff and Augusto Sagnotti. The Ultraviolet Behavior of Einstein Gravity. *Nucl. Phys. B*, 266:709–736, 1986.

[102] Eric Gourgoulhon. 3+1 formalism and bases of numerical relativity. 3 2007.

[103] David J. Gross and John H. Sloan. The Quartic Effective Action for the Heterotic String. *Nucl. Phys. B*, 291:41–89, 1987.

[104] David J. Gross and Edward Witten. Superstring Modifications of Einstein's Equations. *Nucl. Phys. B*, 277:1, 1986.

[105] A. Gruzinov and M. Kleban. Causality Constrains Higher Curvature Corrections to Gravity. *Class. Quant. Grav.*, 24:3521–3524, 2007.

[106] Carsten Gundlach and Jose M. Martin-Garcia. Symmetric hyperbolic form of systems of second order evolution equations subject to constraints. *Phys. Rev. D*, 70:044031, 2004.

[107] Carsten Gundlach and Jose M. Martin-Garcia. Hyperbolicity of second-order in space systems of evolution equations. *Class. Quant. Grav.*, 23:S387–S404, 2006.

[108] Carsten Gundlach, Jose M. Martin-Garcia, Gioel Calabrese, and Ian Hinder. Constraint damping in the Z4 formulation and harmonic gauge. *Class. Quant. Grav.*, 22:3767–3774, 2005.

[109] J. Hadamard. Sur les problèmes aux dérivés partielles et leur signification physique. *Princeton University Bulletin*, 13:49–52, 1902.

[110] S.W. Hawking and G.F.R. Ellis. *The Large Scale Structure of Space-Time*. Cambridge Monographs on Mathematical Physics. Cambridge University Press, 2 2011.

[111] Sean A. Hayward. Marginal surfaces and apparent horizons. 3 1993.

[112] Aaron Held and Hyun Lim. Nonlinear dynamics of quadratic gravity in spherical symmetry. *Phys. Rev. D*, 104(8):084075, 2021.

[113] Aaron Held and Hyun Lim. Nonlinear Evolution of Quadratic Gravity in 3+1 Dimensions. 6 2023.

[114] Aaron Held and Jun Zhang. Instability of spherically symmetric black holes in quadratic gravity. *Phys. Rev. D*, 107(6):064060, 2023.

[115] David Hilditch and Ronny Richter. Hyperbolicity of High Order Systems of Evolution Equations. *J. Hyperbol. Diff. Equat.*, 12(01):1–35, 2015.

[116] Eric W. Hirschmann, Luis Lehner, Steven L. Liebling, and Carlos Palenzuela. Black Hole Dynamics in Einstein-Maxwell-Dilaton Theory. *Phys. Rev. D*, 97(6):064032, 2018.

[117] Stefan Hollands, Akihiro Ishibashi, and Harvey S. Reall. A stationary black hole must be axisymmetric in effective field theory. 12 2022.

[118] Gregory Walter Horndeski. Second-order scalar-tensor field equations in a four-dimensional space. *Int. J. Theor. Phys.*, 10:363–384, 1974.

[119] W. Israel and J. M. Stewart. Transient relativistic thermodynamics and kinetic theory. *Annals of Physics*, 118(2):341–372, April 1979.

[120] W. Israel and J.M. Stewart. Thermodynamics of nonstationary and transient effects in a relativistic gas. *Physics Letters A*, 58(4):213–215, 1976.

[121] W. Israel and J.M. Stewart. Transient relativistic thermodynamics and kinetic theory. *Annals of Physics*, 118(2):341–372, 1979.

[122] Werner Israel. Nonstationary irreversible thermodynamics: A causal relativistic theory. *Annals of Physics*, 100(1):310–331, 1976.

[123] I. Jack, D. R. T. Jones, and N. Mohammedi. A Four Loop Calculation of the Metric Beta Function for the Bosonic σ Model and the String Effective Action. *Nucl. Phys. B*, 322:431–470, 1989.

[124] I. Jack, D. R. T. Jones, and N. Mohammedi. The Four Loop Metric Beta Function for the Bosonic σ Model. *Phys. Lett. B*, 220:171–175, 1989.

[125] T. Jayasinghe et al. A unicorn in monoceros: the $3\,\mathrm{M}\odot$ dark companion to the bright, nearby red giant V723 Mon is a non-interacting, mass-gap black hole candidate. *Mon. Not. Roy. Astron. Soc.*, 504(2):2577–2602, 2021.

[126] Kostas D. Kokkotas and Bernd G. Schmidt. Quasinormal modes of stars and black holes. *Living Rev. Rel.*, 2:2, 1999.

[127] Aron D. Kovacs. On the construction of asymptotically flat initial data in scalar-tensor effective field theory. 3 2021.

[128] Áron D. Kovács and Harvey S. Reall. Well-posed formulation of Lovelock and Horndeski theories. *Phys. Rev. D*, 101(12):124003, 2020.

[129] Áron D. Kovács and Harvey S. Reall. Well-Posed Formulation of Scalar-Tensor Effective Field Theory. *Phys. Rev. Lett.*, 124(22):221101, 2020.

[130] Robert H. Kraichnan. Inertial Ranges in Two-Dimensional Turbulence. *The Physics of Fluids*, 10(7):1417–1423, 07 1967.

[131] Guillermo Lara, Miguel Bezares, and Enrico Barausse. UV completions, fixing the equations, and nonlinearities in k-essence. *Phys. Rev. D*, 105(6):064058, 2022.

[132] Edward W. Leaver. Spectral decomposition of the perturbation response of the Schwarzschild geometry. *Phys. Rev. D*, 34:384–408, 1986.

[133] Jean Letessier and Johann Rafelski. *Hadrons and Quark–Gluon Plasma.* Oxford University Press, 2002.

[134] A. Lichnerowicz. *J. Math. Pures et Appl.*, 23:37–63, 1944.

[135] Lee Lindblom, Mark A. Scheel, Lawrence E. Kidder, Robert Owen, and Oliver Rinne. A New generalized harmonic evolution system. *Class. Quant. Grav.*, 23:S447–S462, 2006.

[136] Lee Lindblom and Bela Szilagyi. An Improved Gauge Driver for the GH Einstein System. *Phys. Rev. D*, 80:084019, 2009.

[137] Mariangela Lisanti. Lectures on Dark Matter Physics. In *Theoretical Advanced Study Institute in Elementary Particle Physics: New Frontiers in Fields and Strings*, pages 399–446, 2017.

[138] D. Lovelock. The Einstein tensor and its generalizations. *J. Math. Phys.*, 12:498–501, 1971.

[139] Michele Maggiore et al. Science Case for the Einstein Telescope. *JCAP*, 03:050, 2020.

[140] Jerome Martin. Everything You Always Wanted To Know About The Cosmological Constant Problem (But Were Afraid To Ask). *Comptes Rendus Physique*, 13:566–665, 2012.

[141] Ken Mattsson. Diagonal-norm summation by parts operators for finite difference approximations of third and fourth derivatives. *Journal of Computational Physics*, 274:432 – 454, 2014.

[142] Ken Mattsson and Jan Nordström. Summation by parts operators for finite difference approximations of second derivatives. *Journal of Computational Physics*, 199(2):503 – 540, 2004.

[143] R. R. Metsaev and Arkady A. Tseytlin. Curvature Cubed Terms in String Theory Effective Actions. *Phys. Lett. B*, 185:52–58, 1987.

[144] J. W. Moffat. Scalar-tensor-vector gravity theory. *JCAP*, 03:004, 2006.

[145] Gabriel Nagy, Omar E. Ortiz, and Oscar A. Reula. Strongly hyperbolic second order Einstein's evolution equations. *Phys. Rev. D*, 70:044012, 2004.

[146] T. Nakamura, K. Oohara, and Y. Kojima. General Relativistic Collapse to Black Holes and Gravitational Waves from Black Holes. *Prog. Theor. Phys. Suppl.*, 90:1–218, 1987.

[147] D. R. Noakes. THE INITIAL VALUE FORMULATION OF HIGHER DERIVATIVE GRAVITY. *J. Math. Phys.*, 24:1846–1850, 1983.

[148] Maria Okounkova. Numerical relativity simulation of GW150914 in Einstein dilaton Gauss-Bonnet gravity. *Phys. Rev. D*, 102(8):084046, 2020.

[149] Maria Okounkova, Leo C. Stein, Jordan Moxon, Mark A. Scheel, and Saul A. Teukolsky. Numerical relativity simulation of GW150914 beyond general relativity. *Phys. Rev. D*, 101(10):104016, 2020.

[150] Maria Okounkova, Leo C. Stein, Mark A. Scheel, and Daniel A. Hemberger. Numerical binary black hole mergers in dynamical Chern-Simons gravity: Scalar field. *Phys. Rev. D*, 96(4):044020, 2017.

[151] Maria Okounkova, Leo C. Stein, Mark A. Scheel, and Saul A. Teukolsky. Numerical binary black hole collisions in dynamical Chern-Simons gravity. *Phys. Rev. D*, 100(10):104026, 2019.

[152] M. Ostrogradsky. Mémoires sur les équations différentielles, relatives au problème des isopérimètres. *Mem. Acad. St. Petersbourg*, 6(4):385–517, 1850.

[153] Giuseppe Papallo and Harvey S. Reall. On the local well-posedness of Lovelock and Horndeski theories. *Phys. Rev. D*, 96(4):044019, 2017.

[154] Rafael A. Porto. The effective field theorist's approach to gravitational dynamics. *Phys. Rept.*, 633:1–104, 2016.

[155] Rafael A. Porto. The Tune of Love and the Nature(ness) of Spacetime. *Fortsch. Phys.*, 64(10):723–729, 2016.

[156] Frans Pretorius. Evolution of binary black hole spacetimes. *Phys. Rev. Lett.*, 95:121101, 2005.

[157] Frans Pretorius. Numerical relativity using a generalized harmonic decomposition. *Class. Quant. Grav.*, 22:425–452, 2005.

[158] Miren Radia, Ulrich Sperhake, Amelia Drew, Katy Clough, Pau Figueras, Eugene A. Lim, Justin L. Ripley, Josu C. Aurrekoetxea, Tiago França, and Thomas Helfer. Lessons for adaptive mesh refinement in numerical relativity. *Class. Quant. Grav.*, 39(13):135006, 2022.

[159] Harvey S. Reall and Claude M. Warnick. Effective field theory and classical equations of motion. *J. Math. Phys.*, 63(4):042901, 2022.

[160] Chloe Richards, Alexandru Dima, and Helvi Witek. Black Holes in Massive Dynamical Chern-Simons gravity: scalar hair and quasibound states at decoupling. 5 2023.

[161] Justin L. Ripley and Frans Pretorius. Hyperbolicity in Spherical Gravitational Collapse in a Horndeski Theory. *Phys. Rev. D*, 99(8):084014, 2019.

[162] Maximilian Ruhdorfer, Javi Serra, and Andreas Weiler. Effective Field Theory of Gravity to All Orders. *JHEP*, 05:083, 2020.

[163] Olivier Sarbach and Manuel Tiglio. Continuum and Discrete Initial-Boundary-Value Problems and Einstein's Field Equations. *Living Rev. Rel.*, 15:9, 2012.

[164] Erik Schnetter. Time Step Size Limitation Introduced by the BSSN Gamma Driver. *Class. Quant. Grav.*, 27:167001, 2010.

[165] Noah Sennett, Richard Brito, Alessandra Buonanno, Victor Gorbenko, and Leonardo Senatore. Gravitational-Wave Constraints on an Effective Field-Theory Extension of General Relativity. *Phys. Rev. D*, 102(4):044056, 2020.

[166] Noah Sennett, Richard Brito, Alessandra Buonanno, Victor Gorbenko, and Leonardo Senatore. Gravitational-wave constraints on an effective-field-theory extension of general relativity. *Phys. Rev. D*, 102:044056, Aug 2020.

[167] Pau Amaro Seoane et al. The Gravitational Universe. 5 2013.

[168] Masaru Shibata and Takashi Nakamura. Evolution of three-dimensional gravitational waves: Harmonic slicing case. *Phys. Rev. D*, 52:5428–5444, 1995.

[169] Hector O. Silva, Abhirup Ghosh, and Alessandra Buonanno. Black-hole ringdown as a probe of higher-curvature gravity theories. 2022.

[170] Hector O. Silva, Abhirup Ghosh, and Alessandra Buonanno. Black-hole ringdown as a probe of higher-curvature gravity theories. *Phys. Rev. D*, 107(4):044030, 2023.

[171] Hector O. Silva, Helvi Witek, Matthew Elley, and Nicolás Yunes. Dynamical Descalarization in Binary Black Hole Mergers. *Phys. Rev. Lett.*, 127(3):031101, 2021.

[172] Larry Smarr and James W. York. Kinematical conditions in the construction of spacetime. *Phys. Rev. D*, 17:2529–2551, May 1978.

[173] Adam R. Solomon and Mark Trodden. Higher-derivative operators and effective field theory for general scalar-tensor theories. *JCAP*, 02:031, 2018.

[174] K. S. Stelle. Renormalization of Higher Derivative Quantum Gravity. *Phys. Rev. D*, 16:953–969, 1977.

[175] Gerard 't Hooft and M. J. G. Veltman. One loop divergencies in the theory of gravitation. *Ann. Inst. H. Poincare Phys. Theor. A*, 20:69–94, 1974.

[176] Saul A. Teukolsky. Perturbations of a rotating black hole. 1. Fundamental equations for gravitational electromagnetic and neutrino field perturbations. *Astrophys. J.*, 185:635–647, 1973.

[177] Farid Thaalba, Miguel Bezares, Nicola Franchini, and Thomas P. Sotiriou. Spherical collapse in scalar-Gauss-Bonnet gravity: taming ill-posedness with a Ricci coupling. 6 2023.

[178] Todd A. Thompson et al. Discovery of a Candidate Black Hole - Giant Star Binary System in the Galactic Field. 6 2018.

[179] Vijay Varma and Mark A. Scheel. Constructing a boosted, spinning black hole in the damped harmonic gauge. *Phys. Rev. D*, 98(8):084032, 2018.

[180] Steven Weinberg. The Cosmological Constant Problem. *Rev. Mod. Phys.*, 61:1–23, 1989.

[181] J. M. Weisberg, D. J. Nice, and J. H. Taylor. Timing Measurements of the Relativistic Binary Pulsar PSR B1913+16. *Astrophys. J.*, 722:1030–1034, 2010.

[182] Clifford M. Will. The Confrontation between General Relativity and Experiment. *Living Rev. Rel.*, 17:4, 2014.

[183] Clifford M. Will. *Theory and Experiment in Gravitational Physics*. Cambridge University Press, 9 2018.

[184] Helvi Witek, Leonardo Gualtieri, Paolo Pani, and Thomas P. Sotiriou. Black holes and binary mergers in scalar Gauss-Bonnet gravity: scalar field dynamics. *Phys. Rev. D*, 99(6):064035, 2019.

[185] James W. York, Jr. Gravitational degrees of freedom and the initial-value problem. *Phys. Rev. Lett.*, 26:1656–1658, 1971.

[186] James W. York, Jr. Role of conformal three geometry in the dynamics of gravitation. *Phys. Rev. Lett.*, 28:1082–1085, 1972.

[187] James W. York, Jr. Kinematics and Dynamics of General Relativity. In *Workshop on Sources of Gravitational Radiation*, pages 83–126, 1978.

APPENDICES

Appendix A

Prototypical equation, Fixing the equations

In this appendix, we will explore an example of an equation that contains some of the pathologies present in the gravitational theory we mean to evolve. This simplified model allows us to explore a range of alternatives on how to “fix” its equations to obtain insight into how to proceed in the gravitational sector. The model we considered is described by the following equation[1],

$$\Box\phi = -\epsilon\partial_t^4\phi, \tag{A.1}$$

where $\Box$ is the Laplacian operator in Minkowski's spacetime. For simplicity, we shall consider this equation in 1+1 dimensions. The system as presented possesses 4th-order time derivatives of the field ϕ. As we shall show soon, a straightforward analysis indicates that the higher time derivatives lead to ghost modes that grow without bound.

In this simple example, we assume that the ϵ proportional term is the leading order term in some expansion in this parameter that is ultimately truncated. This expansion and the truncated nature of this equation could be responsible for the appearance of instabilities that might not be present in the full underlying theory. This section aims to explore ways one can modify the equations in a way that removes instabilities and reproduces the physics in the long wavelength regime.

The system we propose as a fixed version is given by:

---

[1] This is a slightly modified version of an example considered in [56], where the fourth order derivatives are of space instead of time.

$$\Box\phi = -\epsilon\partial_t^2\Pi \tag{A.2}$$

$$\Box\Pi = -\frac{1}{\sigma}\left(-\tau\partial_t\Pi - \left(\Pi - \partial_t^2\phi\right)\right) \tag{A.3}$$

By means of a "reduction of order" we replace the $\partial_t^2\phi$ on the right-hand side of (A.3) using equation (A.2) to $\mathcal{O}(0)$ in ϵ, obtaining,

$$\Box\Pi = -\frac{1}{\sigma}\left(-\tau\partial_t\Pi - \left(\Pi - \partial_x^2\phi\right)\right) \tag{A.4}$$

The resulting second-order system determines the evolution of the variable Π that is damped towards the "source" $\partial_x^2\phi$ on a timescale σ/τ .

We will first study these systems with an analytic approach and point out their differences.

A.0.1 Analytics

Original system

Here we analyze the behavior of solutions of (A.1) under a Fourier mode ansatz given by,

$$\phi(t, x) = e^{st}e^{ikx}. \tag{A.5}$$

The dispersion relation for this system has four solutions:

$$s_{(\pm,\pm)} = \pm\sqrt{\frac{1 \pm \sqrt{1 + 4\epsilon k^2}}{2\epsilon}}. \tag{A.6}$$

For $\epsilon > 0$, two of these solutions are real ($s_{+,+}$ and $s_{-,+}$), while the other two are imaginary. It is then immediate to see that the solution given by $s_{+,+}$ is unstable for all values of k. We can see this in Figure A.1 and Figure A.2 for $\epsilon = 10^-3$ (notice that the only scale in the system is given by ϵ). This is a problem even if the S_{++} is not initially present; numerically, it will be unavoidably exited and drive the solution into an exponential instability.

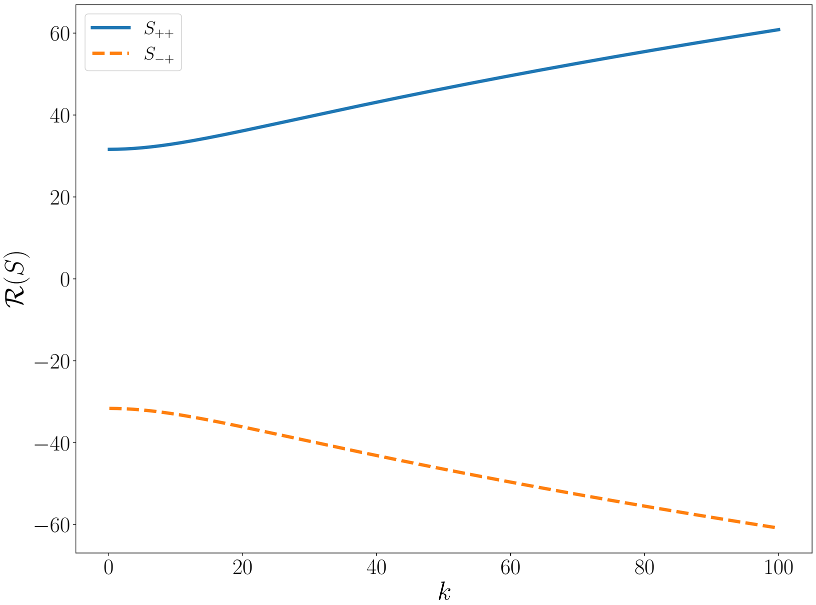

Figure A.1: Real solutions S_{++} and S_{-+} for the dispersion relation of the original system for a value of $\epsilon = 10^{-3}$. Of these S_{++} shows to be unstable.

Fixed system

Lets now find the dispersion relation for system (A.2),(A.4) using the anzats,

$$\phi(t, x) = e^{st}e^{ikx}, \tag{A.7}$$

$$\Pi(t, x) = B(s, k)e^{st}e^{ikx}. \tag{A.8}$$

By first finding B to be,

$$B(s, k) = -\frac{k^2}{k^2\sigma + s^2\sigma + \tau s + 1}, \tag{A.9}$$

one then obtains the equation:

$$s^4\sigma + s^3\tau - (-1 + (-2\sigma - \epsilon)k^2)s^2 + k^2 s\tau + k^4\sigma + k^2 = 0 \tag{A.10}$$

This equation also has four solutions ($S_i, i = 1..4$), although not as nice to show in a closed form as the original system. One can show, nevertheless, that solutions for this

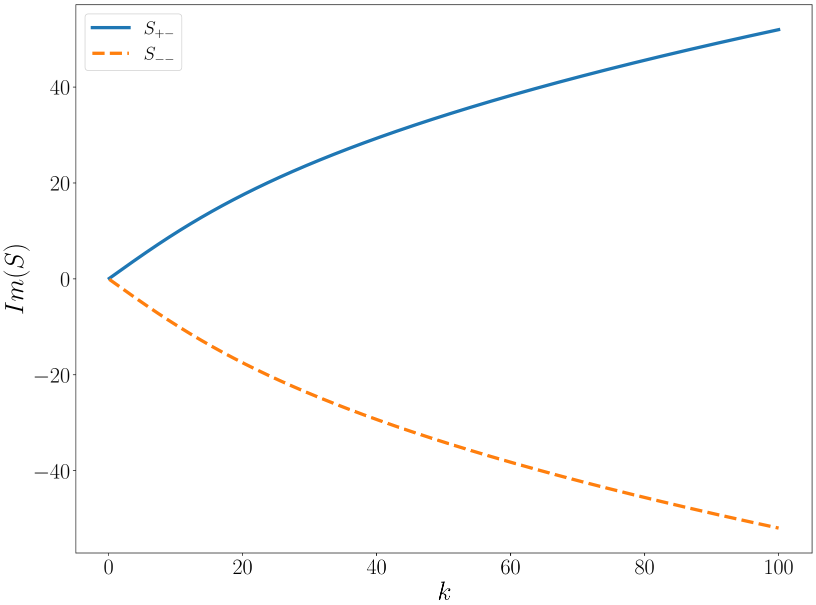

Figure A.2: Imaginary solutions S_{+-} and S_{--} for the dispersion relation of the original system for a value of $\epsilon = 10^{-3}$.

system have non-positive real parts $S_i(k)$ for all k. Figure A.3 shows the real part of these solutions for a fixed value of $\epsilon = 10^{-3}$ and different value pairs for σ and τ. When it comes to choosing good values for σ and τ, a good guiding principle is to choose them such that the fixed system reproduces the (stable) solutions from the original system in the long wavelength regime. In this scenario, the frequency that sets the upper limit at which we consider the expansion on ϵ to be valid is given by $k_{cutoff} = \epsilon^{1/2}$. So we focus on the solution for $k << k_{cutoff}$. In figure A.4 we show the relative difference between the imaginary part of S_{+-} and the imaginary part of S_1 (which is identical to the pair S_{--} , S_2.). For all the pairs plotted in A.4, this relative error is very small for small k and remains around the percent level for $k \approx k_{cutoff}$. From all these pairs of values, the pair $\sigma = \epsilon$ and $\tau = \sqrt{\epsilon}$ hold the smallest relative error with respect to the original solution essentially for all $k < k_{cutoff}$. The solution has a greater relative error for values either above or below this threshold. The real part of the original solutions S_{+-} and S_{--} is zero. In Figure A.5, we can see that the real part of the solution S_1 (equivalently for S_2) starts decreasing as k increases. Even though these solutions do not have an exactly vanishing real part, they remain small for the frequencies of interest and damp higher frequencies faster. With this in mind, a good guiding principle for choosing these parameters might be to choose them

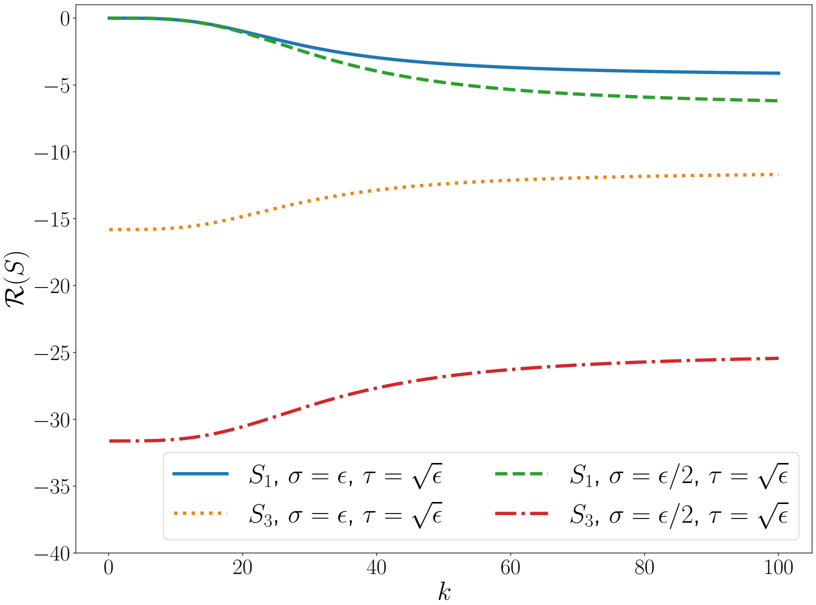

Figure A.3: Real part of the dispersion relation for the fixed system for $\epsilon = 10^{-3}$ and different value pairs for σ and τ. The real part for S_2 is the same as the one for S_1 (same with S_4 and S_3) so we omit showing the first one. All of these are negative for all values of k.

such that the real part of S_1 (and S_2) are as close to zero as possible. These solutions are closer to zero as σ increases and as τ decreases.

A.0.2 Numerical implementation and results

Having explored analytically the fixed system, we can now expect numerical simulations of it to be well-behaved. We want to study how well our new ad-hoc manages to damp departures of Π from its target value ϕ_{xx} as we vary the value of ϵ, σ, and τ. To study this, we performed a parameter exploration on a 1D simulation of an initial scalar Gaussian profile advecting to the left in a domain with periodic boundary conditions. The periodic domain is of size $L = 200$, discretized in a uniform grid. We use sixth-order accurate finite difference derivative operators. For the time steps, we implement a fourth-order Runge-Kutta with $\Delta t/\Delta x = 1/4$, and Kreiss-Oliger dissipation. The initial data consists of Gaussian profile given by $\phi(0, x) = 10^{-3} e^{-\frac{1}{2}(x-100)^2/\alpha^2}$, and its time derivative $\phi_{,t}(0, x) = \phi_{,x}(0, x)$. For consistency, the initial data we impose on the new dynamical variable Π is

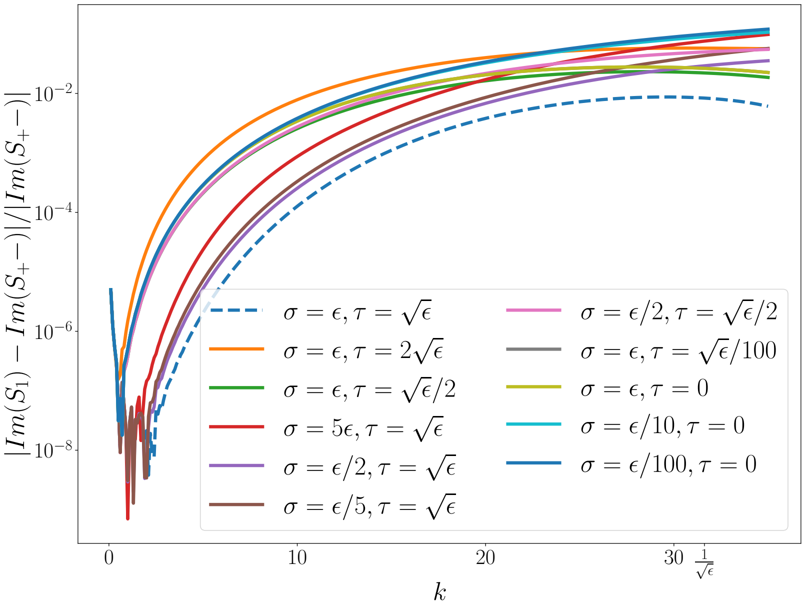

Figure A.4: Relative difference between the imaginary part of S_{+-} and the imaginary part of S_1, for a fixed value of ϵ and different values of σ and τ. Notice The smallest error is for the solution obtained with $\sigma = \epsilon$ and $\tau = \sqrt{\epsilon}$.

given by $\Pi(0, x) = \phi_{,xx}(0, x)$ and $\Pi_{,t}(0, x) = \phi_{,xxx}(0, x)$.

To study the stability and the capability of our ad-hoc equation to drive Π into ϕ_{xx} we ran this simulation for fixed values of $\epsilon = 10^{-3}$ and $\epsilon = 10^{-2}$ with $\alpha = 1$ for an array of values $\{\sigma, \tau\}$. In Figure A.6 we show the scalar field profile at $t = 0$ and at $t = 400$ (enough time for the pulse to travel twice throughout the spatial domain) for different values of ϵ and the fixing parameters. As the system evolves, the initial advecting pulse develops as an oscillatory tail as the main effect from the terms modifying the wave equation and does not develop high frequencies rendering a stable evolution. As expected, the effect of the correction is greater for the larger values of ϵ. The frequency of the oscillatory tail decreases as ϵ grows.

The system is evolved long enough such that the main "peak" passes through the center of the grid twice. To quantify how well the variable Π tracks ϕ_{xx}, we compute the quantity, which we will refer to from now on as "Tracking" and denote by $\mathcal{T}$. The "Tracking" between these two variables is defined as,

$$\mathcal{T} = \frac{||\Pi - \phi_{xx}||_2}{||\phi_{xx}||_2}, \tag{A.11}$$

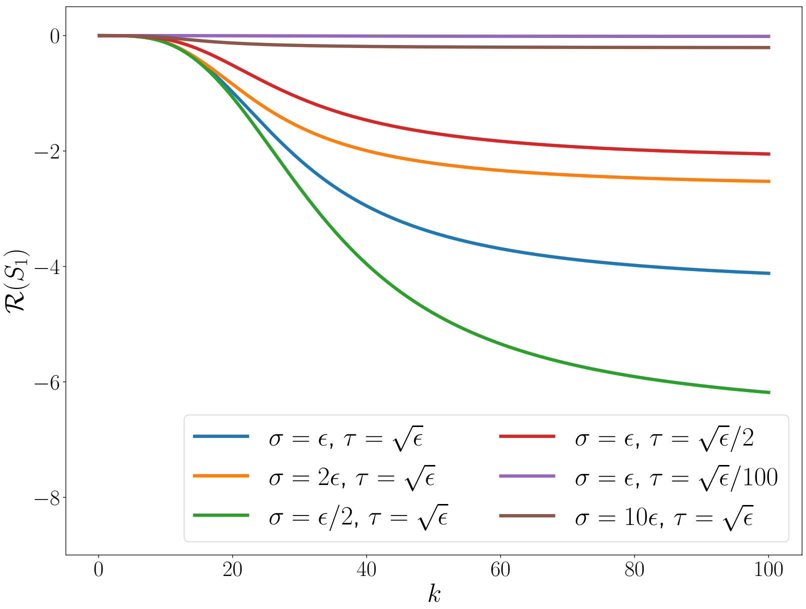

Figure A.5: Real part of S_1 for a fixed value of ϵ and different values of σ and τ as a function of k. The solution gets closer to zero as τ decreases or σ increases.

were $|| \quad ||_2$ denotes the $l2$ norm over the whole domain. The results from these simulations can be seen in Figure A.7 where we plot the tracking $\mathcal{T}$ computed at the final time of the simulation as a function of the fixing parameters σ and τ. The blue points are simulations that remain stable throughout the whole evolution. This plot shows that $\mathcal{T}$ decreases up to a relative error of $\approx 10^{-5}$ for the best pair of $\{\sigma, \tau\}$ values. Figure A.7 also shows how the tracking decreases linearly until saturation as we decrease the value of one of the fixing parameters while keeping the other one fixed. The red dots in this figure correspond to points where the simulation was unstable and crashed. These unstable evolutions appear mostly for small values of σ. They can be associated with the equations becoming "stiff", and we have checked that one can obtain stable evolutions for smaller values of σ by using smaller time steps. It is also important to compare how different solutions with different $\{\sigma, \tau\}$ pairs are from each other. Achieving good tracking would be useless if this implies a non-convergent solution as we vary $\{\sigma, \tau\}$ to lower the value of $\mathcal{T}$. We corroborate that as the value of $\mathcal{T}$ decreases, the difference between the physical variable ϕ between simulations with different fixing parameters also decreases. For example, the relative error between the two curves in Figure A.6 obtained for $\epsilon = 10^{-3}$ have a relative error, computed as $||\phi_1 - \phi_2||_2/||\phi_1||_2$, of $\approx 10^{-6}$.

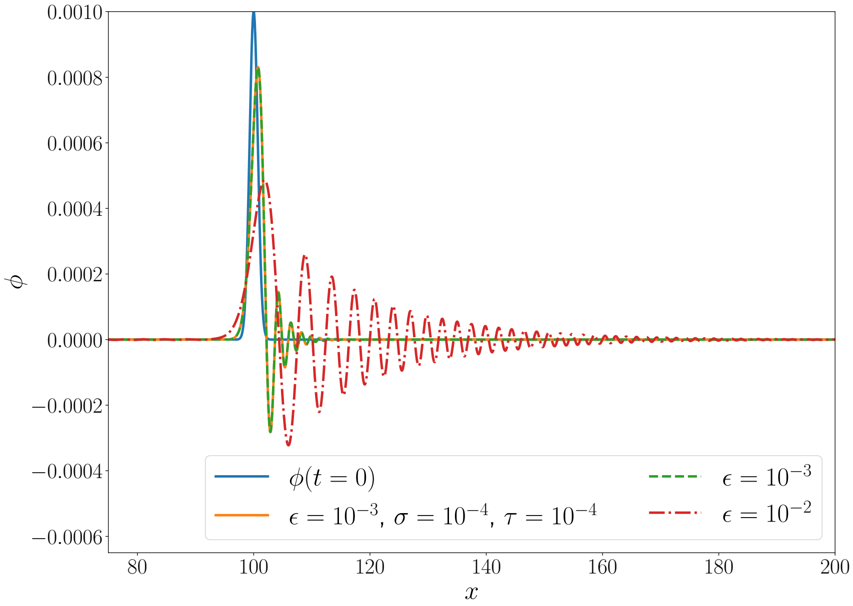

Figure A.6: Scalar field ϕ profile at $t = 0$ and at $t = 400$ for different values of ϵ and the fixing parameters. The dashed green and red dashed-dotted curves were obtained using $\sigma = 10^{-3}$ and $\tau = 10^{-3}$. Notice there is no discernible difference between the two curves for $\epsilon = 10^{-3}$.

The effects from the correcting terms in the wave equation will become more important as the value of ϵ increases. To study how this would affect the fixing procedure, stability, and tracking, we perform the same parameter exploration for $\epsilon = 10^{-2}$. The results are displayed in Figure A.8. In contrast to $\epsilon = 10^{-3}$ in this case we are only able (for the same $\Delta t/\Delta x$=0.25) to have stable simulations for $\sigma \approx 10^{-3}$ as opposed to $\approx 10^{-4}$ and best achievable tracking is $\approx$$10^{-4}$ as opposed to $\approx 10^{-5}$.

This simple example shows how the *Fixing* method allowed us to reformulate the original pathological system into a new one free of pathologies. We were able to see analytically that the solution in the long-wavelength regime reproduces quite well the solution of the original system in such regime and that no unstable modes are present in the new system. Furthermore, we corroborated the expectations from the analytical study through numerical simulations. In such simulations, we demonstrated how we achieved stable numerical evolution and studied the dependence of the solution on the fixing parameters $\{\sigma, \tau\}$. We showed, through computation of the tracking measure $\mathcal{T}$ the ability of our system to drive the new variable Π to its target value ϕ_{xx}, and that the obtained solution does not depend

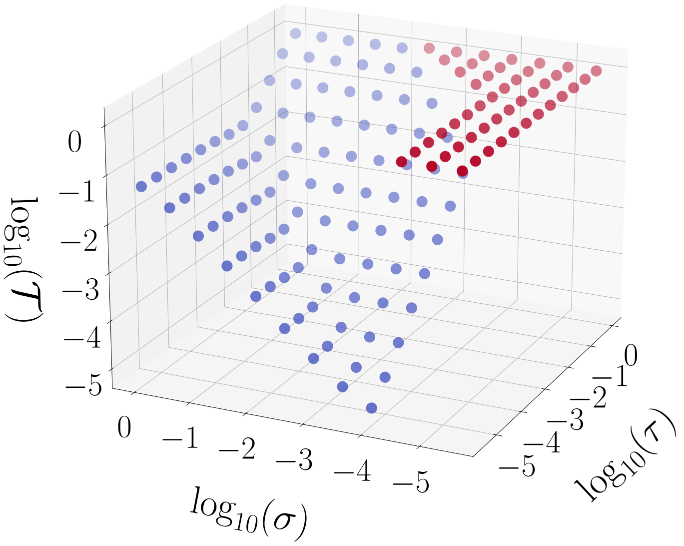

Figure A.7: Tracking $\mathcal{T}$ quantity for simulations with $\epsilon = 10^{-3}$ and $\alpha = 1$ for a range of values σ and τ. The red dots correspond to simulations that crashed due to instabilities. The blue dots show how the tracking improves linearly with τ and σ decrease until saturation is reached for a fixed value of the other fixing parameter.

strongly on $\{\sigma, \tau\}$.

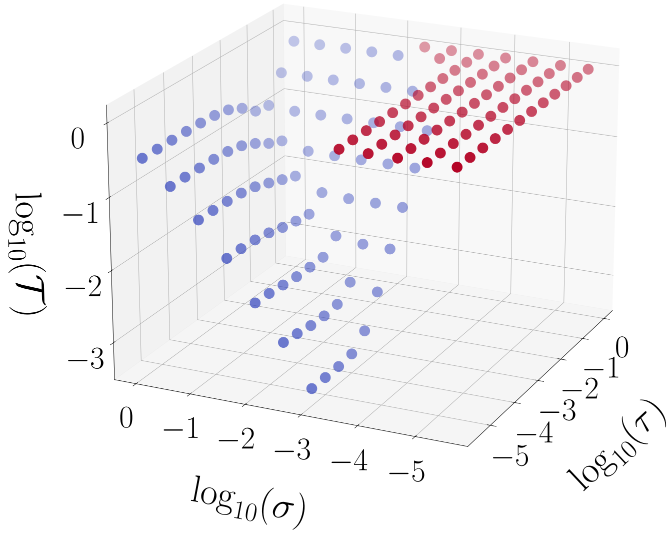

Figure A.8: Tracking $\mathcal{T}$ quantity for simulations with $\epsilon = 10^{-2}$ and $\alpha = 1$ for a range of values σ and τ. The red dots correspond to simulations that crashed due to instabilities. The blue dots show how the tracking improves linearly with τ and σ decrease until saturation is reached for a fixed value of the other fixing parameter.

Appendix B

Removing Ostrogradsky's ghost, an example.

B.1 One-dimensional point particle example

This appendix will review the order reduction example presented in [173]. Consider a one-dimensional point particle with the following Lagrangian:

$$L = \frac{1}{2}\dot{x} - \epsilon\frac{1}{2}\ddot{x} - \frac{1}{2}m^2x^2 + \mathcal{O}(\epsilon^2), \tag{B.1}$$

where ϵ is an expansion parameter which we can related to $\left(\frac{1}{\Lambda^6} = \epsilon\right)$ in this thesis. The equations of motion for this Lagrangian contain fourth-time derivatives,

$$\ddot{x} + m^2x - \epsilon x^{(4)} = \mathcal{O}(\epsilon^2). \tag{B.2}$$

Its exact solutions are given by,

$$x(t) = A_+ \exp^{k_+t} + B_+ \exp^{-k_+t} + A_- \exp^{k_-t} + B_- \exp^{-k_-t}, \tag{B.3}$$

where $A_\pm$ and $B_\pm$ are determined by four initial conditions, and k_+ and k_- are given by,

$$k_\pm^2 = \frac{1}{2\epsilon}(1 \mp \sqrt{1 + 4\epsilon m^2}). \tag{B.4}$$

Expanding to leading order in ϵ we can see,

$$k_+ \approx im + \mathcal{O}(\epsilon), \quad k_- \approx \frac{1}{\sqrt{\epsilon}} + \mathcal{O}(\epsilon^0). \tag{B.5}$$

Thus it is clear that the terms with exponents k_+ are oscillatory, while the other two represent exponentially growing or decaying solutions that are not consistent with the perturbative expansion and hence considered nonphysical.

The process to avoid having these unhealthy solutions start by first noticing that equation (B.2) contains in the right-hand side the $\mathcal{O}(\epsilon^2)$ symbol, then we can benefit from the fact that the equation is only valid to that order. Taking two time derivatives of (B.2), isolating the fourth time derivative, and considering the equation valid up to order $\mathcal{O}(\epsilon)$, we get,

$$x^{(4)} = -m^2\ddot{x} + \mathcal{O}(\epsilon), \tag{B.6}$$

which can be substituted in (B.2) to get,

$$\ddot{x} + \tilde{m}^2 x = \mathcal{O}(\epsilon^2) \quad , \quad \tilde{m}^2 \equiv (1 - \epsilon m^2)m^2. \tag{B.7}$$

Equation (B.7) has a straightforward solution,

$$x(t) = A\cos(\tilde{m}t) + B\sin(\tilde{m}t), \tag{B.8}$$

which upon expanding to $\mathcal{O}(\epsilon^2)$ takes the form,

$$x(t) = A\cos(mt) + B\sin(mt) + \frac{1}{2}\epsilon m^3 t(A\cos(mt) - B\sin(mt)) + \mathcal{O}(\epsilon^2). \tag{B.9}$$

It can be then checked that (B.9) is the same solution one would obtain by solving (B.2) by a perturbative expansion method using $x = x_0 + \epsilon x_1 + \mathcal{O}(\epsilon^2)$. The solution obtained then no longer possesses exponentially growing/decaying solutions.

Appendix C

Appendix for Chapter 3.

C.1 Convergence

To check convergence, we adopt the base uniform grid spacing to be $dx = 0.037M$ and compute the convergence factor as,

$$Q \equiv \ln\left(\frac{||u_{dx} - u_{dx/2}||_2}{||u_{dx/2} - u_{dx/4}||_2}\right) / \ln(2), \tag{C.1}$$

were u_{dx}, $u_{dx/2}$ and $u_{dx/4}$ stands for any of the dynamical fields evolved with resolutions dx, $dx/2$ and $dx/4$ respectively. In Figures C.1 and C.2 we present the convergence factor Q for simulations with a fixed coupling of $\epsilon = 1 \times 10^{-2}$, $\tau = 5 \times 10^{-3}$, an initial amplitude of the scalar field given by $A = 1 \times 10^{-3}$, centered at $r_c = 20M$ and of width $\sigma = 1$, and the initial total mass of the spacetime is $M = 1$. Figure C.1 shows the measured rate for the "standard" fields (i.e., those that would only be present in GR). The majority of fields display a rate of around 4th to 6th order, which is consistent with the 4th-order accuracy of our time integrator or the 6th-order accuracy –at interior points—of our finite difference derivative operators. The field K_T rate is $\simeq 3$, indicating its behavior is dominated by the 3rd order accuracy at boundary points of our scheme. Figure C.2 displays the rate for the new variables $\Pi_{\mu\nu}$ introduced to evolve the modified theory, which converge at order $Q \approx 3$.

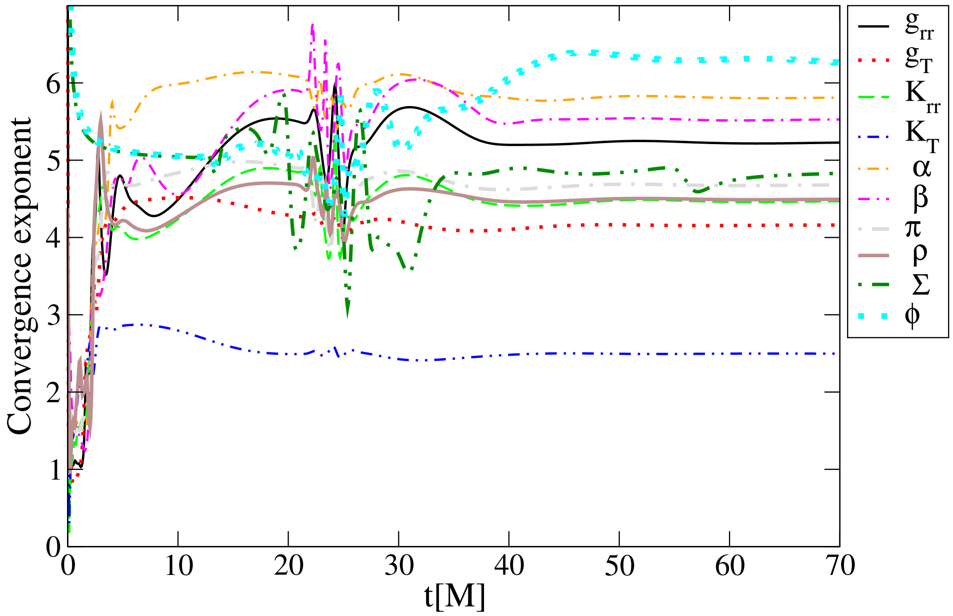

Figure C.1: Convergence factor Q as a function of time. In most cases, the convergence settles between 4th and 6th order. For K_T $Q \approx 3$.

C.2 Constraints

We also monitor the behavior of constraints (4.6a), (4.6b),(4.6c) and (4.6d) during evolution. In particular, Figure C.3 displays the norms of each one as a function of time for our base resolution of $dx = 0.019M$, coupling $\epsilon = 1 \times 10^{-2}$, $\tau = 5 \times 10^{-3}$ and initial scalar profile with center and width are $A = 1 \times 10^{-3}$, $r_c = 20M$ and $\sigma = 1$ respectively. To assess the magnitude of constraint violations, we normalized the norms of every constraint by the sum of the norms of each term that define it. Such violations remain below $\approx 1\%$ during evolution.

It is also important to check how effective equations (4.14) are to enforce variables $\Pi_{\mu\nu}$ approximate $\widetilde{M}_{\mu\nu}$. To this end, we monitor the quantities given by

$$\mathcal{P}_{\mu\nu} \equiv \frac{||\Pi_{\mu\nu} - \widetilde{M}_{\mu\nu}||_2}{||\widetilde{M}_{\mu\nu}||_2}. \tag{C.2}$$

Figure C.4 displays the behavior of $\mathcal{P}_{tt}$ for $\epsilon = \{0.01, 0.05\}$ (two strong coupling values) and choosing $\tau = \{0.002, 0.005\}$ (two different values of driving timescales). The

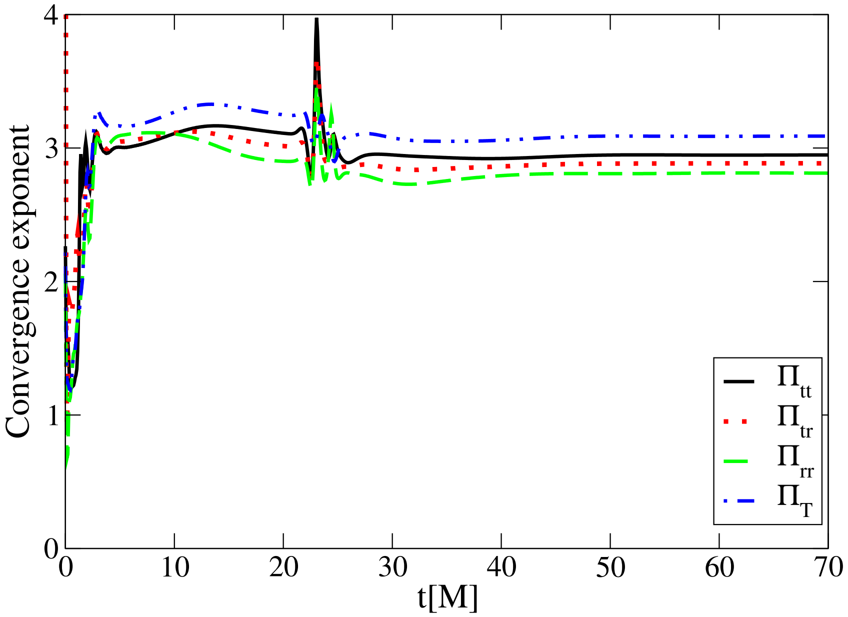

Figure C.2: Convergence factor Q as a function of time for the $\Pi_{\mu\nu}$ variables. The behavior is consistent with 3rd-order convergence.

difference between Π_{tt} and $\widetilde{M}_{tt}$ stays small throughout, but it is most pronounced at two moments during the evolution. One at the beginning of the simulation until the initial solution rapidly transitions (primarily due to gauge evolution) and a second rise, during the accreting stage. Both are the regimes with the most marked time dependence. For the values chosen, the differences are bounded by 2% (0.5%) during the initial (accretion) stage, but are diminished by decreasing the value of the timescale τ.

It is instructive also to monitor these quantities restricted to the *exterior* of the apparent horizon as M_{tt} can be quite large inside and skew the interpretation of difference. Figure C.5 shows that with this restriction, the initial transient transient is significantly reduced but it is larger during the accretion stage, raising to $\approx 7\%$. Nevertheless, this can be reduced by adopting a different value of τ. For instance, it is reduced by about half going from $\tau = 0.05$ to $\tau = 0.02$. Finally, we note that differences in the other components of $\mathcal{P}_{\mu\nu}$ behave similarly to the one displayed by $\mathcal{P}_{tt}$.

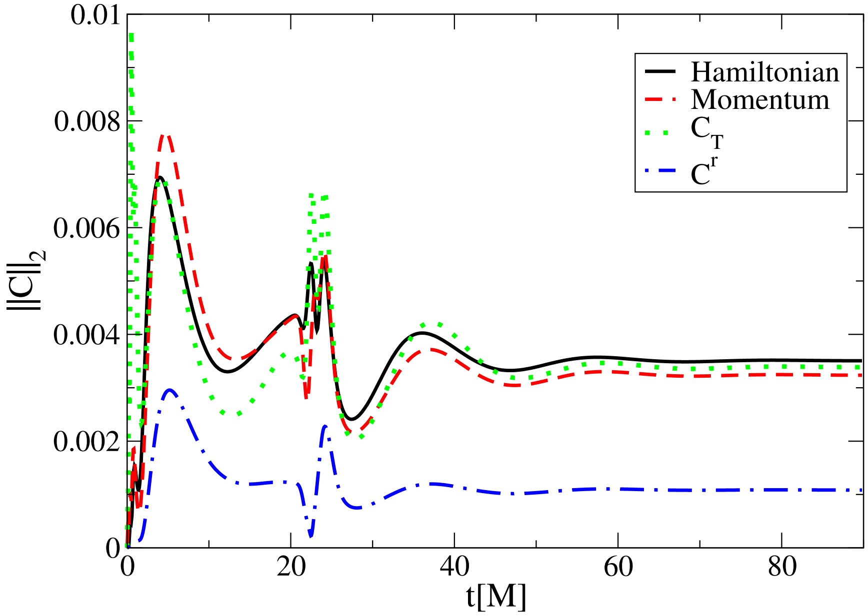

Figure C.3: Norm of the constraints as a function of time for $dx = 0.019M$, $\epsilon = 1 \times 10^{-2}$, $A = 1 \times 10^{-3}$, $r_c = 20M$ and $\sigma = 1$.

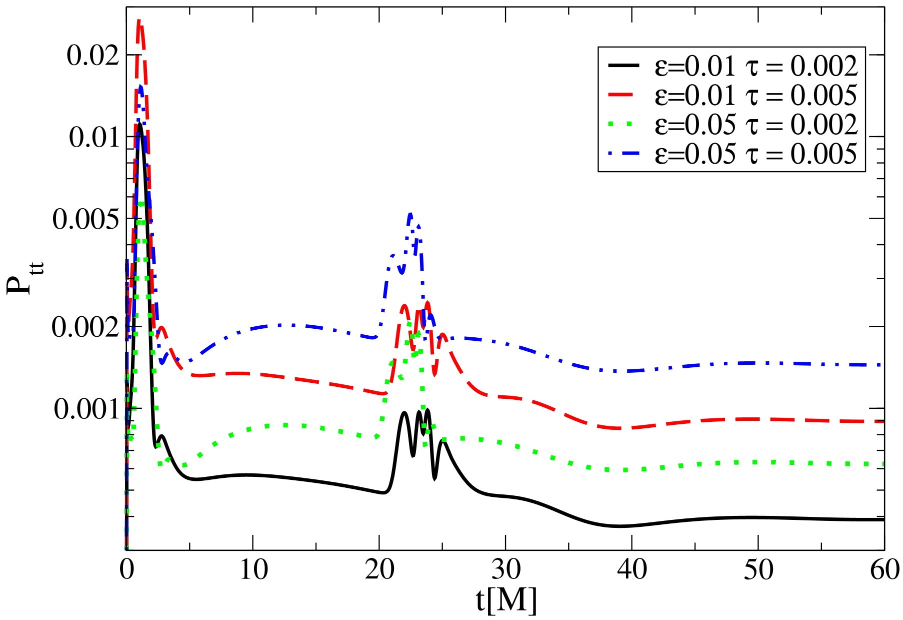

Figure C.4: $\mathcal{P}_{tt}$ as a function of time for different values of the coupling ϵ and the coupling τ.

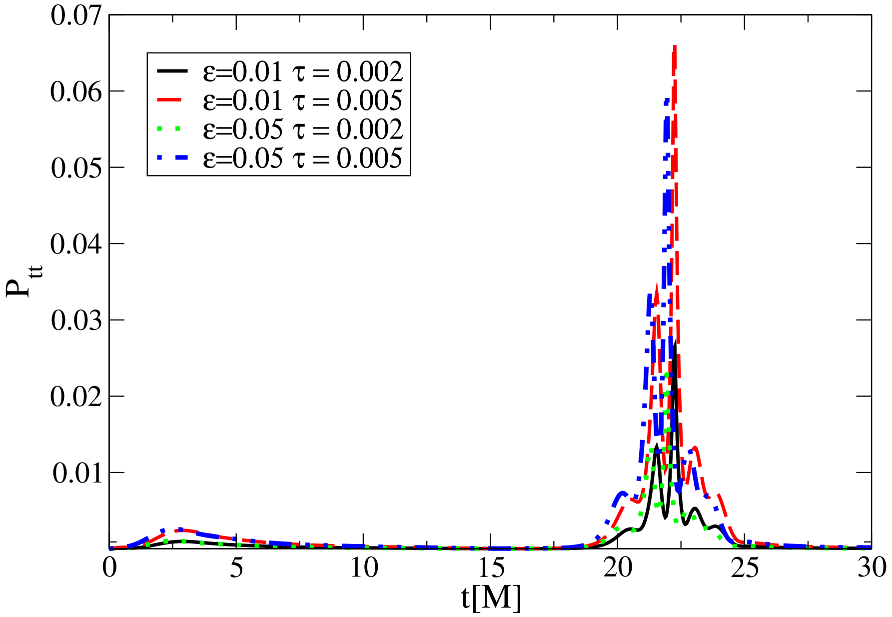

Figure C.5: $\mathcal{P}_{tt}$ as a function of time for different values of the coupling ϵ and the coupling τ. The norms are calculated over points at or exterior to the apparent horizon.

Appendix D

Appendix for Chapter 4.

D.1 Excision

The numerical treatment of solutions containing BHs requires dealing with the singular behavior of its interior. In GR, excising from the computational domains trapped region(s) (which can be shown to lie within BHs and thus are causally disconnected from their exterior) or mapping the interior of BHs to other causally disconnected asymptotic regions are practical and successful techniques to address this issue. With beyond GR theories, extensions of these ideas can be adopted. Here, we follow a strategy implemented in [86], where terms beyond GR are "turned off" inside the apparent horizon (AH), thus allowing one to follow the standard approach in GR and use a puncture gauge to handle (coordinate) singularities inside BHs. By turning off beyond GR terms well inside the AH, we are modifying the theory in a region of spacetime that is causally disconnected from any external observer and where the theory should no longer be a valid EFT anyway.

Since the higher-derivative terms enter the equations of motion as an effective stress-energy tensor T_{ab}, a measure of the weak field condition is provided by the "size" of the components of T_{ab}. In the 3+1 decomposition, we have

$$\rho = n^a n^b T_{ab}\,, \quad S_i = -n^a \gamma_i{}^b T_{ab}\,, \quad S_{ij} = \gamma_i{}^a \gamma_j{}^b T_{ab}\,. \tag{D.1}$$

Then, a point-wise measure of the weak field condition is captured by the quantity

$$W = \sqrt{\rho^2 + S_i S_j \delta^{ij} + S_{ij} S_{kl} \delta^{ik} \delta^{jl}} \tag{D.2}$$

This quantity need not be covariant nor anything special, it is just a measure where we can input a threshold; it is preferred to ρ, which goes to zero at the puncture (even though it is large in the surrounding region).[1]

Given an energy-momentum tensor, we damp the "effective source" inside the AH, and when the weak field condition W is too large by a factor $e \cdot T_{ab}$ where e is a smooth transition function:

$$e(\chi, W) = 1 - \sigma(\chi; \bar{\chi}, \omega_\chi)\sigma(W; \bar{W}, -\omega_W) \tag{D.3}$$

where, $\sigma(x; \bar{x}, \omega_x)$ is defined as,

$$\sigma(x; \bar{x}, \omega_x) = \frac{1}{1 + 10^{\frac{1}{\omega_x}\left(\frac{x}{\bar{x}} - 1\right)}}, \tag{D.4}$$

where χ is the conformal factor of the induced metric, $\bar{\chi}$ and $\bar{W}$ are thresholds for the excision cutoff region and ω_χ and ω_W are smoothness widths. With this choice of $e(\chi, W)$, the source approaches 0 exponentially whenever $\chi < \bar{\chi}$ and $W > \bar{W}$, and is 1 otherwise. The parameters ω_χ and ω_W determine the width of the transition region; we typically choose them to be $\omega_\chi = \omega_W = 0.1$. Since the contours of χ in our working gauge track the AH very well, we choose a threshold $\bar{\chi}$ that ensures that the excision region is well inside the AH. In practice, we ended up taking $\bar{W} = 0$ so that $\sigma(W; \bar{W}, -\omega_W)$ is always effectively 1, and hence the excision region is solely determined by the value of χ. In practice, for non-spinning BH binaries, the choice $\bar{\chi} = 0.09$ ensures that the excision region is well within the AH [158, 92].

D.2 Convergence

We test convergence by comparing the evolution presented, which used a numerical grid coarsest spacing of $\Delta = 4M$ and eight further levels of refinement, with two higher resolutions, with spacing $\Delta = \frac{32}{11}M$ (medium) and $\Delta = frac83M$ (high). The particular setting for these simulations has $\epsilon = 10^{-5}M_S^6$, $\sigma = 0.1$ and $\tau = 0.005$. Figure D.1 shows gravitational strain errors between low, medium, and high resolutions, together with the estimates for second and fourth-order convergence based on the convergence proportionality factor

$$Q_n = \frac{\Delta^n_{\text{Low}} - \Delta^n_{\text{Med}}}{\Delta^n_{\text{Med}} - \Delta^n_{\text{High}}}\,. \tag{D.5}$$

This figure indicates approximately fourth-order convergence for the amplitude and the phase of h^+_{22}.

---

[1] This is because we turn off the non-GR terms inside BHs, as we explain in the following paragraph.

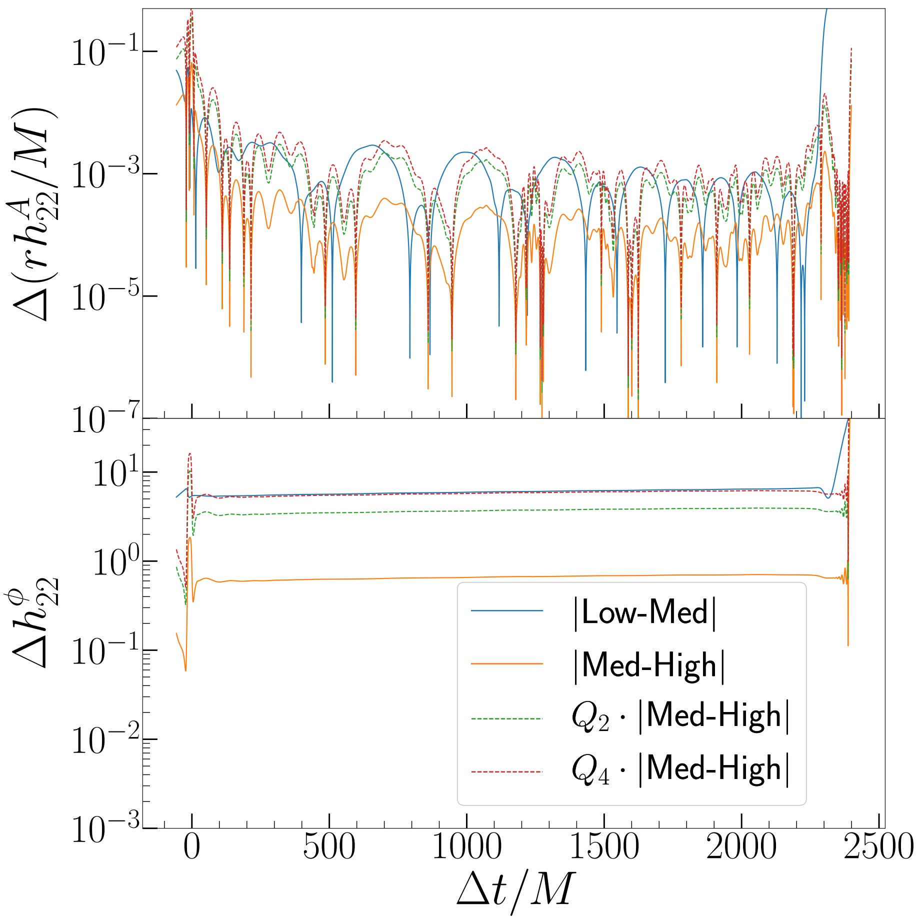

Figure D.1: Errors for the amplitude (top) and phase (bottom) of the + polarisation h^{+}_{22}, extrapolated to null infinity, as a function of retarded time. The dotted lines show estimates for the error between low and medium resolutions assuming second and fourth-order convergence. The waves were aligned by their peaks. These figures are consistent with approximately fourth-order convergence.

Appendix E

Appendix for Chapter 5.

E.1 Convergence

To check the convergence of the solutions, the base uniform grid spacing $dx = 0.04$ is adopted, and the convergence factor is computed as,

$$\mathcal{Q} \equiv \ln\left(\frac{||u_{dx} - u_{dx/2}||_2}{||u_{dx/2} - u_{dx/4}||_2}\right), \tag{E.1}$$

here, u_{dx}, $u_{dx/2}$ and $u_{dx/4}$ stand for any field evolved with resolutions dx, $dx/2$ and $dx/4$ respectively. In Figure E.1 we plot the convergence factor $\mathcal{Q}$ for the K_{rr} variable in the BH collapse scenario : $A = 0.0023$, $\sigma = 1$, $r_c = 10$, $z = 0.5$, $\kappa = 2$. For practical reasons, we only plot the convergence until an apparent horizon has been detected. The convergence factor behaves similarly to the other dynamical variables. The black curve in Figure E.1 shows the convergence factor for the GR case and shows how the convergence is ≈ 4 at the beginning of the simulation and close to the collapse $\mathcal{Q}$ quickly climbs to values between 5 and 6. This is consistent with the 4th-order accuracy of the Runge-Kutta time integrator and the 6th-order accuracy of finite difference derivative operators. This seems to be similar for essentially all the $\epsilon_2 \neq 0$ simulations. The result changes drastically for the $\epsilon_1 \neq 0$ simulations, where we can see the convergence factor does drop to lower values as the system is close to collapse. Some of these simulations retain acceptable convergence factors, for example, the cases with $\epsilon_1 = 10^{-3}$, $\epsilon_1 = 5 \times 10^{-3}$ and $\epsilon_1 = -10^{-3}$ drop to convergence factors of values $\mathcal{Q} \approx 4$, $\mathcal{Q} \approx 3$ and $\mathcal{Q} \approx 2$ respectively. However, when the magnitude of ϵ_1 increases, we can see how all convergence is quickly lost. This coincides

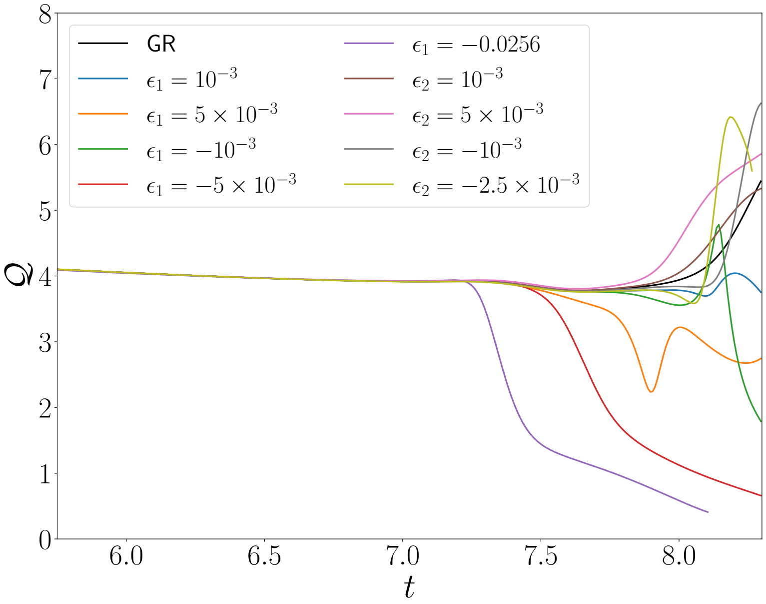

Figure E.1: Convergence factor $\mathcal{Q}$ for the K_{rr} variable as a function of time close the time of collapse for different values of ϵ_1 and ϵ_2.

mainly with the regime we have identified of simulations leaving the regime of applicability of the EFT.

E.2 Constraints

Monitoring that the constraints (4.6a), (4.6b), (4.6c), and (4.6d) remain under control is important to attest to the quality of the performed simulations. In Figure E.2 we plot the valuer of the $l2$-norm of Hamiltonian constraint (4.6b) for different values ϵ_1 and ϵ_2. Here we have normalized by the $l2$-norm of the most relevant terms that define it to get a relative notion of the violation of constraints. The other constraints display similar behavior, so we omit to show them. The black curve shows our reference GR simulation using the same parameters used in the convergence test for the $dx = 0.02$ grid spacing. The GR case Hamiltonian violation remains extremely small during the evolution, rising as expected close to the collapse time but never rising above a relative error of 10^{-8}. For convenience, we only plot the constraint violations until an apparent horizon is formed; after this apparent horizon forms and excision is applied, the constraint violations naturally

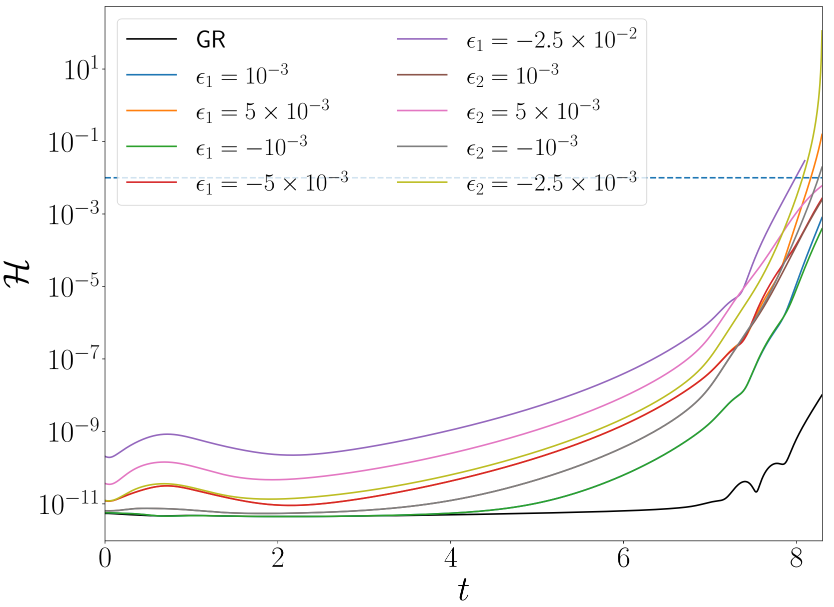

Figure E.2: $l2$-norm of the Hamiltonian constraint as a function of time for simulations with different values of ϵ_1 and ϵ_2. The horizontal dashed line highlights the 1% error .

become smaller.

The situation changes once either of the couplings is non-vanishing; the constraint violations remain below the 10^{-8} relative error for most of the simulation but then quickly rise as the scalar field profile approaches the center of coordinates. For most cases, the constraint violation remains below the 1% level throughout the simulation. However, there are cases in which violations are within a worrying 1% and 10% like for $\epsilon_2 = -10^{-3}$ and $\epsilon_1 = -2.5 \times 10^{-2}$, and cases were the violations $> 10\%$ and greater than 1000% error, for $\epsilon_1 = 5 \times 10^3$ and $\epsilon_2 = -2.5 \times 10^3$. These larger constraint violations are no surprise; manipulations in the constraint equations were performed that assume that the modifying terms remain corrective (i.e., within the applicable regime of the EFT), and these corrections become greater as the pulse collapses. The cases where constraint violations are large enough to be unable to trust simulations anymore also belong in the parameter regime that has shown either through loose or convergence or by leaving the EFT regime that these solutions can not be trusted.